Plasmon-enhanced electrocatalysis

over Cu-based bimetallic tandem catalysts

Li Zhu

München 2025

Plasmon-enhanced electrocatalysis

over Cu-based bimetallic tandem catalysts

Li Zhu

Dissertation

an der Fakultät für Physik

der Ludwig-Maximilians-Universität

München

vorgelegt von

Li Zhu

aus China

München, den 28/10/2025

Erstgutachter/in: Prof. Dr. Emiliano Cortés
Zweitgutachter/in: Prof. Dr. Johanna Eichhorn
Tag der mündlichen Prüfung: 11/12/2025

Contents

List of Figures

Publications and Conferences

Publications Included in This Dissertation

Zhu, L., Liu, K., Li, H. J., Mei, Z., Kang, Y., Chen, Q., Wang, X., Zhang, H., Zi, X., Wang, Q., Fu, J., Pensa, E., Stefancu, A., Liu, M., Cortés, E. Plasmon-Enhanced C_2H_4 Generation in the CO_2 Electroreduction Reaction on a CuPd Tandem Catalyst. **Journal of the American Chemical Society**, 2025, 147(36), 33003-33017.

Wang, Y.-H.,† **Zhu, L.**,† Mariani, E., Pensa, E., Henrotte, O., Xia, Y., Müller-Caspary, K., Zhang, T.-Y., Gao, M.-R., Cortés, E. Plasmonic Enhancement in an Earth-Abundant CuNi Catalyst for Alkaline Hydrogen Evolution Reaction. **To be submitted, 2025**

Liu, M., Wang, Q., Luo, T., Herran, M., Cao, X., Wao, W., **Zhu, L.**, Li, H., Stefancu, A., Lu, Y.-R., Chan, T.-S., Pensa, E., Ma, C., Zhang, S., Xiao, R., and Cortés, E. Potential Alignment in Tandem Catalysts Enhances CO_2-to-C_2H_4 Conversion Efficiencies. **Journal of the American Chemical Society**, 2024, 146(1), 468-475.

Zi, X., Zhou, Y., **Zhu, L.**, Chen, Q., Tan, Y., Wang, X., Sayed, M., Pensa, E., Geioushy, R. A., Liu, K., Fu, J., Cortés, E., Liu, M. Breaking K^+ Concentration Limit on Cu Nanoneedles for Acidic Electrocatalytic CO_2 Reduction to Multi-Carbon Products. **Angewandte Chemie International Edition,** 2023, 62(42), e202309351.

Additional Publications

Kang, Y., João, S.M., Lin, R., Liu, K., **Zhu, L.**, Fu, J., Cheong, W.C., Lee, S., Frank, K., Nickel, B., Liu, M., Lischner, J., Cortés, E. Effect of Crystal Facets in Plasmonic Catalysis. **Nature Communications**, 2024, 15(1), 3923.

Liu, K., Fu, J., Luo, T., Ni, G., Li, H., Lin, Z., **Zhu, L.**, Wang, Y., Zhang, L., Sun, Y., Cortés, E., Liu, M. Potential-Dependent Active Moiety of Fe-N-C Catalysts for the Oxygen Reduction Reaction. **The Journal of Physical Chemistry Letters**, 2023, 14(15), 3749-3756.

Nan, L., Giráldez-Martínez, J., Stefancu, A., **Zhu, L.**, Liu, M., Govorov, A. O., Besteiro, L. V., and Cortés, E. Investigating Plasmonic Catalysis Kinetics on Hot-Spot Engineered Nanoantennae. ***Nano Letters***, 2023, 23, 2883-2889.

Stefancu, A., Lin, N., **Zhu, L.**, Chiș, V., Bald, I., Liu, M., Leopold, N., Maier, S. A., Cortés, E. Controlling Plasmonic Chemistry Pathways through Specific Ion Effects. **Advanced Optical Materials**, 2022, 10, 2200397.

Conference

29 Sep-1 Oct 2025, Bayreuth - 14th SolTech Conference

Poster: "Plasmon-enhanced Electrocatalysis for Highly Effient Energy Coversion"

23-27 Oct 2023, Paris - Paris-Saclay Plasmonics School

Poster: "Plasmonic interfaces for chemical energy production"

6-9 Mar 2023, Bayrischzell - The e-conversion Winter Retreat

4-7 Oct 2022, Venice - e-conversion Conference 2022

Poster: "Plasmonic interface for chemical energy production"

30 Aug-2 Sep 2022, Munich - The International Nanoscience Students Conference

Short Talk & Poster: "CuPd catalyst improve the selectivity of CO_2 electroreduction to C_{2+} products by a tandem reaction mechnism"

Exchange

2-11 Dec 2024, Univerity of Campinas, Brazil

Grant from DAAD-CAPES project between University of Campinas, Brazil and LMU Munich, Germany.

Project Tittle: "Boosting green hydrogen production through the plasmonic-driven electrooxidation"

25 Dec 2023-7 Feb 2024, Central South University, Changsha

Project Tittle: "Plamon-enhanced electroreduction CO_2 reaction on CuPd catalyst"

Zusammenfassung

Die elektrochemische Reduktion von Kohlendioxid (CO_2RR) und die Wasserstoffentwicklungsreaktion (HER) gelten als vielversprechende Wege zu einem CO_2-neutralen Energiekreislauf, indem sie eine durch erneuerbare Elektrizität angetriebene Kohlenstoffrecyclingstrategie und die Erzeugung von grünem Wasserstoff (H_2) ermöglichen. Die praktische Umsetzung dieser Technologien wird jedoch weiterhin durch intrinsische kinetische Barrieren und eine unzureichende Kontrolle über Grenzflächenreaktionen eingeschränkt. Die CO_2RR leidet unter einer hohen Aktivierungsbarriere von CO_2 sowie ineffizienter Protonierung und Kopplung des kritischen Zwischenprodukts *CO (adsorbiertes Kohlenmonoxid auf der Katalysatoroberfläche), während die HER in alkalischer Umgebung durch eine träge Wasserspaltungskinetik im Volmer-Schritt behindert wird.

Um diese Herausforderungen zu bewältigen, untersucht diese Dissertation plasmonenverstärkte Elektrokatalyse als eine fortschrittliche Strategie, um die elektronische Struktur und Reaktionsenergetik an der Grenzfläche durch lokalisierte Oberflächenplasmonenresonanz (LSPR) zu modulieren. Aufgrund ihrer einzigartigen katalytischen Eigenschaften und plasmonischen Reaktion im sichtbaren Bereich dient Kupfer (Cu) als vielseitige Plattform für den Aufbau von Cu-basierten bimetallischen Tandemkatalysatoren zur CO_2-Umwandlung und H_2-Erzeugung.

Zunächst werden die zugrunde liegenden Mechanismen der plasmonenverstärkten Elektrokatalyse erläutert, einschließlich elektromagnetischer Nahfeldverstärkung, Erzeugung und Transfer von heißen Ladungsträgern sowie lokaler photothermischer Erwärmung. Deren synergistische Effekte beschleunigen die Reaktionsgeschwindigkeit, stabilisieren Reaktionsintermediate und steuern die Produktselektivität. Basierend auf diesen Prinzipien wurden drei repräsentative Cu-basierte bimetallische Systeme – CuPd, CuNi und CuAg – rational entwickelt und umfassend experimentell sowie theoretisch untersucht.

Für die CO_2RR wurde ein CuPd-Tandemkatalysator mittels Keimwachstumsmethode hergestellt. Unter resonanter Beleuchtung fördert die Plasmonenanregung die *CO-Bildung an CuPd-Grenzflächenstellen, woraufhin dieses zu Cu-Zentren diffundiert und koppelt, was die Ausbeute an C_2H_4 um 27% steigert. Für die alkalische HER wurde ein CuNi-Katalysator durch pulsierende Elektroabscheidung synthetisiert, um eine starke Grenzflächenkopplung zu erzielen. Heiße Elektronen, die auf Cu erzeugt werden, werden schnell in die Ni-Aktivzentren injiziert und verbessern die Wasserspaltung, während die photothermische Erwärmung den Stofftransport unterstützt. Bemerkenswerterweise übertrifft der beleuchtete CuNi-Katalysator die Leistung von kommerziellem Pt. Im CuAg-System fungieren Ag-Nanospitzen als hochaktive Zentren für die *CO-Bildung, während Cu die Protonierung von *CO in Richtung Methan katalysiert. Das Verhältnis der Ag- zu Cu-Zentren erweist sich als entscheidender Fak-

tor für die Tandemselektivität gegenüber Kohlenwasserstoffprodukten, mit zusätzlichem Verbesserungspotenzial durch Plasmonenanregung.

Insgesamt etabliert diese Arbeit einen einheitlichen Plasmonen-Engineering-Ansatz für Cu-basierte Tandemkatalysatoren, der eine effiziente CO_2-Umwandlung und die Produktion von grünem H_2 ermöglicht. Durch die Aufklärung, wie Plasmonenanregung den Ladungstransfer und die Reaktionskinetik in komplexen bimetallischen Systemen dynamisch moduliert, liefert diese Dissertation wertvolle Designprinzipien für die nächste Generation plasmonenverstärkter Elektrokatalysatoren und unterstützt die zukünftige Integration optischer Anregung in skalierbare elektrochemische Energiesysteme.

Abstract

The carbon dioxide electroreduction reaction (CO_2RR) and hydrogen evolution reaction (HER) are recognized as promising pathways toward a carbon-neutral energy cycle by enabling renewable electricity-driven carbon recycling and green hydrogen (H_2) production. However, the practical implementation of these technologies remains limited by intrinsic kinetic barriers and insufficient control over interfacial reaction pathways. CO_2RR suffers from the high CO_2 activation barrier and unefficient protonation and coupling of key intermediates *CO (an adsorbed carbon monoxide on the catalyst surface), while alkaline HER is hindered by sluggish water dissociation kinetics at the Volmer step. To address these challenges, this thesis explores plasmon-enhanced electrocatalysis as an advanced strategy to modulate interfacial electronic structure and reaction energetics through localized surface plasmon resonance (LSPR). Benefiting from its unique catalytic function and plasmonic response in visible light region, copper (Cu) serves as a versatile platform for constructing Cu-based bimetallic tandem catalysts toward both CO_2 conversion and H_2 production.

This thesis first elucidates the governing mechanisms of plasmon-enhanced electrocatalysis, including electromagnetic near-field enhancement, hot carriers generation and transfer, and localized photothermal heating, as well as their synergistic roles in accelerating reaction rate, stabilizing reaction intermediates, and steering product selectivity. Based on these principles, three representative Cu-based bimetallic systems, CuPd, CuNi and CuAg, were rationally designed and comprehensively investigated through experimental and theoretical studies.

For CO_2RR, a CuPd tandem catalyst was developed by seed growth method. Under resonant illumination, plasmon excitation accelerates *CO formation on CuPd interfacial sites, which subsequently diffuse to Cu sites for coupling, thereby significantly improving the yield of C_2H_4 by 27%. For alkaline HER, a CuNi catalyst was constructed via pulsed electrodeposition to achieve strong interfacial coupling. Hot electrons generated on Cu are rapidly injected into Ni active sites, enhancing water dissociation, while the photothermal heating facilitates mass transport. Remarkably, the illuminated CuNi catalyst delivers performance surpassing commercial Pt. For the CuAg system, Ag nanoneedles serve as highly active *CO formation centers and Cu catalyze *CO protonation toward methane. The balance of the ratio of Ag and Cu sites is highlighted as a key determinant of tandem catalytic selectivity toward hydrocarbon products, with potential of additional enhancement from plasmon excitation.

Overall, this work establishes a unified plasmon engineering approach for Cu-based tandem electrocatalysts that enables efficient CO_2 conversion and green H_2 production. By revealing how plasmon excitation dynamically modulates charge transfer and reaction kinetics at complex bimetallic systems, this thesis provides valuable design principles for

next-generation plasmon-enhanced electrocatalysts and supports the future integration of optical excitation into scalable electrochemical energy systems.

1 Introduction

To address climate change, rising carbon dioxide (CO_2) emissions, and dwindling non-renewable fossil resources, transition to a carbon-neutral energy system has become a global priority and imperative. The production of renewable fuels and chemicals while minimizing environmental impacts are crucial for achieving sustainable development goals. In this regard, electrochemical energy conversion processes driven by clean electricity, particularly those carbon recycling and hydrogen (H_2) production, offer promising solutions. Among these, the carbon dioxide electroreduction reaction (CO_2RR) and the hydrogen evolution reaction (HER) have attracted considerable attention due to their abilities to convert CO_2 and water (H_2O) into energy-rich molecules at ambient temperatures. CO_2RR, by converting CO_2 into valuable hydrocarbon products, contributes to the establishment of a closed-loop carbon system, enabling sustainable carbon recycling and mitigating atmospheric emissions. Combined with the clean H_2 provided by HER, CO_2RR and HER can jointly address the dual challenges of carbon reduction and energy demand, thereby being considered as potential key technologies for the next generation of sustainable energy infrastructure. Despite significant progress in catalyst research for CO_2 and HER in recent years, inherent bottlenecks at the molecular and interfacial levels still significantly limit their application in practical energy conversion systems.

CO_2 is a chemically inert, linear molecule with high thermodynamic stability. This results in a significant activation barrier for the initial proton-electron transfer step to form the key intermediate *COOH (* denotes an adsorbed reaction intermediate on the catalyst surface), which is also a decisive step toward *CO formation. This step is widely considered as the primary kinetic bottleneck in CO_2RR. Furthermore, the formation of hydrocarbon products such as methane (CH_4), ethylene (C_2H_4) and ethanol (C_2H_5OH) requires not only CO_2 activation but also efficient accumulation of the *CO intermediate and subsequent *CO protonation or coupling. Most catalytic surfaces are unable to simultaneously meet these demanding kinetic and adsorption requirements. Copper (Cu), with its moderate *CO binding strength and band structure (which catalyzes *CO protonation and coupling), is the only monometallic catalyst capable of efficiently generating both CH_4 and multi-carbon products (C_{2+}). By combining Cu with other metal catalysts which are highly efficient for the *CO intermediate formation, such as Pd and Ag, the development of Cu-based bimetallic tandem catalysts can enhance the selectivity of CH_4 or C_{2+}. However, Cu-based tandem catalysts still face challenges such as selectivity fluctuations, oxidation state changes, morphological reconstruction, and performance degradation during long-term electrolysis. These limitations highlight the urgent need for precise control of the electronic structure of catalyst surface and intermediate adsorption during CO_2RR to further improve selectivity for specific products and overall catalytic performance.

H_2, as a clean and energy-dense fuel, has the potential to drive deep decarbonization in the chemical, industrial, and transportation sectors, and also plays an indispensable role in renewable energy systems. Although platinum (Pt) exhibits the best catalytic activity in the HER, its scarcity and high cost significantly limit its large-scale commercial application. In contrast, nickel (Ni), with its abundant reserves, low cost, and excellent hydrogen adsorption (*H), has become the mainstream non-precious metal catalyst for the HER under alkaline conditions. However, the rate of HER under alkaline conditions is significantly lower than that in acidic systems, primarily due to the initial Volmer step, which requires the catalytic dissociation of H_2O. This process has a high energy barrier and becomes a kinetic bottleneck for the overall reaction. Therefore, accelerating charge transfer and enhancing H_2O dissociation capabilities of earth-abundant Ni catalyst is crucial for further improving the kinetics of HER.

To overcome these long-standing challenges in CO_2RR and HER, previous studies have explored plasmon-enhanced electrocatalysis as a transformative strategy. When excited by resonant light, metal nanostructures such as Cu, silver (Ag), and gold can exhibit localized surface plasmon resonance (LSPR), generating strong electromagnetic near-fields, energetic hot carriers, and localized photothermal effects. These tunable optical dynamics can alter the interfacial potential, redistribute electrons near the Fermi level, and modify the stability of rate-limiting intermediates. Consequently, LSPR excitation can effectively lower the energy barrier of *CO intermediate and change the reaction pathway in the CO_2RR system, accelerate H_2O dissociation and *H formation in the HER system. In this regime, the catalytic reaction rate and pathway are determined not only by the electrochemical bias and thermodynamic potential but also by the dynamic energy flow of LSPR excitation. This dynamic regulation of charged and thermally activated interfaces provides a powerful and complementary strategy for electrocatalytic control.

Cu serves a dual role as both an efficient CO_2RR catalyst and a visible-light absorber, making it an ideal platform for plasmon-enhanced electrocatalysis. By developing Cu-based bimetallic tandem catalysts, it aims to uniquely combine the CO_2RR catalytic function of Cu with efficient plasmon excitation. Furthermore, Cu, serving as a plasmonic antenna, can be tightly coupled to the highly active and abundant Ni for the alkaline HER. In this CuNi hybrid structure, hot electrons generated by the LSPR transfer from the Cu light absorber to the Ni catalytic center, significantly enhancing the rate of HER without relying on precious metals. These design concepts provide a unified plasmon engineering strategy for carbon cycling and H_2 production. However, the mechanisms of how plasmon excitation influence reaction kinetics remain poorly understood, particularly in complex bimetallic structures, where interfacial charge transfer and thermally induced kinetic changes interact simultaneously. Understanding these mechanisms is crucial for the rational optimization of catalysts and the implementation of future plasmon-enhanced electrochemical technologies. Based on the above challenges, plasmonic Cu-based tandem bimetallic catalysts were designed in this thesis, various experimental and theoretical methods were used to reveal the mechanisms of plasmon enhancement in CO_2RR and HER, thereby providing guidance for the design of the next generation of efficient and stable plasmonic electrocatalysts.

Chapter 2 introduces the fundamental concepts of plasmon-enhanced electrocatalysis. The basic principles of surface plasmons, the background of CO_2RR and HER, and the generation of LSPR effects (localized near-field enhancement, hot-carrier excitation, and photothermal heating) are explained. It further discusses how plasmonic effects can influence the reaction kinetics and product selectivity of CO_2RR and HER. Based on the complementary catalytic roles and plasmonic responses, the rationale for selecting CuPd, CuNi, and CuAg systems is

clarified. Chapter 3 describes the synthesis strategies and characterization methods for CuPd, CuNi, and CuAg systems, establishing the structural basis for later chapters.

Chapter 4 focuses on plasmon-enhanced CO_2RR on CuPd tandem catalysts. Experimental and theoretical analyses demonstrate that plasmon excitation accelerates the formation of *CO on CuPd interfacial sites, and *CO intermediates subsequently diffuse to Cu sites for C-C coupling, thereby improving the selectivity of C_2H_4.

Chapter 5 introduces a CuNi catalyst designed for plasmon-enhanced alkaline HER. Under resonant illumination, the CuNi catalyst exhibits performance surpassing commercial Pt. Both experimental and theoretical results indicate that plasmon-generated hot electrons transferred from Cu sites to Ni sites significantly enhance H_2O dissociation on Ni active sites, while photothermal heating further promotes interfacial mass transport.

Chapter 6 investigates the Cu deposited on Ag nanoneedle substrate for CO_2RR. The Ag nanoneedle sites efficiently generate *CO intermediates, whereas adjacent Cu sites enable their subsequent protonation toward CH_4. This chapter highlights the importance of balancing the ratio of Ag sites which are efficient for *CO generation and Cu sites which are efficient for *CO protonation or coupling to optimize overall catalytic selectivity of hydrocarbon products. Moreover, the CuAg system demonstrates potential for plasmon-enhanced CO_2RR toward CH_4 or C_{2+} products.

In conclusion, this thesis develops Cu-based tandem catalysts that can catalyze CO_2 conversion and green H_2 production, proposes a practical design strategy for plasmon-enhanced electrocatalysis, and improves the understanding of how plasmon excitation interacts with catalysts under electrochemical conditions. These findings support the future integration of optical excitation into scalable electrochemical systems and contribute to the transition toward clean and sustainable energy technologies.

2

Fundamentals of Plasmon-enhanced Electrocatalysis

This chapter introduces plasmonics for electrocatalysis. It explains the Drude model and the distinction between propagating surface plasmon polaritons and localized surface plasmons based on Maier's book.[1] Key concepts of carbon dioxide electroreduction reaction (CO_2RR) and hydrogen evolution reaction (HER) are summarized. Three plasmonic enhancement mechanisms are highlighted with their roles in tuning electrochemical activity and selectivity. Finally, considerations in Copper-based bimetallic tandem systems are addressed for achieving synergistic plasmon-enhanced electrocatalytic performance. Large language models are used to refine the grammars.

2.1 Surface plasmon

This section provides a concise overview of the fundamental principles of surface plasmons based on Maier's book,[1] The reader can find more details in this book, which offers a comprehensive treatment of the foundamentals and applications of plasmonics. Surface plasmons are collective oscillations of conduction electrons at a metal–dielectric interface, strongly coupled to the electromagnetic field. They allow light to be confined and manipulated at the nanoscale, well below the diffraction limit, which makes them central to the field of plasmonics. Two main types are distinguished: surface plasmon polaritons (SPPs), which propagate along extended interfaces, and localized surface plasmons (LSPs), which occur in metallic nanoparticles. Both arise from the same physical principle—the interaction between free electrons in the metal and incident electromagnetic waves.

2.1.1 Electromagnetics of Metals

The starting point for understanding surface plasmons is the characteristic optical response of metals to electromagnetic radiation. In dielectric materials, the electrons are strongly bound to the atomic lattice and can only undergo small displacements when subjected to an external electric field. In contrast, metals contain a high density of conduction electrons that are free to move throughout the lattice. Upon interaction with incident light, these

conduction electrons do not behave as independent particles but instead become coherent, collective oscillations. This collective motion of the electron plasma forms the physical basis of plasmonic excitations, which fundamentally distinguish the optical properties of metals from those of ordinary dielectric materials.

The optical response of metals is fundamentally governed by their dielectric function, which characterizes how the free electron gas interacts with electromagnetic radiation. The optical response of metals over a wide frequency range can be described within the framework of the classical Drude model, which treats conduction electrons as a free electron gas moving against a rigid background of positive ion cores. The starting point is the equation of motion for an electron with effective mass m and charge $-e$, subject to an oscillating external electric field $E(t) = E_0 e^{-i\omega t}$:

$$m\ddot{x} + m\gamma\dot{x} = -eE(t), \tag{2.1}$$

where $\gamma = 1/\tau$ denotes the electron scattering rate and τ the mean collision time. Assuming a harmonic response of the form $x(t) = x_0 e^{-i\omega t}$, the displacement amplitude follows as

$$x_0 = \frac{-e}{m\left(\omega^2 + i\gamma\omega\right)} E_0. \tag{2.2}$$

Each displaced electron contributes a dipole moment $-ex$, and for an electron density n, the macroscopic polarization is given by

$$P = -nex = -\frac{ne^2}{m\left(\omega^2 + i\gamma\omega\right)} E. \tag{2.3}$$

The displacement field relates to the polarization through

$$D = \varepsilon_0 E + P = \varepsilon_0 \varepsilon(\omega) E. \tag{2.4}$$

Hence, the dielectric function of the free electron gas is obtained as

$$\varepsilon(\omega) = 1 - \frac{ne^2}{\varepsilon_0 m\left(\omega^2 + i\gamma\omega\right)}. \tag{2.5}$$

Introducing the plasma frequency,

$$\omega_p^2 = \frac{ne^2}{\varepsilon_0 m}, \tag{2.6}$$

the dielectric function simplifies to

$$\varepsilon(\omega) = 1 - \frac{\omega_p^2}{\omega^2 + i\gamma\omega}. \tag{2.7}$$

This expression describes the contribution of free electrons. In real metals, however, bound (core) electrons also contribute to the polarization at high frequencies. Their effect is accounted for by including a background dielectric constant ε_∞, yielding the final form of the Drude dielectric function:

$$\varepsilon(\omega) = \varepsilon_\infty - \frac{\omega_p^2}{\omega^2 + i\gamma\omega}. \tag{2.8}$$

Here, ε_∞ typically lies between 1 and 10, depending on the material. This model forms the foundation for understanding plasmonic phenomena, as the sign and frequency dependence of $\mathrm{Re}\{\varepsilon(\omega)\}$ determine the ability of metals to sustain plasmonic excitations.

The plasma frequency ω_p is determined by the electron density n, the electronic charge e, the effective mass m^*, and the vacuum permittivity ε_0. For photon energies below the plasma frequency ($\omega \ll \omega_p$), the real part of the dielectric function becomes negative ($\mathrm{Re}\{\varepsilon(\omega)\} < 0$). In this regime, electromagnetic waves cannot propagate inside the bulk of the metal but are instead reflected, which explains the high reflectivity of metals in the visible and infrared spectral ranges. In the low-frequency limit ($\omega \to 0$), conduction electrons screen external fields efficiently, corresponding to $\varepsilon(\omega) \to -\infty$. At very high frequencies ($\omega \gg \omega_p$), the free-electron contribution becomes negligible and the dielectric function tends to the background constant ε_∞, such that metals behave similarly to transparent dielectrics.

Experimentally, plasma frequencies for most metals are found in the ultraviolet, with ω_p typically on the order of 5–15 eV, depending on the details of the band structure. In real metals such as Au and Ag, however, additional absorption channels occur due to interband transitions. For noble metals, these effects already set in for photon energies exceeding about 1 eV, corresponding to wavelengths of order 1 μm. InAu, for instance, the onset of interband transitions occurs at the boundary between the near-infrared and the visible, limiting the validity of the Drude model at optical frequencies. These processes increase the imaginary part of the dielectric function and lead to significant deviations from the free-electron prediction. A more accurate description therefore requires adding Lorentz-type oscillator terms to the Drude response, which account for transitions from filled bands, such as the d-bands in Au and Cu.

Consequently, in the visible and near-infrared frequency ranges, the dielectric function of metals is characterized by a negative real part, allowing for the existence of surface plasmon polaritons at metal–dielectric interfaces.

2.1.2 Surface plasmon polaritons

Surface plasmon polaritons (SPPs) are electromagnetic excitations that propagate along the interface between a dielectric and a conductor, with the fields being evanescently confined in the perpendicular direction. They originate from the coupling between electromagnetic fields and the collective oscillations of the conductor's electron plasma.

The theoretical treatment starts from Maxwell's equations, which can be recast into the wave equation for regions of constant dielectric function. In the absence of external charges and currents, the central equation of electromagnetic wave theory is

$$\nabla^2\mathbf{E} - \frac{\varepsilon}{c^2}\frac{\partial^2\mathbf{E}}{\partial t^2} = 0, \tag{2.9}$$

where $\mathbf{E}$ denotes the electric field vector, ε is the relative dielectric function of the medium, and c is the speed of light in vacuum. To describe propagating solutions, one assumes a harmonic time dependence of the electric field, $\mathbf{E}(\mathbf{r}, t) = \mathbf{E}(\mathbf{r})e^{-i\omega t}$, with ω the angular frequency of the wave. Inserting this form into the central equation of electromagnetic wave theory yields the Helmholtz equation

$$\nabla^2\mathbf{E} + k_0^2\varepsilon\mathbf{E} = 0, \tag{2.10}$$

where $k_0 = \frac{\omega}{c}$ is the wave vector of the propagating wave in vacuum.

For waves bound to a flat metal–dielectric interface, we consider propagation along the x-direction and exponential decay away from the interface along z. Figure 2.1 illustrates the geometry of a single flat interface between a metal and a dielectric. The metal occupies the lower half-space ($z < 0$), while the dielectric lies above ($z > 0$). Surface plasmon polaritons propagate along the interface in the x-direction, with electromagnetic fields that decay exponentially away from the boundary into both media.

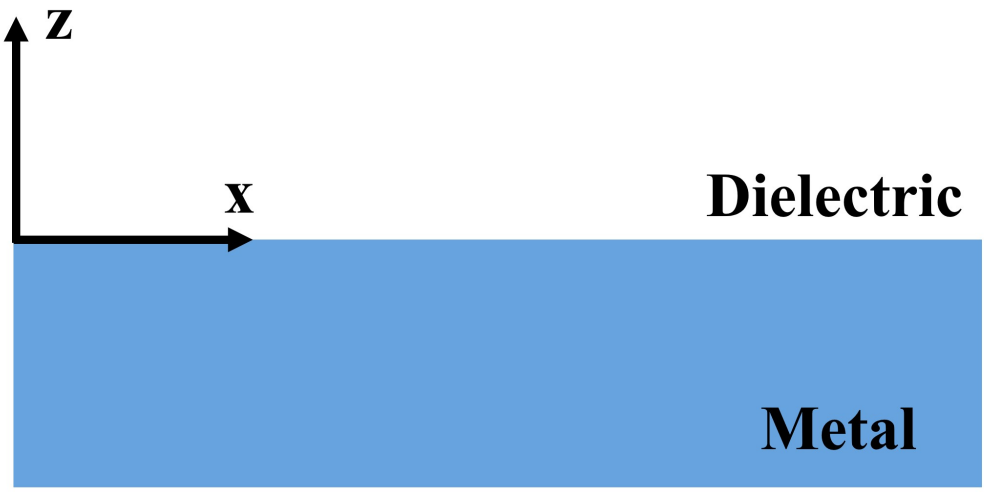

Figure 2.1: Schematic of Metal-Dielectric System. Geometry for surface plasmon polaritons propagation at a single interface between a metal and a dielectric. Adapted with permission from Ref [1].

The solutions of the Helmholtz equation can then be classified into transverse magnetic (TM, or p-polarized) and transverse electric (TE, or s-polarized) modes. Importantly, only TM solutions give rise to confined surface waves. For a metal (ε_1)–dielectric (ε_2) boundary, continuity conditions require that

$$\frac{k_{z,1}}{k_{z,2}} = -\frac{\varepsilon_1}{\varepsilon_2}, \tag{2.11}$$

with $k_{z,i}$ being the perpendicular wave vector components in each medium. This condition demands that the real parts of the permittivities have opposite signs, i.e. surface modes can exist only at conductor/dielectric interfaces. The resulting dispersion relation of SPPs is

$$\beta = k_0 \sqrt{\frac{\varepsilon_1 \varepsilon_2}{\varepsilon_1 + \varepsilon_2}}, \tag{2.12}$$

where β is the propagation constant along the interface. This relation shows that SPPs have larger momentum than light in the dielectric, which explains their confinement and the necessity of special coupling schemes for excitation.

Physically, the fields are bound to the interface, decaying evanescently into both media. The decay length into the dielectric determines the spatial confinement, while losses in the metal (through $\mathrm{Im}\{\varepsilon_1\}$) lead to finite propagation lengths. In multilayer structures, such as insulator/metal/insulator (IMI) or metal/insulator/metal (MIM) geometries, coupling between SPPs at adjacent interfaces gives rise to symmetric and antisymmetric mode splitting. This leads to richer dispersion characteristics, with trade-offs between confinement and propagation length. Finally, the concept of an effective mode length is introduced to quantify energy

localization, which becomes crucial for assessing the degree of sub-wavelength confinement achievable with SPPs.

2.1.3 Localized surface plasmons

In addition to propagating SPPs, plasmonics features another fundamental excitation: localized surface plasmons (LSPs). While SPPs are dispersive, propagating electromagnetic waves bound to a conductor–dielectric interface, LSPs are non-propagating resonances of the conduction electrons in metallic nanostructures coupled to the electromagnetic field. These modes arise naturally from the scattering problem of a small, sub-wavelength metallic nanoparticle in an oscillating electromagnetic field. The curved surface of the particle provides an effective restoring force on the driven electrons, such that a resonance condition can be met. This resonance leads to strong field amplification both inside the particle and in the near-field zone surrounding it, and is termed the localized surface plasmon resonance (LSPR). Unlike propagating SPPs, LSPRs can be excited directly by far-field illumination, without the need for phase-matching schemes.

The physics of LSPs can be explored by considering the interaction of metal nanoparticles with electromagnetic waves in order to derive the resonance condition. Subsequent aspects include damping mechanisms, the influence of particle size and shape on resonance characteristics, and the coupling of plasmons in ensembles of particles. For Au and Ag nanoparticles, the resonance lies in the visible region of the spectrum. A striking manifestation is the appearance of vivid colors in colloidal suspensions or stained glass, caused by resonantly enhanced absorption and scattering. Historically, this effect has been exploited for centuries, while modern applications range from emission enhancement to optical sensing.

The concept of localized surface plasmons can be introduced by considering the simplest geometry: a homogeneous metallic sphere of radius a, characterized by a dielectric function $\varepsilon(\omega)$, embedded in a homogeneous dielectric background of permittivity ε_m. When an external static electric field $\mathbf{E}_0$ is applied, as illustrated in **Figure 2.2**, the conduction electrons in the sphere are displaced relative to the ionic background, leading to an induced dipole moment.

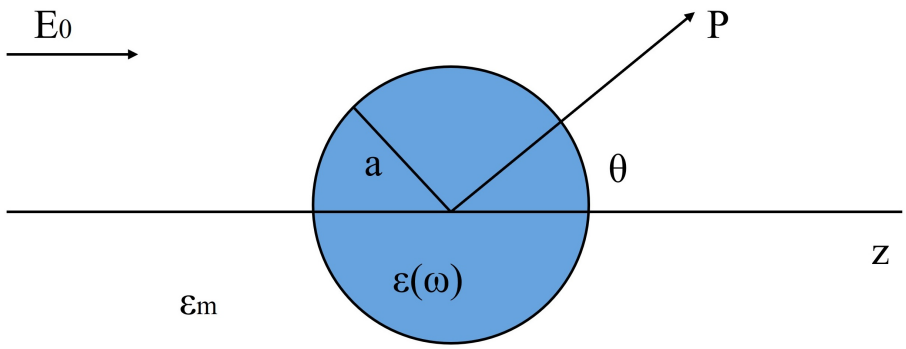

Figure 2.2: Sketch of a homogeneous sphere placed into an electrostatic field. Adapted with permission from Ref [1].

In the quasistatic approximation, valid for particle sizes much smaller than the wavelength of light ($a \ll \lambda$), the problem reduces to solving Laplace's equation for the scalar potential,

$$\nabla^2 \Phi = 0, \tag{2.13}$$

inside and outside the sphere. The boundary conditions at the sphere surface (r = a) require continuity of the potential and of the normal component of the displacement field. Solving this problem yields an induced dipole moment $\mathbf{p} = \alpha \mathbf{E}_0$, with the polarizability given by

$$\alpha(\omega) = 4\pi a^3 \frac{\varepsilon(\omega) - \varepsilon_m}{\varepsilon(\omega) + 2\varepsilon_m}. \tag{2.14}$$

This expression shows that the polarizability depends both on the particle volume (a^3) and on the dielectric contrast between the metal and the surrounding medium. A resonance occurs when the denominator approaches zero, i.e. when

$$\mathrm{Re}[\varepsilon(\omega)] = -2\varepsilon_m, \tag{2.15}$$

which is known as the Fröhlich condition. At this frequency, the polarizability is strongly enhanced, corresponding to the excitation of a dipolar localized surface plasmon resonance (LSPR). Physically, this resonance describes the collective oscillation of the conduction electron cloud against the restoring force of the positive ion background, confined to the nanoparticle. It results in pronounced local field enhancement both inside and near the particle, forming the basis of many plasmonic phenomena such as surface-enhanced Raman scattering and fluorescence enhancement.

Beyond the simple case of a homogeneous metallic sphere, localized surface plasmon resonances (LSPRs) can be generalized to nanostructures of different geometries and compositions. For ellipsoidal particles, the resonance condition depends on the depolarization factors along each principal axis, which leads to distinct resonances associated with oscillations of the conduction electrons along different axes. In particular, elongated particles such as nanorods exhibit resonances that are spectrally red-shifted with increasing aspect ratio, allowing the plasmon frequency to be tuned into the near-infrared region. Furthermore, core–shell particles consisting of a dielectric core and a thin metallic shell support hybridized plasmon modes. These structures provide additional flexibility for tailoring the spectral response, as their polarizability contains contributions from both the inner and outer interfaces of the shell.

For particles with dimensions comparable to the wavelength of light, the quasi-static approximation is no longer valid, and a full electrodynamic treatment is required. This is provided by Mie theory,[2] which describes the scattering and absorption of electromagnetic waves by a sphere. While the quasi-static model predicts a single dipolar resonance, Mie theory reveals the presence of higher-order multipolar modes and accounts for retardation effects that shift and broaden the resonance. Additionally, damping mechanisms such as radiation damping and absorption through interband transitions play an important role in determining the linewidth and lifetime of LSPRs.

Finally, the concept of localized plasmons can be extended beyond metallic particles to more complex systems such as void plasmons in metallic hosts and nanoshell geometries, where coupling between sphere-like and cavity-like modes gives rise to hybridized resonances. These generalized cases highlight the versatility of localized surface plasmons as tunable excitations, forming the foundation for their widespread applications in sensing, field-enhanced spectroscopy, and nanophotonics.

2.2 Electrocatalysis

Electrocatalysis, the study of catalytic processes that govern charge transfer at electrified interfaces, underpins many key technologies in renewable energy conversion and sustainable chemical synthesis. By enabling selective and efficient pathways for multi-electron reactions, electrocatalysts address the kinetic and thermodynamic limitations inherent to electrochemical transformations. Within this context, two reactions are of central importance to this thesis: CO_2RR and HER. CO_2RR not only offers a strategy to mitigate greenhouse gas emissions but also provides a route to generate value-added carbon-based products.[3] HER represents the cornerstone of clean hydrogen production and serves as a fundamental benchmark for assessing catalytic activity.[4] Together, these reactions exemplify the dual challenges of achieving both high activity and selectivity in electrocatalyst design.

2.2.1 CO_2 electroreduction reaction

Background of CO_2RR. Since the Industrial Revolution, global CO_2 emissions have continued to rise. In 2024, CO_2 emissions from fossil fuels and cement reached a new high of 37.4 Gt, placing significant pressure on the climate system. Global warming has exacerbated the frequency of extreme weather events. This trend underscores the urgency and necessity of CO_2 emissions reduction.[5]

Key strategies for addressing CO_2 from industrial sources, such as fossil fuels, include CO_2 capture and storage (CCS) and CO_2 catalytic conversion and utilization (CCU). A recent review notes that while CCS is included in the critical pathways of many climate models and has recently been rapidly promoted, its historical project failure rate is high, and medium- and long-term growth remains constrained by technical complexity, energy consumption, cost, and public acceptance. Only a few scenarios truly achieve large-scale, durable storage. Risks such as leakage and high energy consumption are also detailed in recent literature, indicating that CCS is not the ultimate solution.[6] In contrast, CCU offers the dual benefits of carbon reduction and resource utilization. It can convert CO_2 into energy carriers and chemicals, contributing to the promotion of a circular economy, and is considered to have a greater long-term development potential. Current CO_2 conversion pathways include thermal catalytic hydrogenation, bioconversion, photocatalytic reduction, and electrocatalytic reduction.[7] CO_2RR is considered a key approach to achieving carbon neutrality and building a green chemical industry due to its mild reaction conditions, renewable electricity-driven power, and diverse product offerings, which offer both environmental and industrial benefits.[8]

Since Hori et al. first discovered in 1985 that Cu electrodes can efficiently reduce CO_2 to various hydrocarbons under mild conditions,[9] theoretical and experimental research on the CO_2RR has rapidly developed and made important progress, becoming a cutting-edge research topic in electrochemistry and green catalysis. However, the practical application of CO_2RR still faces key challenges: The low solubility of CO_2 in the electrolyte leads to limited mass transfer and sluggish kinetics, and competes strongly with HER, reducing energy efficiency and current utilization. Large-scale applications are still hampered by insufficient catalyst durability and inadequate scale-up optimization of reactor systems (e.g., the efficiency and uniformity of gas diffusion electrodes and membrane electrode assemblies decrease under long cycles, high current densities, and scale-up conditions).[10] Therefore, continuing to develop new, efficient, low-cost, and highly selective catalysts and promoting system engineering and industrial demonstrations are key future research directions.

Mechanistic overview of CO_2RR. A CO_2RR system typically consists of two components: a cathode and an anode, as shown in Figure 2.3. The cathode side includes a working electrode (catalyst) and a reference electrode, while the counter electrode in the anode is often made of an inert material (such as platinum). The two sides are separated by a proton exchange membrane or an ion exchange membrane, effectively preventing cross-contamination of products.[11] The CO_2RR primarily occurs at the catalyst/electrolyte interface in the cathode, involving the adsorption and activation of CO_2 molecules, electron-proton transfer of intermediates, and desorption of the final products. Simultaneously, water oxidation, known as the oxygen evolution reaction (OER), occurs in the anode, releasing proton (H^+), which migrates through the membrane to the cathode to participate in the CO_2RR.[12]

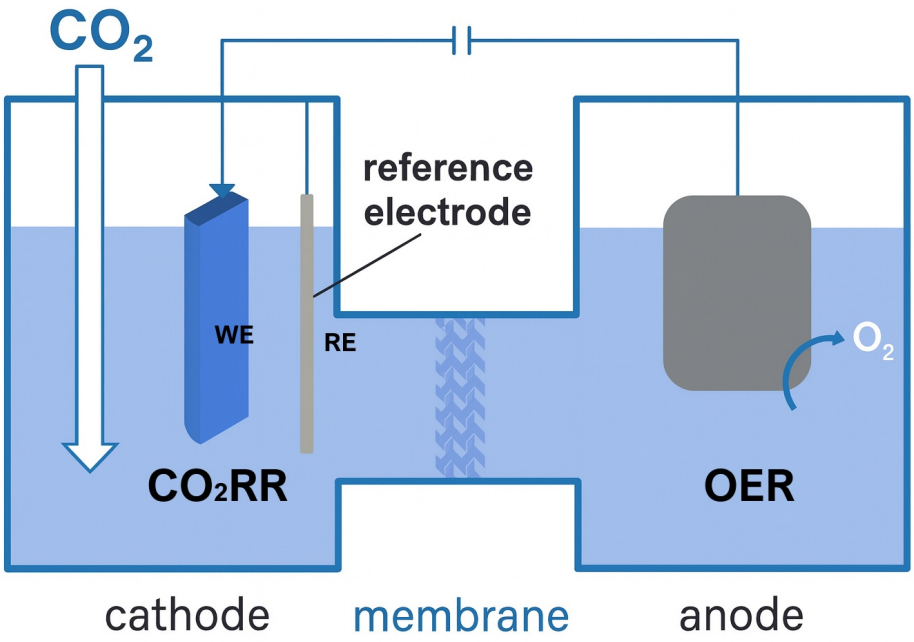

Figure 2.3: Schematic diagram of CO_2RR. Schematic illustration of a three-electrode electrochemical cell for CO_2RR at the cathode and OER at the anode, separated by a membrane. WE: working electrode, RE: reference electrode. Adapted with permission from Ref [13].

At the molecular level, the first step in CO_2 activation is the adsorption of CO_2 at the active site of catalyst surface. CO_2 is a chemically inert linear molecule, and breaking its C=O double bond is the primary thermodynamic barrier to the overall reaction, which requires considerable energy around 750 kJ mol^{-1}. On an effective catalyst surface, electron injection bends the CO_2 molecular structure and generates an activated CO_2 adsorption intermediate, significantly lowering the reduction barrier of molecule.[14] Next, various active intermediates are formed through electron transfer and/or proton migration. Finally, the reduction products are desorbed from the electrode surface and diffuse into the electrolyte. The number of transferred electrons and standard hydrogen electrode potential of different reduction products are shown in Table 2.1.[15]

The pathways of different products are simply described, as shown in Figure 2.4. Firstly, CO_2 combines with protons to form key intermediates such as *HCOO or *COOH (* represents the intermediate adsorbed on the catalyst surface). Then the *HCOO accepts a proton and an electron to yield *HCOOH, while the *COOH dehydrates to form the *CO intermediate.[16] *CO, as a key intermediate for C_1 and C_{2+} products, can either directly desorb to form CO gas or undergo C-C coupling or multi-step electron/proton transfer (e.g., *CO–CO, *CHO, *COH, *CHO–CHO, *COH–COH) on the catalyst surface, further generating multi-carbon

Reaction equation	Product	E° (V vs. SHE)
$CO_2 + 2H^+ + 2e^-$	$CO + H_2O$	−0.10
$CO_2 + 2H^+ + 2e^-$	$HCOOH + H_2O$	−0.12
$CO_2 + 6H^+ + 6e^-$	$CH_3OH + H_2O$	0.03
$CO_2 + 8H^+ + 8e^-$	$CH_4 + 2H_2O$	0.17
$2CO_2 + 12H^+ + 12e^-$	$C_2H_5OH + 3H_2O$	0.09
$2CO_2 + 12H^+ + 12e^-$	$C_2H_4 + 4H_2O$	0.08
$2H_2O$	$O_2 + 4H^+ + 4e^-$	1.23
$2H^+ + 2e^-$	H_2	0.00

Table 2.1: CO_2RR, OER and competing HER with their standard hydrogen electrode potentials (Carbon monoxide (CO), formic acid (HCOOH), methanol (CH_3OH), methane (CH_4), ethanol (C_2H_5OH), ethylene (C_2H_4), oxygen (O_2), hydrogen (H_2)). Reproduced with permission from Ref [15].

compounds such as C_2H_4 and C_2H_5OH. This determines the distribution and selectivity of the final products.[17]

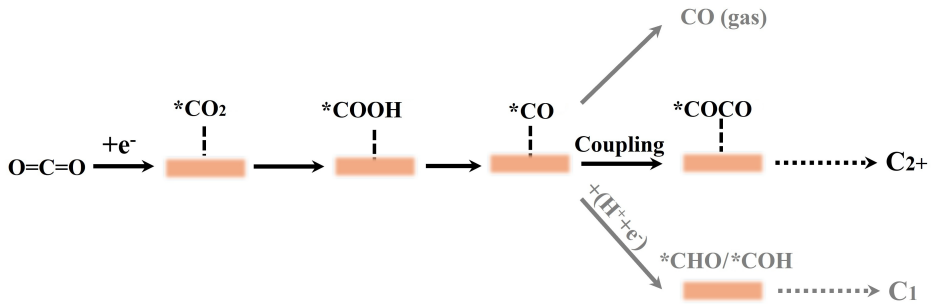

Figure 2.4: Schematic illustration of CO_2RR Pathway. Simplified pathway of the CO_2RR, showing the conversion of CO_2 into CO gas, C_{2+} products, and C_1 products.

Catalysts for CO_2RR. Catalysts for CO_2RR are primarily categorized into metal catalysts, non-metal catalysts, and molecular catalysts.[18,19] Among them, non-metallic catalysts primarily include carbon-based materials (such as carbon nanotubes, graphene, and carbon quantum dots), organic small molecules, and non-metallic single-atom catalysts.[20,21] These catalysts have been extensively studied due to their low cost, large surface area, and tunable structure. Carbon-based catalysts offer the advantages of diverse morphologies and abundant active sites. Their activity can be further enhanced by doping with heteroatoms such as nitrogen, phosphorus, or sulfur, thereby modulating their electronic properties and catalytic behavior. Recent research progress has focused on precisely controlling active sites through optimized synthesis methods, nanostructures, and computational design to improve catalyst efficiency and stability. For example, non-metallic single-atom catalysts, in which isolated non-metallic atoms (iodine, phosphorus) are anchored on carbon supports, can improve catalystic efficient and selective due to altered electronic structure and enhanced mass transfer.[22,23] Despite these advantages, they also face challenges, such as improving long-term stability and activity under harsh reaction conditions. Metal-free catalysts represent a dynamic and evolving class of catalysts that offer cost-effective, tunable, and sustainable alternatives to traditional metal catalysts and are increasingly used in the energy, environmental, and chemical industries.

Molecular catalysts, particularly metal complexes, are a class of catalysts composed of a central metal atom or ion coordinated by organic or inorganic ligands.[24] The structure and catalytic mechanisms of these catalysts are highly tunable, as the metal center and its surrounding ligands can be precisely controlled, influencing the catalyst's electronic properties and reactivity.[25] Metal complexes, such as phthalocyanines, porphyrins, and bipyridine-based

catalysts, are frequently studied molecular catalysts.[26] They often mimic the function of enzymes by providing well-defined active sites and can be designed to efficiently catalyze reactions under mild conditions. Another advantage of molecular catalysts is that their discrete, uniform active sites enable detailed mechanistic studies, allowing researchers to precisely monitor reaction intermediates and pathways. However, despite these advantages, molecular catalysts often face stability challenges. Particularly under harsh reaction conditions, such as high current density or corrosive environments, the metal center may undergo demetallation, ligand degradation, or structural changes, shortening the catalyst lifetime. Addressing these stability issues is an active area of research, including strategies such as immobilization on supports, ligand design to enhance catalyst stability, and development of protective environments to prolong catalyst activity.[27] Emerging approaches like dynamic protonation of ligands and optimizing electronic interactions with supports also show promise. Molecular catalysts offer a unique combination of tunability and selectivity, but further improvements in stability are needed for widespread practical applications in energy conversion, green synthesis, and environmental technologies.

Metal catalysts include monometallic catalysts, copper-based alloys and multimetallic catalysts. Monometallic catalysts are categorized based on their primary product into those that produce CO (such as Pd, Au, Ag, and Zn),[28] those that produce formic acid (such as Bi, Sn, In, and Pb),[29] those that produce H2 (such as Ni, Fe, and Pt), and the specialized metal Cu that catalyzes the conversion of CO_2 to multiple carbon products.[30,31] Cu-based alloys and multimetallic catalysts enhance C–C coupling by manipulating electronic structure and surface defects, improving catalytic activity and product selectivity.

Due to its unique electronic structure and surface properties, Cu can efficiently convert CO_2 into a variety of high-value-added multi-carbon products, such as ethylene, ethanol, and methane. Therefore, Cu and Cu-based catalysts have become the core of research on the electrocatalytic reduction of CO_2 to produce multi-carbon high-value-added products.[32] The Cu surface crystal planes (such as Cu(100), Cu(111), Cu(110)), oxidation state (Cu^0 and Cu^+), and rich structural morphologies (nanoparticles, nanowires, twins, etc.) synergistically affect product distribution and catalytic selectivity.[33,34] For example, Cu(100) is conducive to ethylene production, while Cu(111) is more inclined to methane production.[35,36] High-density twin boundaries can significantly reduce the intermediate reaction energy barrier and improve the selectivity of methane and multi-carbon products.[37]

Copper-based bimetallic or multimetallic catalysts, composed of copper in combination with other metals (such as palladium, silver, nickel, gold, and zinc), are important systems for CO_2RR. Two main structural manipulation strategies—alloying and heterostructures—respectively tailor the electronic structure and active site distribution, significantly improving the efficiency and selectivity of C_{2+} products.[38] Each structural manipulation approach has its own advantages and unique mechanisms. For alloy catalysts, copper and other metals (such as gold, palladium, nickel, and zinc) are uniformly mixed at the atomic scale, resulting in a synergistic effect that optimizes intermediate adsorption and reaction energy barriers. For example, controlling the Au content in Cu-Au alloys significantly improves CO production efficiency and suppresses the formation of methane byproducts.[39] Cu-Ni alloys optimize the reaction pathway by manipulating the adsorption energy of intermediates such as *CO, thereby increasing selectivity for multi-carbon products.[40] Cu–Pd alloy catalysts exhibit enhanced efficiency and selectivity for CO_2RR to CH_4, owing to their ability to modulate intermediates adsorption and suppress C–C coupling through the construction of favorable electronic structures and surface reaction environments.[41] In contrast, heterostructured catalysts, such as Cu-Ag, Cu-Pd, and Cu-Au, achieve spatial separation of active sites through

heterogeneous interfaces or core-shell structures, enabling tandem catalysis.[42,43] One of the metals primarily reduces CO_2 to CO, while the intermediate CO migrates to the copper site to complete a C-C coupling reaction, generating multi-carbon products. This tandem catalysis effectively overcomes the sluggish kinetics of the C-C coupling reaction at the copper active site, significantly improving the Faradaic efficiency and yield of multi-carbon products.

Despite the outstanding performance of copper-based catalysts in CO_2 electroreduction, including multi-dimensional improvements in structural design, alloy synergy, and tandem mechanisms, they still face challenges such as catalytic stability, high overpotential, and competition for hydrogen evolution.[44] Future development efforts will focus on dynamic structural control, increasing the number of highly active polyhedral facets/defects, and optimizing reaction processes to achieve long-term catalyst efficiency and industrial viability.[45]

CO_2RR Performance Metrics. The performace of CO_2RR catalysts is primarily determined by parameters such as Faraday efficiency (FE), overpotential, current density, Tafel slope, and stability. These metrics provide a comprehensive understanding of catalyst selectivity, activity, energy efficiency, kinetics, and stability in CO_2RR.[46]

The FE for CO_2RR quantifies the proportion of electrons used to produce the desired product during electrolysis relative to the total charge transferred, accurately assessing the electron utilization efficiency of each product.[47] The mathematical expression of FE of any CO_2RR product can be described by the following formula:

$$FE = \frac{z \cdot n \cdot F}{Q} \times 100\%$$

where z represents the number of electrons required for per mole of product (e.g., for CO_2 to CO, z=2), as shown in Table 2.1, n represents moles of the specific generated product, F represents the Faraday constant (96485 C/mol), Q represents total charge passed during the experiment, usually as the integrated current over time. For gaseous products (such as CO, C_2H_4, H_2, and CH_4), the molar number of each product is measured by gas chromatography, while it is analyzed using liquid chromatography or liquid nuclear magnetic resonance for liquid products. The total charge passed during the experiment was measured by the electrochemical workstation. The result is multiplied by 100% to obtain the percentage. FE indicates the selectivity and efficiency of the catalyst toward the target product. An FE close to 100% indicates that almost all electrons are used to produce the desired product. A lower FE indicates that electrons are also consumed in undesirable side reactions.[48]

Overpotential is the extra voltage required beyond the thermodynamic equilibrium potential to drive the reaction at a meaningful rate. Lower overpotentials are indicative of more efficient catalysts, as less energy is needed to drive the reaction.[49] Overpotentials are also connected to selectivity. Certain catalysts can achieve desired products at lower overpotentials, often owing to optimized surface structures and reaction pathways.[50]

Current density reflects the rate at which electrons are delivered per unit area of the electrode. Higher current densities signal high catalytic activity and potential for industrial scalability. However, maintaining selectivity and stability at elevated current densities presents a challenge, as mass transport limitations and competing reactions (such as hydrogen evolution) may arise.[51]

The Tafel slope, derived from the plot of overpotential (η) vs. the logarithm of current density ($\log j$), reveals the reaction kinetics and mechanistic pathways. A small Tafel slope suggests a fast electron-transfer process and efficient catalytic kinetics. Analysis of Tafel

slopes helps identify rate-determining steps and enables targeted improvements in catalyst design.[52]

Stability assesses the ability of a catalyst to maintain its performance (FE, activity, selectivity) over extended operational periods. Long-term stability is imperative for practical applications. It is monitored through continuous operation (often up to hundreds of hours) and by observing structural or morphological changes in the catalyst that could lead to degradation or decreased selectivity. Stability can be enhanced through catalyst design and system engineering.[53]

2.2.2 Hydrogen evolution reaction

Background of HER. The HER is a key electrochemical process for sustainable hydrogen production via water splitting. The high energy density, renewability, and carbon-neutral combustion make H_2 a promising energy carrier for decarbonizing the transportation, industrial, and power sectors. The HER operates in both acidic and alkaline electrolytes, with the cathodic half-reaction coupled with the anodic OER. Optimizing HER catalysis is crucial for minimizing energy losses, lowering overpotential, and improving H_2 production efficiency, thereby enhancing the viability of H_2 as a clean fuel.[54]

The growing global focus on renewable energy is driving the development of robust, cost-effective, and scalable HER catalysts. While platinum group metals (PGMs) remain the benchmark for catalysts due to their excellent catalytic performance, their scarcity and high cost have prompted the exploration of abundant non-precious metal systems and non-metal catalysts. Simultaneous advances in understanding the HER mechanism and evaluating its performance are facilitating the rational design of catalysts for practical application in industrial electrolyzers.[55]

Mechanistic overview of HER. HER proceeds through several basic steps that vary slightly depending on the pH of the electrolyte,[56,57] but generally include:

1. Volmer Step (Electrochemical Adsorption): In acidic media, this involves proton reduction:

$$H^+ + e^- \rightarrow {}^*H \tag{2.16}$$

In alkaline media, water reduction occurs:

$$H_2O + e^- \rightarrow {}^*H + OH^- \tag{2.17}$$

Here, *H represents the surface-adsorbed H intermediate.

2. Hydrogen Formation Steps: Heyrovsky step (Electrochemical desorption):

$$^*H + H^+ + e^- \rightarrow H_2 \quad \text{(acid)} \tag{2.18}$$

$$^*H + H_2O + e^- \rightarrow H_2 + OH^- \quad \text{(alkaline)} \tag{2.19}$$

Tafel step (Chemical recombination):

$$^*H + {}^*H \rightarrow H_2 \tag{2.20}$$

Recent advances in spectroscopy, theoretical modeling, and computational simulations have unveiled more intricate mechanistic pathways, including variations influenced by proton

sources, electrolyte composition, and interfacial environments.[58,59] Sophisticated catalysts can facilitate such processes, enabling more complex reaction dynamics.[60]

Catalysts for HER. The catalytic activity for the HER is often described by the classical volcano relationship, which correlates hydrogen binding energy ΔG_{H*} to HER performance, encapsulating the Sabatier principle.[61] According to this framework, an ideal HER catalyst binds hydrogen neither too weakly nor too strongly, striking a balance that ensures efficient proton/electron transfer and rapid hydrogen desorption.

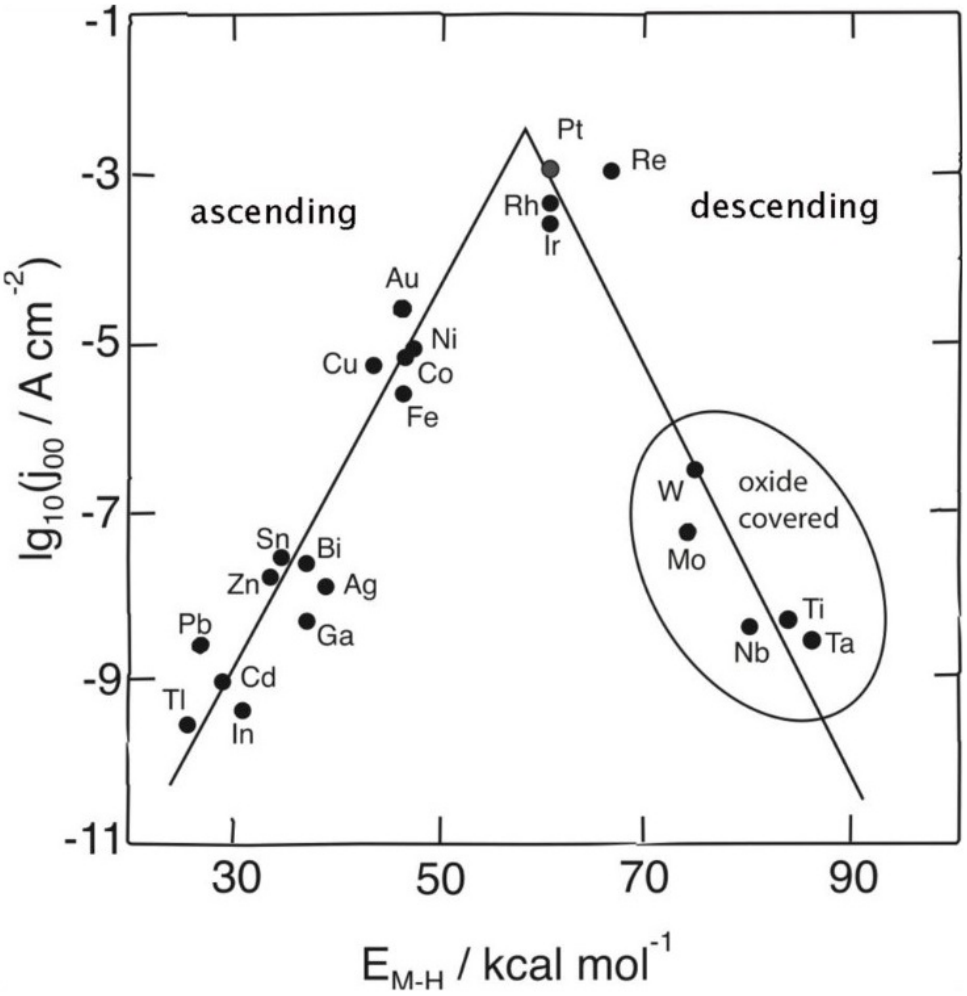

Figure 2.5: Volcano plot of HER. Trassati's volcano plot for the HER in acid solutions. j_{00} denotes the exchange current density, and E_{MH} denotes the energy of hydride formation. Reproduced with permission from Ref [62].

As shown in Figure 2.5, metals such as Au, Ag, and Cu are placed on the left side of the volcano because their weak hydrogen adsorption leads to poor proton activation and sluggish kinetics. Conversely, W and Mo reside on the right side due to overly strong binding, which hinders hydrogen desorption and reduces catalytic turnover. Platinum (Pt) is located at the apex, possessing nearly optimal hydrogen binding that yields exceptional activity and minimal overpotential. Noble metals like Pd, Rh, and Ir cluster near the peak but trail behind Pt in performance. This volcano trend underpins why Pt is the benchmark HER catalyst and drives catalyst design toward fine-tuning hydrogen adsorption energy—by alloying, forming heterostructures, or modulating electronic properties—to approach the region near the volcano's apex for superior catalytic efficiency.[63,64]

Next, we classify HER catalysts. The 1st, Pt group metals (PGMs) catalysts, notably Pt, exhibit near-optimal hydrogen binding energy, affording unmatched catalytic activities with ultra-low overpotentials and favorable kinetics.[65] However, resource scarcity and high costs limit its possibility of large-scale industrial application. Other PGMs, such as Pd, Rh, and Ir, have been explored but confront similar scalability challenges. The applications of PGMs are limited to laboratory and small scale. The 2nd, significant effort has been devoted to developing non-noble metal alternatives, including transition metal sulfides (MoS_2, WS_2), phosphides (Ni_2P, CoP), carbides (Mo_2C, WC), and selenides, which offer promising catalytic properties attributed to their tunable electronic structures and exposed active edge sites.[66] The 3nd, alloy and heterostructures, such as NiMo, CoNi, integrate synergistic effects, optimize hydrogen binding and enhance charge transfer kinetics while improve stability.[67] Structural and electronic modulation allows fine-tuning of active sites to suit either acidic or alkaline media. The 4th, the carbon-based materials and single-atom catalysts have drawn substantial attention in recent years, owing to their high atomic utilization and customizable electronic structures. Nitrogen-doped carbon frameworks and graphene-supported transition metals exemplify this approach, providing robust performance and superior stability across a range of operating conditions.[67] Single-atom catalysts, featuring isolated atomic sites, maximize catalytic efficiency while allowing precise modulation of activity. These strategies together constitute a comprehensive approach to HER catalyst design, emphasizing synergistic effects, structural engineering, and atomic-level control to attain both high performance and stability in sustainable hydrogen production systems.

In parallel with experimental work, machine learning (ML) models have recently demonstrated remarkable capability in accelerating catalyst discovery by predicting hydrogen adsorption energies and catalytic activities with high accuracy and reduced computational cost.[68] These computational frameworks guide experimental efforts by identifying promising candidates, which are not easily accessible via traditional DFT alone.

Despite significant progress, enhancing the intrinsic activity of non-noble metal HER catalysts remains a bottleneck. Stability under harsh acidic or alkaline conditions, scalability of synthesis methods, and integration into industrial electrolyzer systems require further work. The transition from half-cell lab measurements to full-cell, industrially relevant environments poses additional challenges in maintaining performance and durability.[69] Future research should develop in the following aspects: (1) Rational design of multi-component heterostructures exploits synergistic effects to enhance performance; (2) Development of robust metal-free and SAC catalysts with tailored electronic structures; (3) Machine learning-guided high-throughput screening accelerates the discovery of high efficient catalysts; (4) In-depth mechanistic investigations employing operando techniques provide critical insights to guide catalyst design at atomic and molecular levels; (5) Innovation in electrode architectures and integration drive the development of practical electrolyzer devices.

HER Performance Metrics. Benchmarking H_2 evolution catalysts across a comprehensive suite of electrochemical metrics, which is crucial for comparing and improving materials.[70] Standardized protocols remain crucial to ensure reproducibility and facilitate industrial translation. There are some benchmark metrics below. (1) Overpotential (η): Measured at benchmark current densities such as 10 mA cm^{-2}, reflecting the extra voltage beyond thermodynamic potential to drive HER. (2) Tafel Slope: Serves as a mechanistic probe. Slopes near 120, 40, and 30 mV dec^{-1} indicate Volmer, Heyrovsky, and Tafel rate-determining steps, respectively. (3) Exchange Current Density (j_0): Quantifies intrinsic catalytic activity at equilibrium potential; higher implies more active sites or superior site activity. (4) Turnover Frequency (TOF): Represents the number of H_2 molecules generated per active site per unit

time, providing insight into catalyst efficiency beyond surface area effects. (5) Stability: Essential for practical applications, requires long-term chronoamperometric or cycling tests to assess catalyst robustness. (6) FE: Indicates efficiency of electron utilization toward H_2 generation. Ideally, it is close to 100%.

2.3 Principles of plasmonic electrocatalysis

Plasmonic electrocatalysis couples light-excited plasmonic nanostructures with electrochemical interfaces to modulate reaction pathways under applied bias. Upon resonant illumination, localized surface plasmon resonance (LSPR) concentrates electromagnetic energy into subwavelength volumes and decay through radiative and non-radiative channels. The latter generates hot carriers (electrons and holes) and ultimately heat, all within the electrical double layer (EDL) where bond making/breaking occurs. These effects—near-field enhancement, hot carrier generation, and photothermal effect—can lower activation barriers, shift adsorption equilibria, and alter selectivity in multi-electron reactions. In this thesis, we leverage these plasmonic effects to promote two target reactions: CO_2RR and HER, using Cu-based bimetallic systems engineered to balance optical response, catalytic activity, and stability.

2.3.1 Mechanism and Distinguishing of plasmonic effect

Near-field enhancement. LSPR arises from the collective oscillation of conduction electrons in metallic nanostructures upon illumination by incident light. This oscillation results in charge displacement at the metal–dielectric interface, producing intense localized electromagnetic fields that decay rapidly with distance, as shown in Figure 2.6, typically within 10–30 nm from the nanoparticle surface. Sharp geometries such as tips, edges, and nanogaps amplify the local field through geometric confinement, occasionally generating near-field 'hot spots' with field intensities up to $10^4 - 10^6$ times higher than the incident light field.[71,72] The buildup and dephasing of these near-fields occur on ultrafast timescales, often within 10–100 fs after excitation, consistent with femtosecond-resolved pump-probe spectroscopy of LSPR dynamics.[73]

The local field strength generated by LSPR can modulate the potential energy surface (PES) of adsorbed reactants through the Stark effect, thereby lowering activation barriers and stabilizing transition states, a phenomenon analogous to electrostatic field catalysis where electric fields influence reaction kinetics and pathways, as demonstrated in plasmon-driven surface reactions and photoelectrochemical studies.[72,74] Meanwhile, the spatial confinement of electromagnetic energy enables efficient photon coupling with adsorbates, active sites, and adjacent semiconductor supports. Such near-fields not only facilitate enhanced optical absorption and surface-enhanced spectroscopy but also drive plasmon-induced resonance energy transfer (PIRET), through which energy transfer from plasmonic metals to molecular adsorbates or semiconductors enhances photoactivity and catalysis rates.[75] Moreover, due to the exponential decay of near-fields, catalytic enhancement predominantly occurs at hot spots, making morphology engineering (sharp tips, nanogaps, core–shell structures) and interparticle arrangement (arrays, spacing) essential for aligning these hot spots with active catalytic sites, thereby steering reaction selectivity and efficiency in plasmon-enhanced electrocatalysis.[76,77]

Hot-carrier generation and transfer. Plasmon decay proceeds through either radiative scattering or nonradiative Landau damping, with the latter transferring plasmon energy to energetic electron–hole pairs within femtoseconds (approximately 20–100 fs), as shown in Figure 2.6. These nonthermal carriers subsequently undergo electron–electron scattering over 100 fs to 1.5 ps, forming a hot Fermi–Dirac distribution, and then dissipate energy to the lattice via electron–phonon scattering within 1–10 ps. The final stage of phonon–phonon relaxation releases heat into the surrounding environment on a timescale of 0.1–10 ns.[76,78] In noble metals, hot-carrier excitation involves both intraband (sp→sp) and interband (d→sp) transitions; Au and Cu benefit from low-lying d bands supporting visible-light d→sp excitations, whereas Ag predominantly undergoes intraband transitions due to deeper d bands.[71,74]

Once generated, hot carriers can transfer to reaction intermediates via two principal pathways. In the indirect transfer process, carriers first form in the metal and, if sufficiently energetic, are injected into unoccupied molecular orbitals of adsorbates, producing transient negative ions; this process occurs within 100 fs to 10 ps and is strongly dependent on energy level alignment and coupling strength. Alternatively, in the direct transfer mechanism—also termed chemical interface damping—photons drive transitions across strongly hybridized metal–adsorbate or metal–semiconductor orbitals, enabling ultrafast (5–100 fs) charge injection; this pathway bypasses bulk hot-carrier generation, improves interfacial selectivity, and reduces recombination losses.[72,75] In metal/semiconductor heterostructures, Schottky barriers can act as unidirectional filters to extend carrier lifetimes.[77]

The electrochemical potential further dictates carrier utilization: under cathodic bias, hot electrons accumulate and favor reduction reactions, whereas anodic conditions promote hole-driven oxidation. In either case, hot carriers transiently modify local charge density, oxidation states, or defect structures at catalytic centers, thereby tuning adsorption energetics and reaction pathways.[73] For example, in CO_2 reduction electrocatalysis, direct carrier transfer selectively populates interfacial states associated with specific reaction channels, enhancing product selectivity, while indirect injection tends to distribute energy more broadly and thus lowers efficiency.[74]

Photothermal heating. Following plasmon decay, hot carriers dissipate their excess energy through electron–phonon scattering on a timescale of approximately 1–10 ps, which results in a transient increase in lattice temperature, as shown in Figure 2.6. The accumulated heat is subsequently transferred to the surrounding medium over 0.1–10 ns, establishing localized temperature gradients at the electrode–electrolyte interface.[73,75]

In the context of electrocatalysis, photothermal effects influence reactions through several interconnected mechanisms. First, local heating accelerates charge-transfer kinetics according to the Arrhenius relation, effectively reducing activation barriers and leading to exponential increases in reaction rates; this behavior is distinguished from hot-carrier-driven processes, which often exhibit linear scaling with light intensity.[72] Second, photothermal heating alters diffusion coefficients and can induce thermal convection, thereby enhancing mass transport.[73] Finally, the mild and localized nature of photothermal heating ensures that interfacial processes are promoted without inducing bulk temperature rises that could compromise catalyst stability, thereby offering a means to accelerate electrocatalytic reactions while preserving the structural integrity of plasmonic nanostructures.[74,77]

Distinguishing plasmonic effects. Experimentally, distinguishing different plasmonic effects can be approached via the dependence of reaction rates on light intensity, where a linear or superlinear dependence indicates hot-carrier processes.[79] An Arrhenius-type exponential dependence, linked to light-induced temperature rise, is a hallmark of photothermal

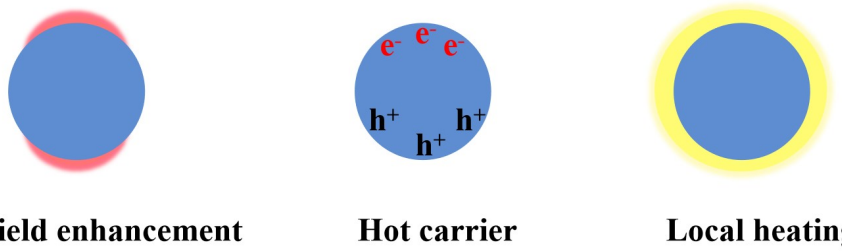

Figure 2.6: Three effects induced by the LSPR. Reproduced with permission from Ref [75].

heating.[80] Time-resolved photocurrent measurements under chopped illumination provide additional mechanistic insight. Rapid current rises on millisecond or sub-millisecond timescales reflect hot-carrier injection or near-field effects, while slower photocurrent over seconds is characteristic of photothermal contributions.[81] Spike-like photocurrent responses may further signify plasmoelectric effects.[82] By selectively using the LSPR resonant wavelength and the interband transition threshold wavelength for excitation (e.g., the d→sp transition in Au or Cu), the different responses of the reaction activity to wavelength can be used to determine the dominant mechanism.[83] Spectroscopic techniques such as transient absorption, time-resolved photoluminescence, and surface-enhanced vibrational spectroscopy offer direct evidence on carrier lifetimes, electronic coupling at interfaces, and vibrational mode enhancement.[84] Lastly, kinetic isotope effects (KIE) serve as diagnostic tools. Pronounced isotope effects often indicate hot-carrier-dominated pathways, while photothermal-driven reactions mimic conventional thermal catalysis without significant isotope sensitivity.[85,86]

Theoretical modeling provides essential complementary tools to experimental studies of plasmonic effects. Characteristic time and energy scales offer key insights: near-field plasmonic enhancements form and decay within femtoseconds and extend spatially over tens of nanometers. Hot carriers are generated and undergo relaxation on ultrafast femtosecond to picosecond timescales, while photothermal heating manifests more slowly, typically from picoseconds to nanoseconds due to lattice heating dynamics.[87] Electromagnetic simulations, including finite-difference time-domain (FDTD) and boundary element methods (BEM), effectively quantify localized field distributions and enhancement factors, aiding identification of near-field contributions. Electronic structure methods such as density functional theory (DFT) and time-dependent DFT (TDDFT) can describe interband and intraband excitations. They allow estimation of hot-carrier energy distributions and help analyze interfacial charge-transfer pathways, which makes it possible to distinguish direct from indirect hot-carrier injection.[88] Photothermal effects are evaluated via thermal modeling approaches such as finite element method (FEM) or heat diffusion simulations, which estimate the local temperature rise under illumination. If the predicted temperature increase quantitatively explains reaction rate enhancements following Arrhenius kinetics, a photothermal mechanism is indicated.[89] Finally, Kinetic models that combine hot-carrier generation, relaxation and transfer rates with catalytic turnover can be used to quantitatively separate the roles of near-field enhancement, hot carriers, and photothermal heating.

2.3.2 Plasmon-enhanced CO_2RR

Plasmon-enhanced CO_2RR has attracted considerable attention as a strategy to mitigate the limitations of conventional electrocatalysis, including sluggish CO_2 activation, large overpotentials, and poor product selectivity. This approach is based on LSPR, a phenomenon occurring in metallic nanostructures such as Au, Ag, and Cu. Upon light irradiation, the collective oscillation of conduction electrons gives rise to enhanced local electromagnetic

fields, the generation of hot carriers (electrons and holes), and localized thermal effects. These processes can lower activation barriers, promote charge transfer, and modify reaction pathways.[75]

Au-based catalysts are well known for their intrinsic selectivity toward CO formation and their high chemical stability. Recent studies demonstrate that under plasmonic excitation, Au nanoparticles not only enhance CO production but also enable methanol formation, with Faradaic efficiencies (FE) up to 52% under 520 nm illumination for particles with diameters of approximately 20 nm.[90] The plasmonic response of Au is strongly dependent on morphology and surface facets, with octahedral nanostructures exhibiting more pronounced light-induced enhancements.[91] Furthermore, the integration of Au nanostructures into flow-cell configurations has been shown to improve both mass transport and light-driven selectivity, increasing FE(CO) from 64% to 85% and reducing the required overpotential.[92] Ag-based catalysts provide an abundant and lower-cost alternative to Au, with well-established selectivity for CO production. Under light illumination, Ag thin-film electrodes have demonstrated a significant increase in FE(CO), from 15% to 95% at -0.6 V versus RHE under 365 nm excitation.[93] In situ ATR-SEIRAS spectroscopy revealed that the strong local electric field generated by LSPR changes the interfacial environment of the Ag electrode (e.g., enhancing HCO_3^- binding and increasing the local pH), promoting the desorption of surface-adsorbed CO, thereby increasing the CO yield at low overpotential and suppressing the HER.[94] Moreover, plasmonic excitation enables the tuning of CO/H_2 ratios across a broad range (35:1 to 1:1), providing an important opportunity for the controlled production of syngas.[95]

Cu-based catalysts are distinguished by their ability to produce C_{2+} products such as ethylene and ethanol, although they typically require high overpotentials and suffer from limited selectivity. Recent work on Cu nanowire arrays revealed pronounced plasmonic effects, including increased current density, reduced charge-transfer resistance, and enhanced CO selectivity relative to the competing hydrogen evolution reaction (HER).[96] These enhancements have been attributed primarily to the accumulation of hot electrons. In addition to single-metal systems, multi-metal plasmonic catalysts have been developed to exploit the strong LSPR activity of Au and Ag in combination with the catalytic versatility of Cu and other transition metals. For example, Cu–Ag nanostructures exhibited light-enhanced production of CO, ethylene, methane, formate, and allyl alcohol, while simultaneously suppressing HER.[97] $Ag/Cu_2O/CuO$ dendritic electrodes achieved a Faradaic efficiency of 54% for acetate formation at -0.4 V under illumination.[98] Recent studies on CuPd tandem catalysts showed that plasmon excitation can boost C_2H_4 production by 27% via hot-electron and photothermal effects at the Cu–Pd interface, thereby facilitating *CO formation and C–C coupling.[99] These findings highlight the advantages of combining plasmonic excitation with catalytic functionality to achieve improved activity, selectivity, and durability.

In summary, plasmon-enhanced CO_2RR provides a light-assisted electrocatalytic pathway that leverages electromagnetic field, hot-carrier dynamics and photothermal heating effects to overcome key kinetic and selectivity barriers associated with CO_2RR. Au, Ag, and Cu each offer distinct benefits: Au enables methanol formation in addition to CO, Ag provides tunable syngas production with high CO selectivity, and Cu facilitates access to C_{2+} products. Multimetallic systems further demonstrate the potential of integrating plasmonic and catalytic components for synergistic performance enhancement. These advances establish a foundation for the rational design of plasmonic nanostructures aimed at efficient and selective CO_2 conversion under light-assisted conditions.

2.3.3 Plasmon-enhanced HER

Plasmonic nanostructures have recently emerged as highly promising promoters of HER, owing to their ability to harvest light and channel the resulting energy into chemical transformations. When resonantly illuminated, plasmonic metals such as Au, Ag, and Cu can generate energetic charge carriers, strong near fields, and localized heat, which together modify the interfacial energetics of HER. The most effective enhancement typically arises when the excitation wavelength matches the localized surface plasmon resonance (LSPR) of the nanostructure and when carrier transport pathways are engineered through nanoscale heterostructures. This unique synergy provides a pathway to lower reaction barriers, optimize intermediate binding, and increase charge transfer kinetics, thereby offering a viable route toward efficient photo-electrocatalytic hydrogen production.[73]

A diverse range of plasmonic architectures has been designed to enhance HER, including plasmonic–catalytic metal hybrids (e.g., AgPt-Au nanostars,[100] Au-Rh nanoflowers,[101] Pt/Fe-Au nanorods[102]), metal–semiconductor junctions (e.g., Au-TiO_2-Pt,[103] Au@MoS_2[104]), and hybrids with 2D materials,[105] or MOFs[106]. These systems exploit light absorption, carrier lifetime extension, and interfacial engineering to optimize hydrogen binding and reaction kinetics. Across these materials, characteristic performance signatures consistently point to plasmonic enhancement: activity peaks near the LSPR resonance, reductions of 10–50 mV in overpotential under illumination, improved Tafel slopes, and lower charge-transfer resistance observed by EIS.

Three plasmonic effects are particularly relevant for HER. First, hot-carrier injection enables plasmonically excited electrons to transfer into adjacent catalytic sites, where they participate directly in proton reduction.[101] This contribution is readily identified through light-on/off current or potential differences, as well as wavelength-dependent performance following the plasmon extinction spectrum. Second, near-field enhancement generates intense electromagnetic "hot spots" that amplify local reaction rates and simultaneously tune the free energy of hydrogen adsorption (ΔG_{H^*}), thereby accelerating the Volmer or Tafel steps.[105] Third, photothermal effects arising from non-radiative plasmon decay elevate local temperatures, which promotes water dissociation and charge transfer.[107] While these effects are often intertwined, careful experimental design—such as pulsed illumination, flow cells, or thermal imaging—can help disentangle their respective roles.

From these studies, several design principles can be distilled. Effective systems position light absorption directly at or near catalytic sites, ensuring that hot carriers are generated where they can be most effectively utilized. Tuning the LSPR via size, shape, or dielectric environment enables spectral matching with illumination sources. Interface engineering, such as controlling shell thickness and optimizing band alignment, minimizes recombination losses. Despite these advances, challenges remain in quantitatively distinguishing hot-carrier and photothermal contributions, extending long-term stability to hundreds of hours, and standardizing performance metrics. Addressing these issues will be essential for translating plasmon-enhanced HER from proof-of-concept demonstrations into robust, scalable technologies for solar-to-hydrogen conversion.

2.3.4 Considerations in selecting CuPd, CuNi, and CuAg systems

Cu is an abundant and cost-effective material with remarkable catalytic properties for CO_2RR. Uniquely among single metals, it can catalyze the formation of multi-carbon products such

as ethylene and ethanol.[74] Moreover, Cu exhibits LSPR in the visible spectrum, which can enhance catalytic activity and product selectivity through local electric field effects, hot-carrier generation, and photothermal heating. These characteristics make Cu a highly promising candidate for plasmon-enhanced CO_2RR and related reactions, such as HER.

For CO_2RR, Pd demonstrates strong CO adsorption capacity along with fast kinetics for CO formation, whereas Cu uniquely facilitates C–C coupling toward the generation of multi-carbon products.[108] The integration of Pd's CO adsorption characteristics with the dual plasmonic and catalytic functions of Cu endows the CuPd system with optimized catalytic performance, making it a promising candidate for plasmon-enhanced CO_2RR aimed at producing valuable multi-carbon products.

Ni is an earth-abundant and relatively inexpensive metal, widely recognized for its outstanding electrocatalytic performance toward the HER, particularly under alkaline conditions.[109] Its intrinsic catalytic activity enables efficient proton reduction to hydrogen, primarily due to the favorable hydrogen adsorption energies on Ni surfaces. In contrast, Cu alone is not considered a highly active HER catalyst; however, its visible-light plasmonic response can be exploited to enhance the photochemical driving force for HER. Within CuNi bimetallic systems, Cu contributes by improving light absorption and generating plasmonic hot carriers, which in turn accelerate charge transfer processes and amplify the HER activity localized at Ni active sites. Such CuNi systems thus offer an optimal balance of cost-effectiveness, catalytic efficiency, and plasmon-enhanced photoactivation, positioning them as promising candidates for photoelectrochemical hydrogen production.

Ag is widely recognized as a highly selective catalyst for the CO_2RR to CO. Since CO serves as a key intermediate in the subsequent formation of C_{2+} products on Cu, the ability of Ag to efficiently generate CO strongly complements intrinsic capability of Cu for C-C coupling and multi-carbon product formation. The integration of Cu with Ag therefore enables a tandem catalytic pathway.[97] Beyond their complementary catalytic roles, both Cu and Ag possess pronounced LSPR responses within the visible spectrum. Under visible-light excitation, the plasmonic properties of these two metals can act cooperatively. Such synergistic plasmon–catalytic interactions are expected to accelerate charge transfer processes, improve reaction kinetics, and increase product selectivity. Consequently, CuAg systems represent promising candidates for plasmon-enhanced CO_2RR, offering a rational strategy to achieve efficient and selective conversion of CO_2 into valuable multi-carbon products.

In summary, the rational design of Cu-based bimetallic systems such as CuPd, CuNi, and CuAg leverages the complementary catalytic and plasmonic properties of the constituent metals. The synergistic interplay between catalytic functionality and plasmonic effects in these systems not only optimizes product selectivity and reaction kinetics, but also broadens the applicability of Cu-based catalysts across CO_2RR and HER. These considerations highlight the strategic potential of Cu–M (M = Pd, Ni, Ag) alloys as promising platforms for plasmon-enhanced electrocatalysis and photoelectrochemical energy conversion.

3 Methodology

3.1 Synthesis

This chapter summarizes the preparation procedures of catalysts and the analytical methods used to evaluate their structures and properties, providing the foundation for subsequent performance and mechanism studies.

3.1.1 Synthesis of CuPd sample

Chemicals. Chemicals used were Copper acetate ($\geq$ 99.99%), Palladium acetate ($\geq$ 99.9%), 2-ethoxyethanol ($\geq$ 99%), Sodium borohydride ($\geq$ 98.0%), Potassium carbonate ($\geq$ 99.999%), ethanol ($\geq$ 99.8% (GC)), isopropyl alcohol ($\geq$ 99.8% (GC)). All chemicals were purchased from Sigma-Aldrich and used without any further purification. Milli-Q water at 25 °C was used in all experiments. Carbon (mesoporous, nano powder graphitized 99.95%, trace metals basis), Nafion (perfluorinated resin solution, 5wt% in lower aliphatic alcohols and water, contains 15-20% water), Deuterium oxide (deuteration degree min. 99.9% for NMR spectroscopy) and Dimethyl sulfoxide (ACS reagent $\geq$ 99.9%) were also purchased from Sigma-Aldrich. Carbon paper (Sigracet 39BB) was purchased from Fuel cells Etc and cut into 0.5 cm * 2 cm. The CuPd, Cu, Pd samples were synthesised by a previously reported method.[108,110]

Synthesis of Cu sample: 3 mmol of copper acetate was thoroughly dissolved into 250 mL of 2-ethoxyethanol with vigorous stirring and N_2 bubbling. After 30 min, 20 mL of $NaBH_4$ aqueous solution (1.5 M) was dropwise added into the above solution. The obtained black precipitate was washed with water and ethanol several times. The collected Cu sample was dried in vacuum.

Synthesis of Pd sample: 3 mmol of palladium acetate was first dissolved into 30 mL of acetone, then 250 mL of 2-ethoxyethanol was added. Stir evenly, 20 mL of $NaBH_4$ aqueous solution (1.5 M) was dropwise added into the mixture solution. The obtained black precipitate was washed with water and ethanol several times and dried in vacuum.

Synthesis of CuPd sample: 1.5 mmol of palladium acetate was dissolved into 10 mL of acetone. 250 mL of 2-ethoxyethanol was added and heated to 120 °C for 30 min with vigorous stirring and Ar bubbling. After cooling to room temperature, 20 mL of copper acetate aqueous solution (75 mmol/L) was dropwise added and followed by 20 mL of $NaBH_4$ aqueous solution (1.5 M). The obtained black precipitate was thoroughly washed with water and ethanol and dried in vacuum.

3.1.2 Synthesis of CuNi sample

Chemicals.$NiSO_4{\cdot}6H_2O$ ($\geq$ 98.0%), $CuSO_4{\cdot}5H_2O$ ($\geq$ 98.0%), and $Na_3C_6H_5O_7$ ($\geq$ 99.0%) were purchased from Sigma-Aldrich. Potassium hydroxide (EMPLURA) was bought from Merck KGaA. Toray Carbon Paper (TGP-H-060) was used in our experiments. All chemicals were used as received without further purification.

Synthesis of CuNi sample: We first prepared the electrodeposition solution by dissolving 2.62 g $NiSO_4{\cdot}6H_2O$, 0.05 g $CuSO_4{\cdot}5H_2O$, and 2.94 g $Na_3C_6H_5O_7$ in 100 mL deionized water (DIW), followed by adjusting the solution pH to 4.2 with 1 M H_2SO_4. Before deposition, the TGP-H-060 substrate was hydrophilized by oxygen plasma treatment for 10 min. Then, CuNi cocatalysts were deposited onto 0.25 cm^2 carbon paper via pulse deposition with 0.2 s on and 0.8 s off per cycle, using a three-electrode configuration. A Pt foil and an Ag/AgCl electrode (saturated in 3.0 M KCl) were used as the counter and reference electrodes, respectively. For the deposition of pure Cu and pure Ni, $NiSO_4{\cdot}6H_2O$ and $CuSO_4{\cdot}5H_2O$ were respectively omitted while maintaining all other deposition parameters.

3.1.3 Synthesis of CuAg sample

Chemicals. Chemicals used were Potassium carbonate ($\geq$ 99.999%), base and curing agent, which were purchased from Sigma-Aldrich and used without any further purification. PDMS was obtained by mixing base and curing agent with a ratio of 10:1. Milli-Q water at 25 °C was used in all experiments.

Sythesis of Ag nanoneedle: The Ag nanoneedle (NND) sample was provided by our cooperator, then we processed the sample according to their method and then conducted the tests.[111] Briefly, Ag NND was obtained by thermal evaporation on commercial AAO templates, with the rate of 0.5 Å/s and thickness of 2.0 μm. After that, 5 wt% NaOH solution was used to remove the templates, then distilled water was used to remove the residual NaOH solution. Ultimately, the Ag NND film was put on PDMS solution with dring at 80 ℃ for 30 min.

Synthesis of AgCu-30s and AgCu-30s samples: AgCu-30s and AgCu-30s samples were obtained by electrodeposition method according to our collaborators.[111] The 0 V_{RHE} was applied in 30 mL of 0.5 mM $CuSO_4{\cdot}5H_2O$ electrolyte for 30 s and 180 s to obtain AgCu-30s and AgCu-30s samples, respectively. After that, controlling the area of the samples to 0.5cm*0.5cm for test with nail polish covering the excess area.

Synthesis of AgCu-5nm, AgCu-10nm and AgCu-50nm samples: The Ag NND sample were placed on the holder of the e-beam evaporator with the current of 125 mA and at a rate of 0.1 Å/s, choosing Cu as source. Evaporating thickness of 5 nm, 10 nm and 50 nm Cu on Ag NND substrates, denoting as AgCu-5nm, AgCu-10nm and AgCu-50nm. Then these samples were annealed at 150 °C under argon (Ar) atmosphere for 1 h. After that, controlling the area of the samples to 0.5cm * 0.5cm for test with nail polish covering the excess area.

3.2 Characterization

3.2.1 Microscopies

Scanning Electron Microscopy (SEM). SEM is a surface and near-surface imaging technique with nanometer-scale resolution. It is commonly used to observe surface topography and roughness; identify defects such as particles, pores, and cracks, as well as fracture features; examine the layered structure and approximate thickness of thin films; and compare different compositions and phases using backscattered electrons (BSE). Furthermore, combined with energy dispersive spectrometry (EDS), it can identify elements and create compositional distribution maps.

Essentially, a SEM scans a focused electron beam across a sample's surface point by point, generating signals from the surface layer down to tens of nanometers deep. The interaction between the incident electrons and the material produces a variety of signals, which are collected by detectors and converted into an image. Secondary electrons primarily originate from the surface layer (1–5 nm) and are suitable for analyzing surface topography and roughness. Backscattered electrons originate from deeper layers (approximately 10–100 nm), and the signal increases with increasing atomic number, allowing for the separation of different components or phases based on brightness or darkness. Imaging resolution is influenced by probe size, beam current and acceleration voltage, working distance, sample geometry, and charging effects. Insulating samples often require conductive coatings or the use of low-voltage or variable-voltage SEMs to suppress charging.

In summary, SEM is widely used in materials analysis because of its large field depth, high resolution, and ability to combine multiple signals.

Transmission Electron Microscopy (TEM). TEM uses a high-energy electron beam (80–300 kV) to transmit ultrathin samples (<100 nm). Electrons undergo elastic/inelastic scattering and coherent interference with atoms, forming real-space images (HRTEM) or selected-area electron diffraction (SAED) through the objective lens. In scanning TEM (STEM) mode, the nanoprobe scans point by point, and high-area electron diffraction (HAADF) can be used to obtain significant Z contrast. TEM can reveal the morphology and size of nanoparticles, pores, and layered structures in detail. SAED or image FFT is used for phase identification and unit cell/orientation analysis. HRTEM directly visualizes lattice fringes with atomic-level resolution, identifying dislocations, twins, stacking faults, and interfaces. Combining EDS and EELS with STEM provides spatially resolved elemental and chemical state mapping. HAADF-STEM is particularly suitable for compositional and layer sequence analysis of complex nanostructures, such as core-shell systems. TEM samples must be sufficiently thin. In addition, since the electron beam may cause surface rearrangement and beam damage, a low dose, low voltage, and reasonable collection strategy are required. Moreover, the particle size of the CuPd nanoparticles was measured using the DigitalMicrograph software.

3.2.2 Spectroscopies

X-ray Diffraction (XRD). XRD is an important characterization technique widely used in materials research. Its main applications include determining the phase composition of a sample by comparison with a standard database (PDF card), calculating lattice constants and stress/strain, assessing crystallinity, estimating grain size, and revealing crystal orientation preferences.

XRD essentially reflects the interaction between X-rays and the periodically arranged atoms in a crystal. A crystal structure can be viewed as consisting of a large number of periodically arranged lattice points, each of which is populated with atoms or ions. When a beam of X-rays with a wavelength on the order of magnitude of the interatomic distance (approximately 0.1–0.2 nm) strikes a crystal, each atom in the crystal acts as a scattering center, emitting scattered waves in all directions.

In disordered atomic systems (such as amorphous phases or liquids), the phase relationships of the scattered waves are random and mostly cancel each other, resulting in only weak observed scattering. In contrast, in periodically arranged crystals, X-rays scattered from adjacent crystal planes exhibit a fixed path difference. When the path difference is not an integer multiple of the wavelength, the scattered waves experience phase differences, partially or even completely canceling out each other, resulting in no distinct diffraction peaks. When the path difference satisfies the Bragg's law:

$$2\mathrm{d}\sin\theta = \mathrm{n}\lambda \tag{3.1}$$

where n is the diffraction order (usually 1), λ is the X-ray wavelength, d is the interplanar spacing, and θ is the angle of incidence. In this case, the scattered waves remain in phase, undergoing constructive interference in specific directions, adding their intensities, and producing a strong diffraction peak. Therefore, diffraction signals are only observed at certain angles θ.

The interplanar spacing (d) can be calculated using Bragg's law. The intensity of XRD diffraction peaks is related to atomic scattering factor, crystal orientation, and crystal plane arrangement. Peak shape parameters (particularly the half-width at half-maximum) can be used to estimate not only grain size and microstrain but also crystallinity. Generally speaking, the sharper the diffraction peak, the higher the crystallinity.

X-ray Photoelectron Spectroscopy (XPS). XPS is a surface-sensitive characterization technique. It can be used for element identification and quantification, as well as determination of chemical valence states and local chemical environments. XPS utilizes the photoelectric effect generated by X-ray excitation to perform energy spectrum analysis. Incident photons excite inner-shell electrons out of the surface, where their kinetic energy $\mathrm{E_K}$, is measured by the energy analyzer. According to the law of conservation of energy:

$$\mathrm{E_B} = \mathrm{h}\nu - \mathrm{E_K} - \phi$$

where $\mathrm{E_B}$ is the binding energy, hν is the photon energy, and ϕ is the analyzer work function which is calibrated in practical XPS measurements. Different elements/shells have characteristic $\mathrm{E_B}$. Chemical shifts for the same element vary depending on the chemical environment. Spin-orbit coupling can lead to peak splitting.

The peak positions of XPS are used to identify elements and their chemical states. After correcting the peak areas and performing peak separation, the atomic percentage of each element in the surface layer can be semi-quantified, as well as the relative content of different chemical states of the same element. In summary, due to high sensitivity and chemical state resolution at the surface nanoscale, XPS is particularly critical in the research of catalysis, electrochemical interfaces, thin films, and semiconductor materials.

4

Plasmon-enhanced electroreduction CO_2 reaction on CuPd tandem catalyst

The content of this chapter is published in the scientific journal Journal of the American Chemical Society (Zhu, L., Liu, K., Li, H. J., Mei, Z., Kang, Y., Chen, Q., Wang, X., Zhang, H., Zi, X., Wang, Q., Fu, J., Pensa, E., Stefancu, A., Liu, M., Cortés, E. Plasmon-Enhanced C_2H_4 Generation in the CO_2 Electroreduction Reaction on a CuPd Tandem Catalyst. Journal of the American Chemical Society, 2025, 147(36), 33003-33017.).[99] *This chapter is based on the peer-reviewed manuscript, incorporating text elements such as words, sentences, full paragraphs, along with graphic content and figures, all sourced directly from the publication. In accordance with the Journal of the American Chemical Society publication guidelines that allow the reuse of an author's own work in theses or dissertations, in compliance with the American Chemical Society's permissions policy. Further permissions or reuse are governed by the ACS AuthorChoice or RightsLink licensing system as applicable.*

4.1 Research background

Plasmon-enhanced electrocatalysis. Plasmon-enhanced electrocatalysis attracts much attention due to its ability to enhance the activity of electrocata-lytic processes such as CO_2 electroreduction reaction (CO_2RR),[91,112,113] hydrogen evolution reaction (HER),[114–117] oxygen reduction reaction,[118,119] and more.[120–122] Plasmonic nano-materials such as Cu, Ag and Au exhibit localized surface plasmon resonances (LSPR) in the optical (i.e. sunlight) regime.[123,124] The interaction between light and the free metal electrons concentrates light at the nanoscale, amplifying local electric fields by over three orders of magnitude.[125] This phenomenon leads to absorption cross-sections much larger than the physical size of the nanostructures, enabling efficient light absorption. Upon LSPR excitation, their energy can decay either through the scattering of resonant photons or by generating energetic charge carriers.[126] These charge carriers can transfer energy to adsorbed molecules or dissipate by heating the metal lattice.[127] The local electric field enhancement, hot carrier generation and photother-mal effect have been utilized in electrochemistry to accelerate chemical reactions (enhancing efficiency) or influence reaction pathways (improving selectivity).[128–130] Despite the potential of plasmonic effect in electrocatalysis, the field remains in its early stages,

especially for CO_2RR.[131,132] Maximizing the use of all the energy pathways derived from the plasmon decay is one of the greatest challenges in plasmonic catalysis.

To produce C_{2+} compounds from CO_2RR, the reaction involves two key processes: the first is the reduction of CO_2 to *CO intermediate (* represents intermediates absorbed on catalyst surface),[133,134] and the second is C-C coupling.[133] Copper (Cu), a plasmonic metal in the visible range of the electromagnetic spectrum, is capable of catalyzing C-C coupling reactions,[135–139] offering a promising avenue for plasmon-driven CO_2RR to generate valuable C_{2+} chemicals and fuels.[140] Additionally, a second metal (co-catalyst) which is favourable for *CO generation, such as Ag,[141–143] Au[144–146] and Pd[108,147–151] is often introduced to develop Cu-based bimetallic catalysts.[152] For example, phase-seperated CuPd nanoparticles (NPs) have been shown to enhance C2 prod-ucts formation, with *CO generated at Pd and CuPd inter-face sites, and Cu sites catalyzing subsequent C-C coupling steps.[153] The performance of such tandem catalysts for CO_2RR upon plasmon excitation is a frontier topic.

In this study, tandem catalyst CuPd NPs was used to explore the role of plasmon resonances in enhancing the C_2H_4 formation during CO_2RR. Our results show that under LSPR excitation (625 nm LED) at -1.3 V_{RHE}, C_2H_4 produc-tion on CuPd NPs increased by 27.0%, CO production decreased by 11.4%, compared to the dark conditions. Through photocurrent response, COMSOL simulations, DFT calculations and in-situ FTIR spectroscopy, we identi-fied the mechanisms driving the selective C_2H_4 generation under plasmon excitation. The increase in C_2H_4 production is mainly attributed to plasmon-induced hot electrons and heating promoting the *CO formation on CuPd interface sites. Subsequently, *CO diffusion from the CuPd interface to Cu sites results in increased *CO coverage on Cu sites, which decrease the energy barrier of C-C coupling and promotes C_2H_4 generation. Plasmon excitation also in-creased the H2 production on CuPd NPs by 26.6%, primarily due to photothermal effect. This study highlights the potential of plasmon resonances to improve the selectivity of high-value C2 products from CO_2RR, presenting signifi-cant opportunities for exploration and innovation in the emerging field of tandem plasmonic catalysts.

4.2 Results and discussion

Catalysts preparation and characterization.

The CuPd, Cu and Pd NPs were prepared by wet chemical reduction method. As shown in Figure 4.1a and 4.1b, the obtained CuPd sample exhibits a quasi-spherical morphology with average diameters ranging from approximately 15 nm for Cu and 55 nm for Pd, respectively. The HAADF-STEM image shows uniformly distributed bright-contrast nanoparticles, and the corresponding EDS elemental maps clearly reveal the presence of Cu (green) and Pd (red). The overlapping of Cu and Pd signals suggests that the CuPd NPs are composed of Pd NPs decorated with multiple Cu NPs. The high-resolution TEM (HRTEM) images of CuPd NPs in Figure 4.1c, provide detailed insights into the crystalline structure of the CuPd NPs. The yellow markings indicate the measured lattice spacings of Cu(111) (0.206 nm), CuO(100) (0.232 nm), Pd(111) (0.227 nm), and Pd(100) (0.196 nm) planes, confirming the coexistence of Cu- and Pd-related phases. The red lines highlight the Cu-Pd interfaces, suggesting strong interficial contact between Cu and Pd domains. Overall, the combination of HAADF-STEM, EDS mapping, and HR-TEM results verifies that the synthesized CuPd NPs exhibit a bimetallic structure with phase-seperated distribution and well-defined Cu–Pd interfaces. Meanwhile, Cu and Pd nanoparticles (NPs) were prepared as control samples. As shown in Figure 4.2, the synthesized Cu and Pd samples both exhibit a quasi-spherical

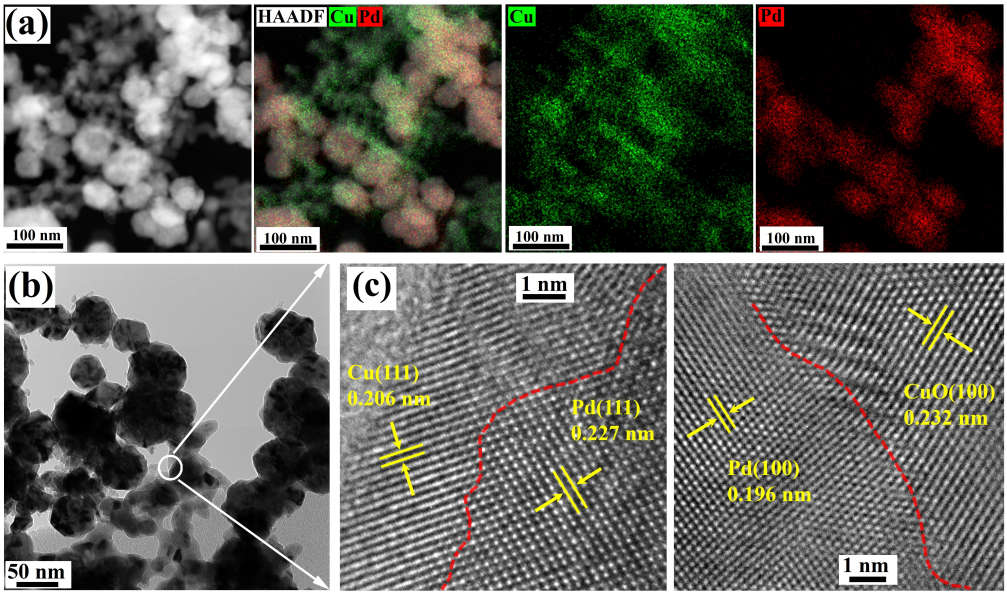

Figure 4.1: STEM/TEM images of CuPd NPs. (a) High-angle annular dark-field scanning transmission electron microscopy (HAADF-STEM) image and corresponding energy-dispersive X-ray spectroscopy (EDS) elemental mapping of the CuPd sample (Cu in green and Pd in red). The scale bars in the insets represent 100 nm. (b) Transmission electron microscopy (TEM) of CuPd NPs (scale bar: 50 nm). (c) High-resolution TEM (HR-TEM) images of CuPd NPs (scale bar: 1 nm). The average distances between the fringes in the HRTEM images and the corresponding Cu and Pd facets are marked in yellow, while red lines highlight the Cu–Pd interfaces.

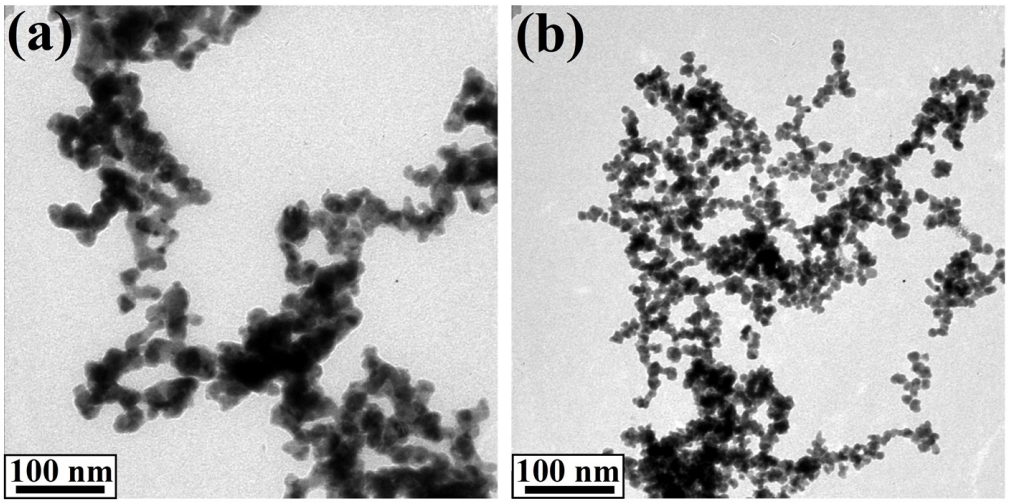

Figure 4.2: TEM images of (a) Cu and (b) Pd NPs. The scale bars in the insets represent 100 nm.

morphology with uniform contrast in the TEM images. The average particle sizes of the Cu NPs and Pd NPs are approximately 10 nm and 15 nm, respectively.

The XRD patterns of CuPd, Cu and Pd NPs in Figure 4.3a show that the CuPd NPs exhibit distinct diffraction peaks of Cu and Pd, such as Cu(111), Cu(200), Pd(111), and Pd(200). This indicates that the CuPd NPs retains the individual crystalline characteristics of Cu and Pd rather than forming alloy, suggesting a phase-separated structure. Figure 4.3b shows the XRD patterns after the electrochemical reduction treatment under -1.3 V_{RHE} for 1 hour. The diffraction peaks associated with oxidized Cu species almost disappear, and only metallic Cu and Pd peaks are detected. This result demonstrates that the oxidized Cu species are effectively reduced to the metallic state during the electrochemical reduction process. Therefore, the influence of oxidized Cu on the reaction products can be neglected in subsequent electro-

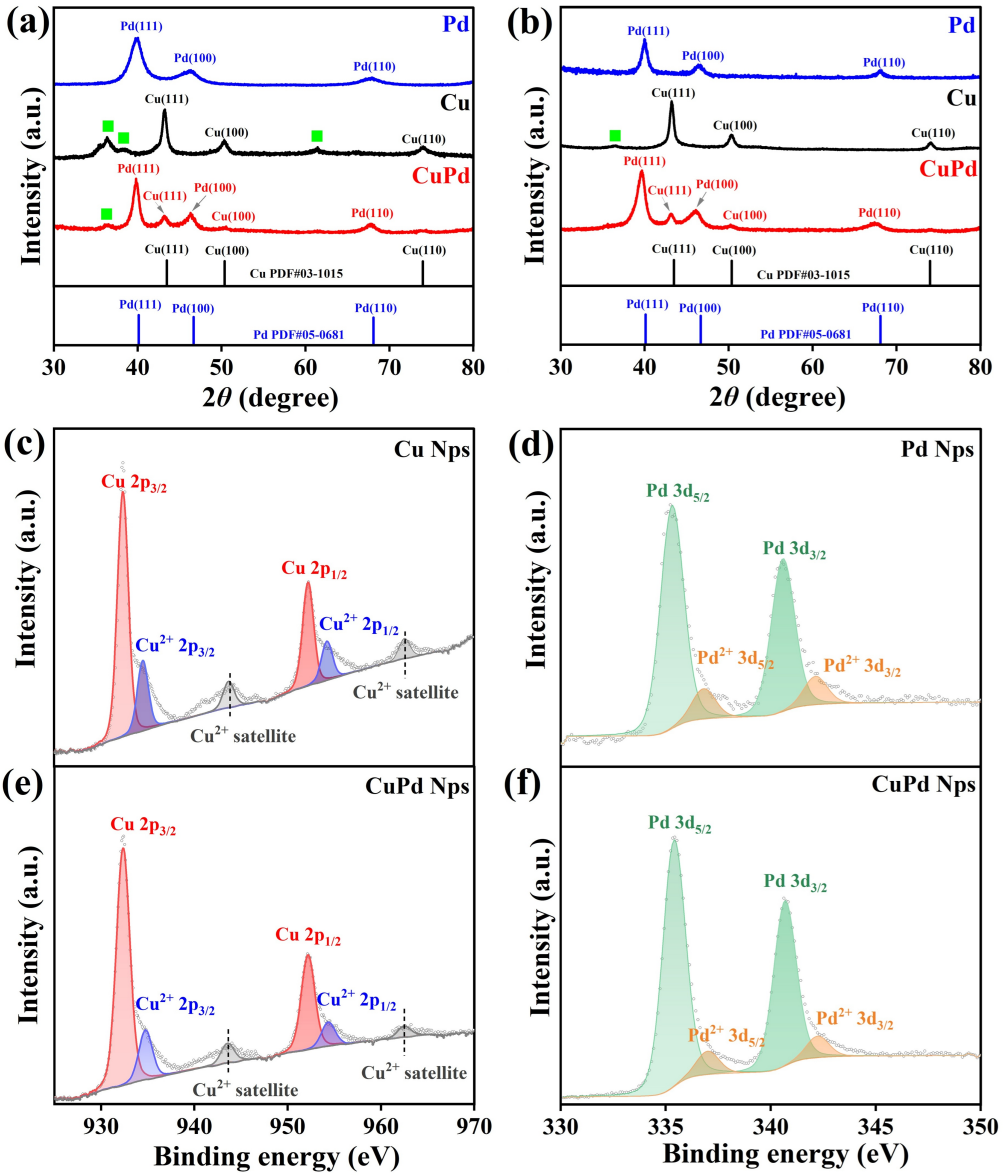

Figure 4.3: XRD patters and XPS spectra. X-ray diffraction (XRD) patterns of the prepared Cu, CuPd and Pd samples (a) before electrochemical reduction and (b) after reduction of -1.3 V_{RHE} for 1 hour. The green cubes represent oxidation states of Cu. (c-f) X-ray photoelectron spectroscopy (XPS) spectra of the Cu, CuPd and Pd samples. (c, e) High-resolution Cu 2p spectra of Cu and CuPd NPs, and (d, f) high-resolution Pd 3d spectra of Pd and CuPd NPs.

chemical reactions. The Cu 2p and Pd 3d XPS spectra of the CuPd sample and monometallic Cu, Pd NPs are shown in Figure 4.3c-4.3f. For CuPd and Cu NPs (Figure 4.3c and 4.3e), the Cu 2p region is deconvoluted into Cu^0 $2p_{3/2}$ and Cu^0 $2p_{1/2}$ components together with Cu^{2+} contributions and the characteristic shake-up satellites. For CuPd and Pd NPs (Figure 4.3d and 4.3f), the Pd^0 $3d_{5/2}$ and Pd^0 $3d_{3/2}$ doublet dominates with a minor Pd^{2+} component. Critically, the Cu 2p and Pd 3d peak positions in the CuPd sample coincide with those of the respective monometallic Cu and Pd NPs within the experimental resolution, suggesting no detectable binding-energy shift or emergence of new components. These results indicate that CuPd NPs do not alloy, instead, they coexist as separate phases. Moreover, the oxidized features (Cu^{2+} satellites and Pd^{2+} shoulders) can be disregarded, since XRD results indicate the disappearance of oxide phases after reduction.

The CO_2-temperature programmed desorption (CO_2-TPD) spectra of CuPd, Cu and Pd NPs are shown in Figure 4.4a. Cu NPs exhibit a temperature desorption feature in the temperature

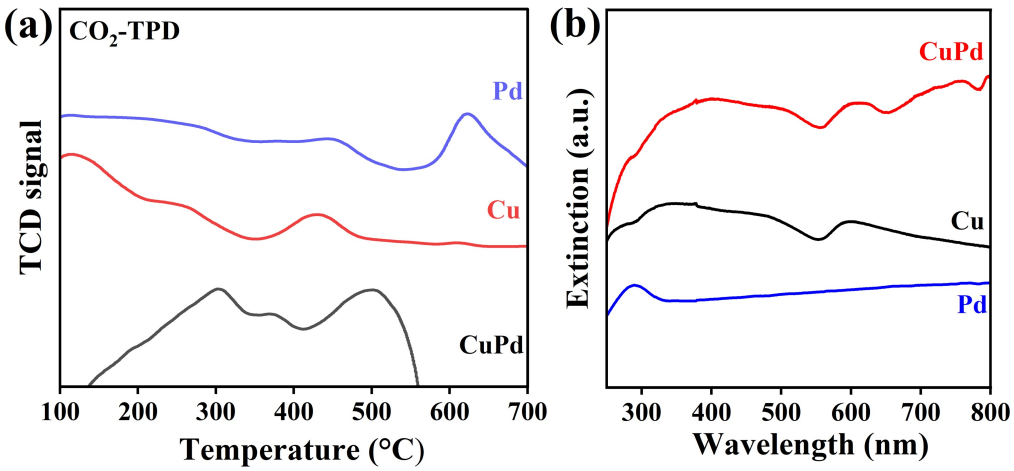

Figure 4.4: CO_2-TPD and UV-vis spectra. (a) The CO_2-temperature programmed desorption (CO_2-TPD) of Cu, CuPd and Pd NPs, showing the CO_2 desorption behaviors of three samples. (b) The UV-vis spectra of Cu, CuPd and Pd NPs, illustrating their optical properties.

range of ≈370–470 °C, which can be assigned to CO_2 released from Cu surface sites. Pd NPs show a desorption peak at a higher temperature range (≈580–680 °C), corresponding to CO_2 desorption from Pd sites. In comparison, CuPd NPs display three distinct desorption peaks. Combined with the HR-TEM observations and our previous studies[108], these three peaks can be assigned to CO_2 desorption from Cu sites, Pd sites and interfacial CuPd sites, respectively. Overall, the HR-TEM images, XRD patterns, XPS spectra, and CO_2-TPD results collectively indicate that the CuPd NPs possess multiple types of surface adsorption sites rather than forming a homogeneous alloy phase. The UV-vis extinction spectra recorded in transmission mode, as shown in Figure 4.4b. The Pd NPs exhibit mainly UV absorption with a response around 280 nm, whereas Cu NPs display a localized surface plasmon resonance (LSPR) band centered at approximately 600 nm. The CuPd NPs exhibit two distinct LSPR peaks at 280 and 605 nm, corresponding to the LSPRs of Pd NPs and Cu NPs, respectively. The spectrum of CuPd NPs combines the features of both Cu NPs and Pd NPs without discernible peak shifts, further supporting phase-separated Cu and Pd domains.

After comprehensive structural and spectroscopic analyses, the successful synthesis of phase-separated CuPd NPs featuring distinct Cu, Pd, and Cu–Pd interfacial sites was confirmed. The coexistence of individual Cu and Pd phases is expected to facilitate tandem catalytic processes. Moreover, the UV–vis spectra revealed a LSPR in the visible region centered at approximately 605 nm, which corresponds to the Cu components. This plasmonic feature suggests that the CuPd NPs are capable of harvesting visible light and converting it into energetic charge carriers and localized heat.

Plasmon-enhanced CO_2RR performance.

Given the unique electronic and structural features described above, the CuPd NPs are expected to exhibit enhanced electrocatalytic CO_2RR performance under light illumination. To probe this plasmonic effect, a 625 nm LED was employed in subsequent CO_2RR tests to resonantly excite the LSPR of Cu component, and the plasmon-enhanced activity and selectivity of CuPd catalysts were systematically investigated and compared with their monometallic counterparts.

The LSV curves (Figure 4.5a) and the corresponding Tafel plots (Figure 4.5b) clearly demonstrate that both CuPd and Cu NPs exhibit enhanced electrocatalytic activity under 625 nm LED illumination compared to dark conditions. Specifically, the photocurrent densities of CuPd and Cu NPs increase significantly (Figure 4.5c-4.5d), while the overpotential required

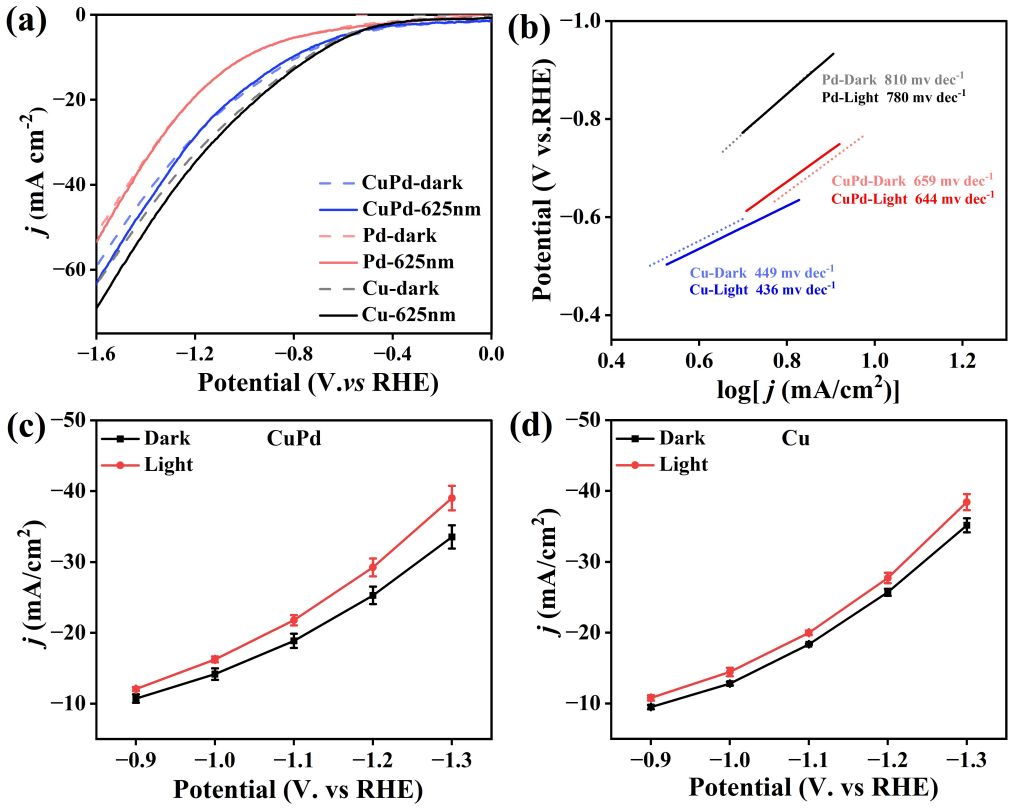

Figure 4.5: Electrochemical kinetics. (a) Linear sweep voltammograms (LSV) curves and (b) Tafel slope of CuPd, Cu, and Pd catalysts in dark and illumination conditions. (c, d) The total current densities of CuPd and Cu catalysts at the potential range from -0.9 to -1.3 V_{RHE} under dark and 625 nm LED illumination.

to achieve the same current density decreases, indicating accelerated reaction kinetics. The smaller Tafel slope under illumination further confirms that the charge transfer process becomes more favorable when CuPd and Cu NPs are exposed to visible light. This enhancement can be attributed to the LSPR effect of Cu and CuPd NPs, which promotes the adsorption and activation of CO_2 and intermediates on the catalysts surface. In contrast, the changes in Tafel slope of Pd NPs under illumination are negligible, indicating that their catalytic behavior is largely insensitive to visible light excitation. This is primarily due to low light absorption cross-section of Pd in the visible region and the lack of a significant plasmon resonance near 625 nm, resulting in minimal photoinduced carrier generation. Therefore, the light-enhanced reaction kinetics observed in CuPd and Cu catalysts mainly originate from the plasmonic properties of Cu, while the Pd component mainly provides active sites for CO_2RR without direct photon contribution.

Electrochemical CO_2RR experiments were performed sequentially under dark and illumination conditions to evaluate the effect of light on catalytic performance. To quantitatively assess the plasmon-induced contributions to CO_2RR on CuPd and Cu NPs, we calculated the enhancement in the production yield (ppm) of products between the illumination and dark conditions for each product using the following formula:

$$Enhancement(\%) = \frac{Light_{(\mathrm{ppm})} - Dark_{(\mathrm{ppm})}}{Dark_{(\mathrm{ppm})}}$$

where $Light_{(\mathrm{ppm})}$ and $Dark_{(\mathrm{ppm})}$ represent the concentration (in parts per million, ppm) of a specific CO_2RR product, such as CO, C_2H_4, or H_2, obtained under light illumination and dark conditions, respectively. This formula quantifies the relative increase in product formation

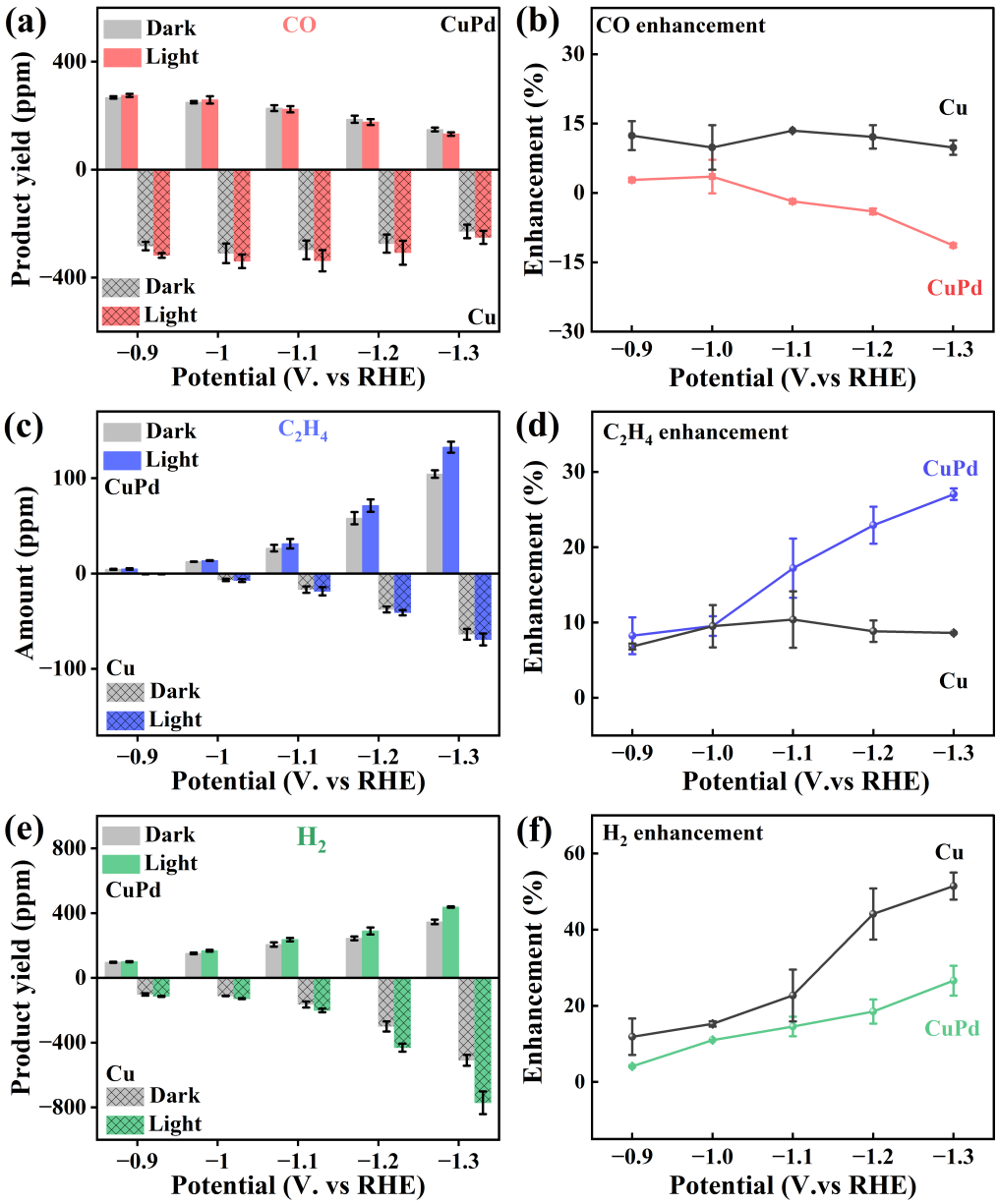

Figure 4.6: Yield (ppm) and enhancement of CO, C_2H_4, and H_2 for CuPd and Cu catalysts under dark and illumination. (a, c, e) Yields (ppm) of CO, C_2H_4, and H_2 on CuPd and Cu electrodes under dark and illumination at different potentials. (b, d, f) Corresponding enhancement percentages of CO, C_2H_4, and H_2 under light compared to dark at different potentials.

caused by 625 nm LED illumination, providing a standardized measure of light-induced enhancement that is independent of absolute productivity. Positive enhancement values indicate that illumination promotes the reaction, which can be attributed to photoinduced surface excitation on the Cu or CuPd catalyst. Conversely, negative enhancement values indicate that the catalytic process is not enhanced by 625 nm LED illumination, or is even inhibited. By applying this formula to the detected products, we systematically evaluated the changes in selectivity and efficiency caused by 625 nm LED illumination, thereby identifying which reaction pathways are promoted by plasmon excitation.

As a key intermediate in the formation of C_{2+} products, the *CO intermediate plays a crucial role in determining the selectivity of CO_2RR. The *CO intermediate can desorb from the catalyst surface as gaseous CO or undergo C-C coupling to form C_{2+} products such as C_2H_4 and C_2H_5OH.[133,134] The balance between these two pathways is highly sensitive to

surface composition, local electronic structure, and LSPR effects on the catalyst. As shown in Figure 4.6a-4.6d, under 625 nm LED illumination at −1.3 V_{RHE}, CO production on the Cu catalyst increased by approximately 9.8%, while C_2H_4 production increased by 8.6%. The simultaneous enhancement of CO and C_2H_4 indicates that plasmon excitation on Cu NPs promotes CO_2 activation and the formation of the *CO intermediate. Subsequently, a portion of the photoexcited *CO desorbs as CO gas, while another portion undergoes C-C coupling step, leading to enhanced C_2H_4 production. Therefore, the photoinduced increase in CO and C_2H_4 yields on the Cu NP surface indicates that plasmonic Cu sites actively participate in *CO generation and subsequent C-C bond formation.

In contrast, on CuPd catalyst at −1.3 V_{RHE}, the 625 nm LED illumination resulted in an 11.4% decrease in CO production, while simultaneously increasing C_2H_4 production by a significant 27.0%. Compared on photoexcited products on Cu NPs, this opposing trend on CuPd NPs suggests that plasmon excitation first promotes CO_2 activation and the formation of the *CO intermediate. Subsequently, plasmon excitation selectively drives *CO coupling step rather than desorption from the CuPd NPs surface. Consequently, the CuPd NPs surface exhibits higher selectivity for C_{2+} products compared to pure Cu NPs. Overall, these results suggest that illumination can enhance CO_2 activation and the formation of the *CO intermediate, but the subsequent pathway depends on the catalyst composition. For Cu NPs, plasmon excitation promotes both *CO desorption and coupling. For CuPd NPs, plasmon excitation selectively promotes *CO coupling to form C_{2+} products.

As shown in Figure 4.6e-4.6f, we also monitored the hydrogen evolution reaction (HER), the primary competing pathway in CO_2RR. H_2 production was quantified under both dark and illuminated conditions to assess the effect of light on the selectivity between CO_2 and HER. Under a 625nm LED, the yield of H_2 increased by 51.4% for Cu NPs and 26.6% for CuPd NPs at -1.3 V_{RHE} compared to dark conditions. This significant enhancement indicates that light irradiation accelerates the proton reduction process for both catalysts, while the enhancement varies depending on the surface composition. The large enhancement of H_2 on the Cu surface implies that photoexcited carriers are primarily consumed by HER. In contrast, the smaller increase in H_2 production observed on CuPd NPs suggests that the introduction of Pd alters the charge distribution and surface energetics, thereby suppressing excessive proton reduction. Therefore, although both catalysts exhibited photoenhanced H_2 formation, the CuPd catalyst showed more controlled electron utilization for CO_2RR, which is consistent with the observed higher C_2H_4 selectivity. Overall, the synergistic electronic interaction of Cu-Pd effectively regulated competition between CO_2RR and HER, maintaining efficient CO_2 conversion while minimizing unwanted H_2 evolution.

As shown in Figure 4.7a-4.7b, the yields of HCOOH and C_2H_5OH on CuPd NPs were compared under illumination and dark conditions. Upon illumination, HCOOH yield increased slightly, while C_2H_5OH yield decreased slightly. For the Pd catalyst (Figure 4.7c-4.7d), the increase in CO yield under illumination was negligible, while the yield of H_2 was slightly enhanced. Figures 4.8a-4.8c show the Faradaic efficiencies (FE) of different CO_2RR products for CuPd, Cu and Pd catalysts. No significant changes in FE were observed under illumination, which can be attributed to the simultaneous increase in product yield and total current density. Furthermore, stability tests (Figure 4.8d) demonstrated that the CuPd catalyst maintained relatively stable current densities during prolonged electrolysis. The EDS mapping images after reaction (Figure 4.8e) revealed no significant elemental segregation or morphological degradation, further verifying the structural stability of the CuPd catalyst during plasmon-enhanced CO_2RR.

Plasmon-induced hot electrons and heating.

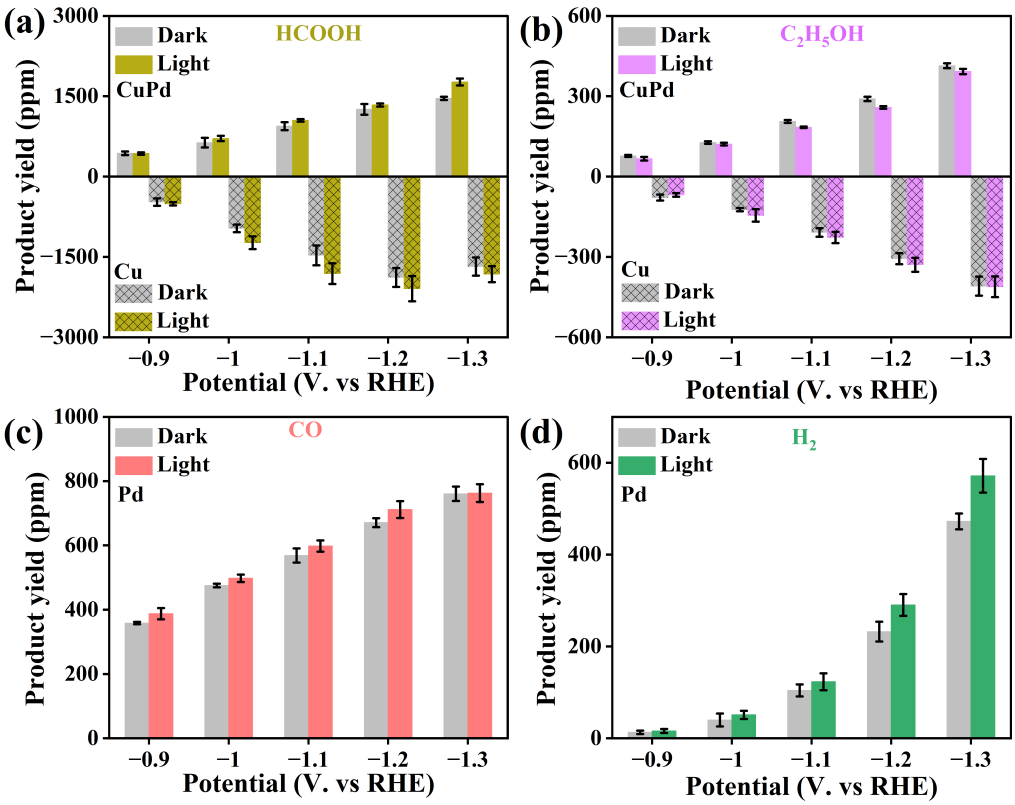

Figure 4.7: Yield (ppm) of products for CuPd and Pd catalysts under dark and illumination. (a, b) Yields (ppm) of HCOOH and C_2H_5OH on CuPd and Cu electrodes under dark and illumination conditions at different potentials. (c, d) Yields (ppm) of CO and H_2 on Pd electrodes under dark and illumination conditions at different potentials.

As mentioned in the Introduction, plasmonic excitation generates hot carriers and heats the metal lattice of the nanostructure. The photocurrent response experiments have been reported to quantify the contributions of hot electrons and the photothermal effect.[154] As shown schematically in Figure 4.9a, the photocurrent response exhibits a two-stage increase: a rapid increase in the initial 0.05 s due to hot electrons, followed by a slower increase from 0.05 s to 10 s due to photothermal effect. Therefore, the contributions of plasmon-induced hot electrons $C_{\text{hot electrons}}$ and photothermal effect $C_{\text{photothermal}}$ can be quantified using the following equations:

$$C_{hot\ electrons} = \frac{I_{0.05}}{I_{10}}$$

$$C_{photothermal} = \frac{I_{0.05-10}}{I_{10}}$$

Here, $I_{0.05}$ denotes the photocurrent measured at the initial 0.05 s after illumination, primarily arising from the injection of hot electrons. $I_{0.05-10}$ represents the photocurrent increase from 0.05 s to 10 s, which reflects the photothermal contribution associated with heat accumulation. I_{10} corresponds to the total photocurrent with 10 s of illumination. This method allows a clear separation of the ultrafast electronic process from the slower thermal process, enabling a more precise understanding of contributions from hot electrons and photothermal effect.

The photocurrent response experiment was carried out on CuPd and Cu NPs under chopped light every 10 s at -1.3 V_{RHE} in Ar- and CO_2-saturated electrolyte (Figure 4.9b-4.9c). In Ar-saturated electrolyte at -1.3 V_{RHE} where only HER occurs, the photothermal effect accounts for 80% of the total photocurrent on CuPd NPs and 76% on Cu Nps (Figure 4.9d), suggesting that the photothermal effect mainly drives proton reduction and H_2 generation

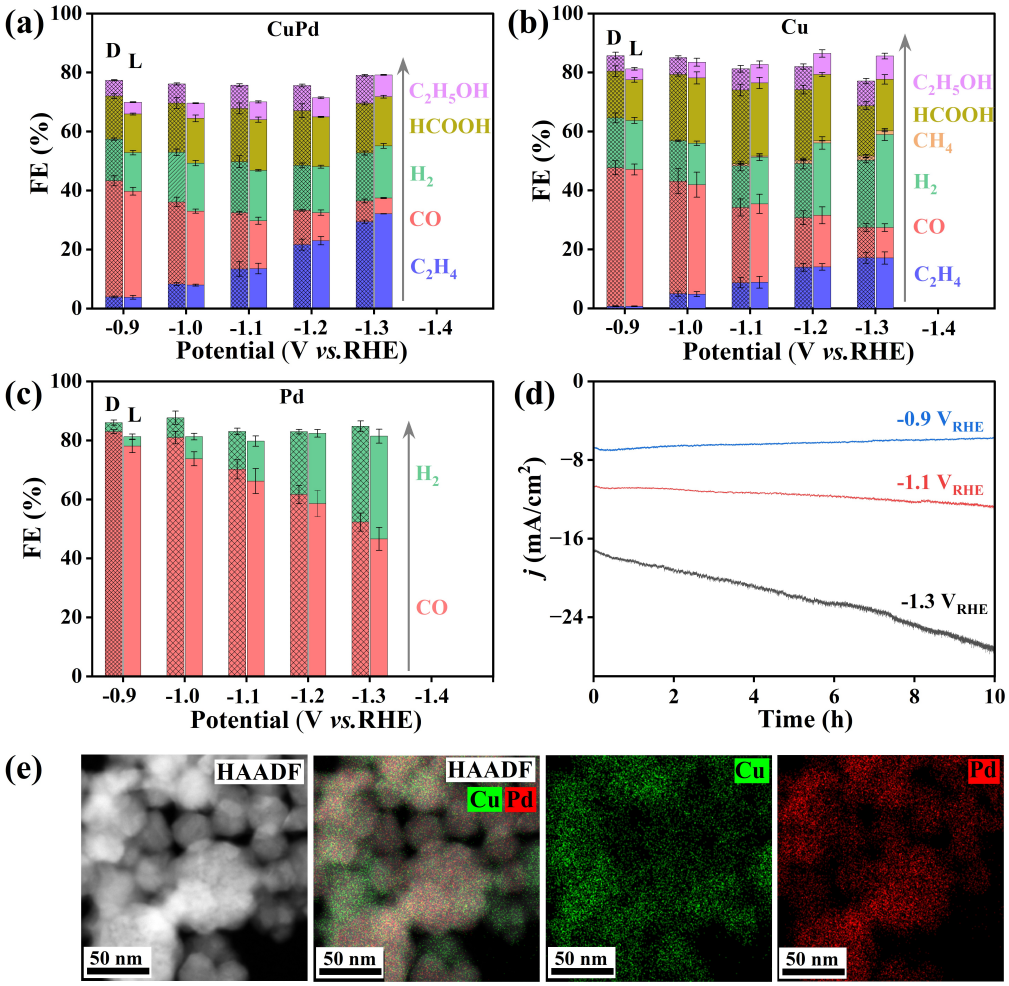

Figure 4.8: (a, b, c) Faradaic efficiencies (FE) of different products on CuPd, Cu, and Pd electrodes under dark (D) and light (L) conditions at different potentials. (d) Chronoamperometric stability tests of the CuPd electrode in 10 hours at different potentials. (e) HAADF and elemental mapping images of the CuPd catalyst after -1.3 V_{RHE} for 1 hour.

under light illumination. In CO_2-saturated electrolyte at -1.3 V_{RHE} where both CO_2RR and HER occur (CO_2RR dominates), the contribution of hot electrons to the photocurrent increased significantly to 42% on CuPd NPs and only 28% on Cu NPs, suggesting that both hot electrons and photothermal effect contribute to the enhancement of CO_2RR on CuPd NPs. In contrast, for CO_2RR on Cu Nps, the photothermal effect plays a dominant role compared to hot electrons, implying that temperature-induced kinetic enhancement outweighs direct electron excitation effects. This is also supported by the greater increase in H_2 production on Cu NPs compared to CuPd NPs under illumination (Figure 4.6e-4.6f). These results collectively demonstrate that while both photothermal heating and hot electrons promote catalytic reactions, their relative importance depends largely on catalyst composition: Cu NPs primarily exhibit thermally enhanced HER and CO_2RR activity, while CuPd NPs benefit from CO_2 activation and C-C coupling assisted by both hot electron and photothermal effects.

Plasmon-induced hot electrons are closely associated with local electric field enhancement on the surface of plasmonic nanomaterials, where a stronger near-field favors the generation of hot electrons.[134,155] Therefore, COMSOL simulations were first used to obtain the electric field distributions on CuPd, Cu, and Pd NPs under 625 nm illumination (Figure 4.10a- 4.10c). The spatial distribution of the electric field intensity differed significantly between the three systems. For CuPd NPs (Figure 4.10a), a distinct “hot spot” appeared at the CuPd interface region, indicating enhanced charge oscillations and electromagnetic confinement. In contrast,

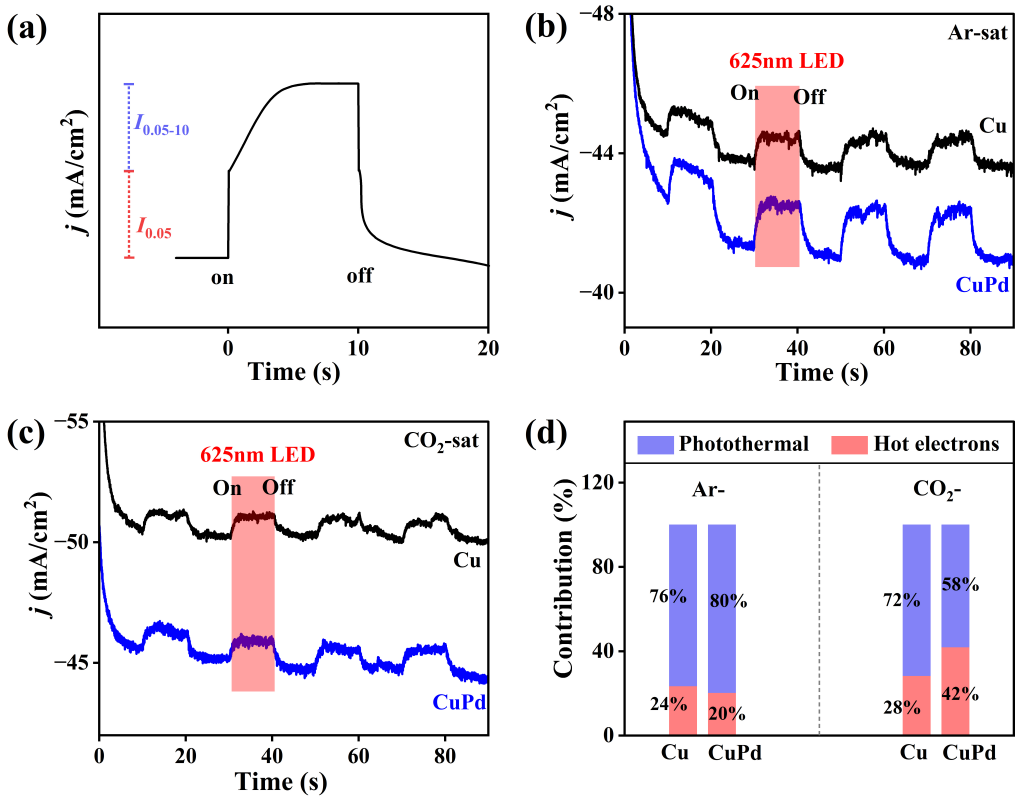

Figure 4.9: Photocurrent response. (a) Schematic of evaluating the contributions of hot electrons and photothermal effects based on the photocurrent response. Photocurrent responses of (b) Ar-saturated and (c) CO_2-saturated 0.1 M $KHCO_3$ upon 625 nm light chopped in every 10 seconds on CuPd NPs and Cu NPs electrode at -1.3 V_{RHE}. (d) The contributions of hot electrons and photothermal effects in Ar-saturated and CO_2-saturated 0.1 M $KHCO_3$ upon 625 nm light chopped in every 10 s on the CuPd and Cu NP electrode at -1.3 V_{RHE}.

pure Cu NPs (Figure 4.10b) displayed a weaker but still significant field enhancement near the surface. Meanwhile, Pd NPs (Figure 4.10c) exhibited minimal field enhancement. Simulation results indicate that the CuPd interface exhibits the strongest local electric field enhancement. The significantly stronger local field intensity observed in CuPd NPs suggest that the formation of a bimetallic interface effectively amplifies the plasmon resonance.

Consistent with the electric field distribution, the plasmon-induced hot electrons are also mainly localized at the CuPd interface, as shown in COMSOL simulations (Figure 4.10d-4.10f). This electron localization originates from the strong plasmon coupling between Cu and Pd, which concentrates electromagnetic energy at the interface and promotes the efficient excitation of hot carriers. On Cu NPs, the induced hot electrons distribution is more uniform and the density is relatively low, indicating low field confinement efficiency. For Pd NPs, the electron density is minimal and widely dispersed, indicating rapid energy dissipation and weak carrier excitation. These results collectively indicate that the CuPd interface provides enhanced field strength and stronger charge localization, favoring the generation and utilization of plasmon-induced hot electrons. This is also reasonable from the perspective of the work function of the two metals (Figure 4.10g-4.10j): the larger work function of Pd compared to Cu drives the diffusion of plasmon-excited hot electrons from Cu side to the CuPd interface.[156] The difference in work function between Cu and Pd improves hot carrier separation and suppresses recombination. Notably, hot electrons were reported to dominate the reduction of CO_2 to CO, significantly increasing CO generation.[91,154] Taken together with the experimental results in Figure 4.6, these results suggest that hot electrons localized at the CuPd interface enhance *CO generation over H_2 generation.

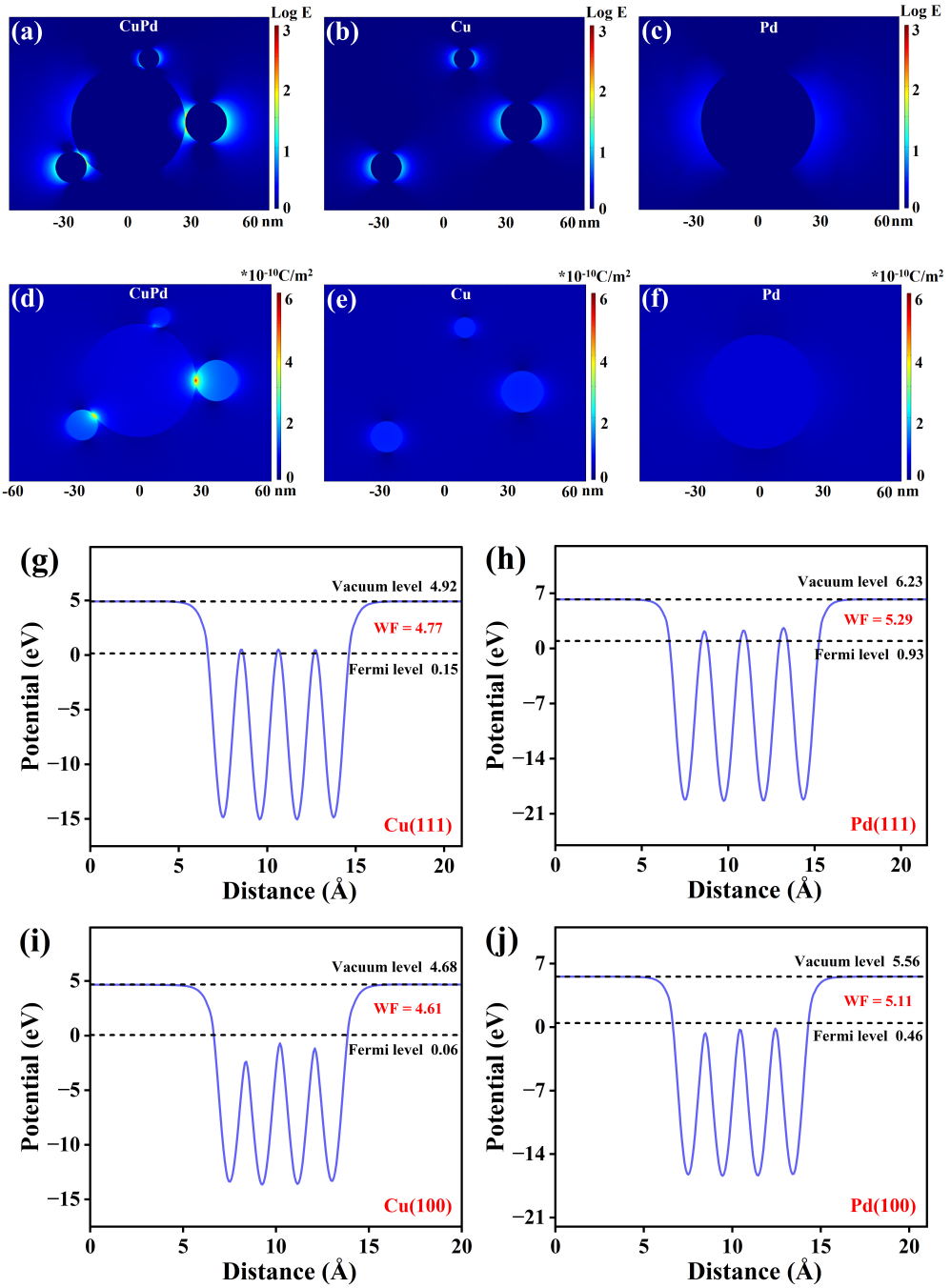

Figure 4.10: COMSOL simulations and work function. The electric field distribution of (a) CuPd NPs, (b) Cu NPs and (c) Pd NPs excited by 625 nm light. The electron density distribution of (d) CuPd NPs, (e) Cu NPs and (f) Pd NPs excited by 625 nm LED. (g-j) Planar averaged electrostatic potentials along the z-direction for Cu and Pd.

Following the generation of hot electrons at CuPd interface, these high-energy carriers dissipate their energy through scattering processes in approximately 1 $\tilde{1}0$ ps, resulting in localized heating and rapid diffusion across the entire metal surface.[157] Photocurrent measurements confirm that photothermal effect enhances both H_2 evolution and CO_2RR. Plasmon-induced heating has been reported to facilitate CO_2 activation and *CO generation.[150,151,154] External heating from 16 °C to 36 °C (Figure 4.11), closely matching the temperature rise reported for bimetallic plasmonic systems under illumination,[158] led to increased H2 and CO production but reduced C_2H_4 formation at -1.3 V_{RHE} for CuPd NPs. This is likely due to reduced CO solubility at higher temperature of electrolyte,[159] which promotes CO release and hinders C-C coupling. In contrast, the unique advantage of plasmonic heating is its confinement

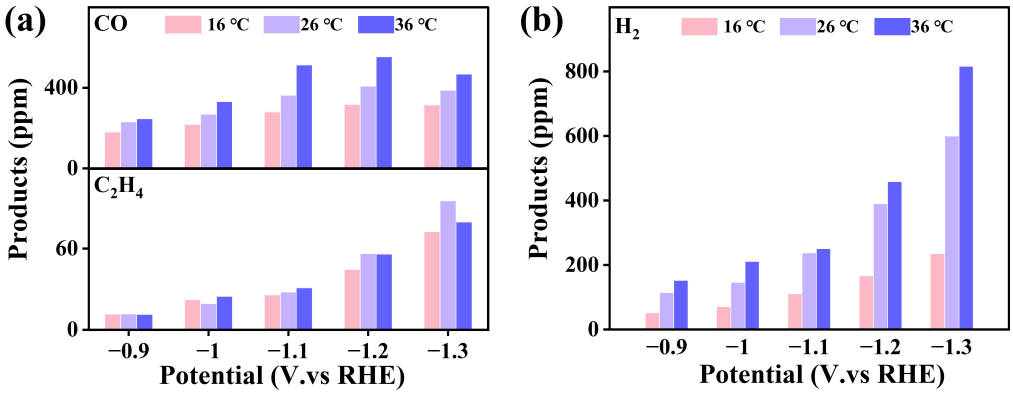

Figure 4.11: Yeild (ppm) of products for CuPd catalysts under temperature gradient. Yields (ppm) of (a)CO, C_2H_4 and (b) H_2 on CuPd electrodes under different temperature of 16 ℃, 26 ℃, and 36 ℃.

to the catalyst surface without affecting the bulk electrolyte temperature. The increased surface temperature enhances *CO formation on the whole surface of CuPd NPs (including CuPd interface, Cu sites and Pd sites), thereby offering greater potential for subsequent C-C coupling steps.

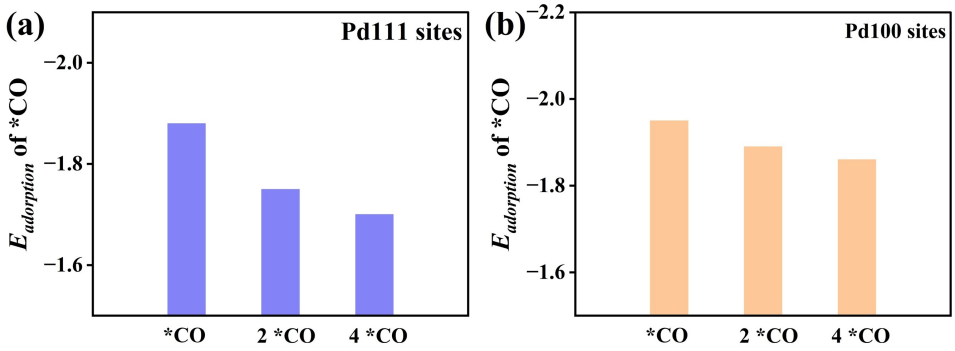

Figure 4.12: *CO adsorption on Pd sites with different coverage. The *CO adsorption energy on (a) Pd(111) sites and (b) Pd(100) sites with different *CO coverage by DFT calculations.

The results above demonstrate that the role of plasmon excitation for CO_2RR is twofold: hot electrons facilitate *CO formation on CuPd interfacial sites and photothermal effect promotes *CO formation on the whole surface of CuPd NPs. Subsequently, DFT calculations were employed to further reveal the mechanism of the increase in C_2H_4 on the CuPd NPs surface under illumination. As shown in Figure 4.12, the adsorption energy of *CO becomes less negative on the Pd (111) and Pd (100) surfaces with increasing *CO coverage, indicating enhanced repulsive interactions between the *CO. In addition, the CuPd (111) and CuPd (100) surfaces (Figure 4.13) also exhibit moderately weakened *CO adsorption with increasing *CO coverage. Therefore, the increase in *CO coverage on the Pd surface and the CuPd interface greatly favors the migration of *CO to the adjacent Cu surface, which leads to the accumulation of *CO on the Cu surface.[160]

In addition, the Gibbs free energy of C-C coupling on the Cu (111) and Cu (100) surfaces derived from DFT calculations (Figure 4.14) indicate that higher *CO coverage can significantly reduce the reaction barrier, from approximately 2.0 eV at low *CO coverage to below 1.0 eV at high *CO coverage. This coverage dependence suggests that increased *CO generated by hot electrons at the CuPd interface and thermal effects across the catalyst surface effectively promotes the C-C coupling step. Overall, DFT calculations indicate that increased *CO coverage at the CuPd interface and Pd sites weakens *CO adsorption, thereby promoting

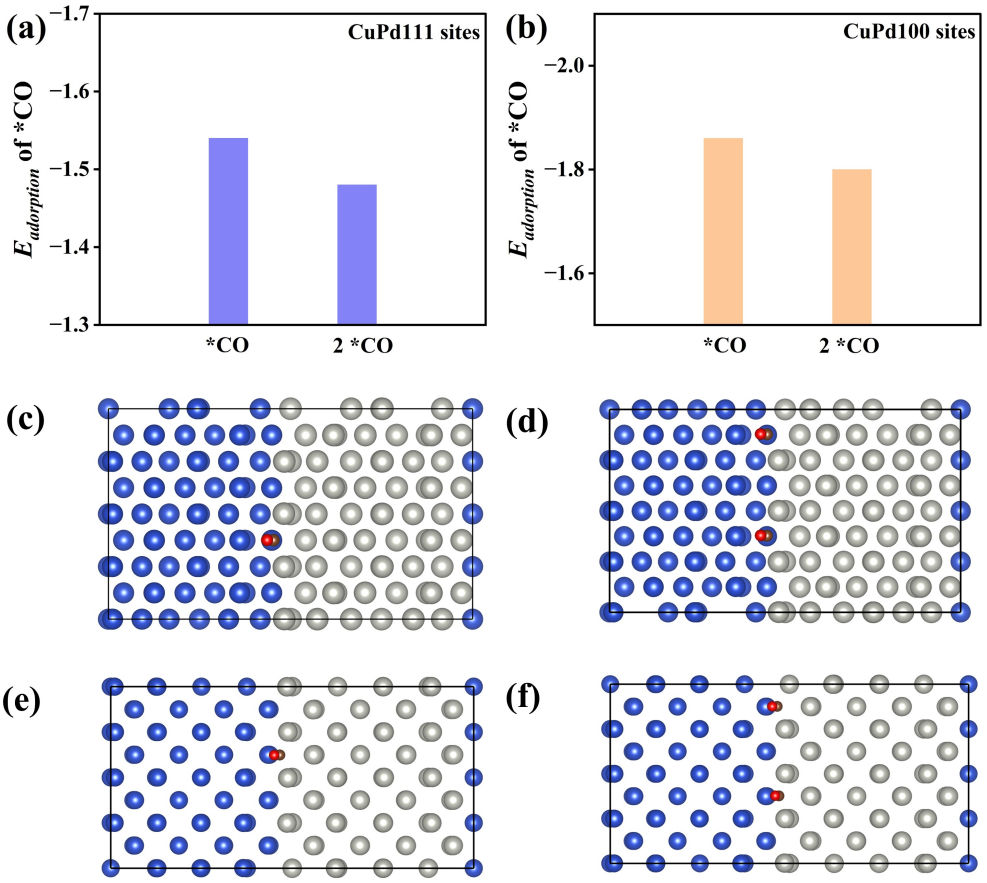

Figure 4.13: *CO adsorption on CuPd interfaces with different coverage. The *CO adsorption energy on (a) CuPd(111) and (b) CuPd(100) interfaces with different *CO coverage by DFT calculations. The configurations of *CO and 2 *CO adsorbed on (c, d) CuPd(111) and (e, f) CuPd((100) interfaces, respectively. The blue, grey, brown and red atoms represent Cu, Pd, C and O, respectively.

its diffusion to Cu sites. *CO accumulation on Cu sites lowers the energy barrier for C-C coupling, ultimately leading to a significant increase in the generation of C_2H_4 on CuPd NPs.

ATR-FTIR measurements.

The in-situ ATR-FTIR measurements, which can track the surface dynamics of reaction intermediate, were carried out to track *COOH and *CO intermediates on CuPd, Cu and Pd NPs under dark and illumination conditions. The vibrational bands in the range 1285 $\sim$ 1250 cm^{-1} are attributed to the functional groups of *COOH on CuPd, Cu and Pd NPs (Figure 4.15).[161–163] As shown in Figure 4.15a-4.15b, for the Cu and Pd catalysts, the *COOH vibrational bands located in 1285 $\sim$ 1250 cm^{-1} range gradually increase in intensity upon 625 nm illumination, but the enhancement is relatively small. The Cu NPs exhibit a slightly stronger photoresponse than the Pd NPs, but the changes in both are limited compared to the bimetallic CuPd system, indicating a weaker photoinduced activation of the individual metals.

In contrast, the CuPd catalyst exhibits a significant enhancement of the *COOH band intensity upon illumination, as shown in Figure 4.15c-4.15d. The *COOH peak intensity increases sharply within the first few minutes after illumination, indicating a faster accumulation of *COOH species on CuPd surface. Quantitative analysis of the integrated peak areas (Figure 4.15e) further confirms that the rate of *COOH generation on CuPd NPs is much faster under illumination than in the dark. The difference in integrated intensity between illumination and darkness reflects the accelerated *COOH generation kinetics under plasmon

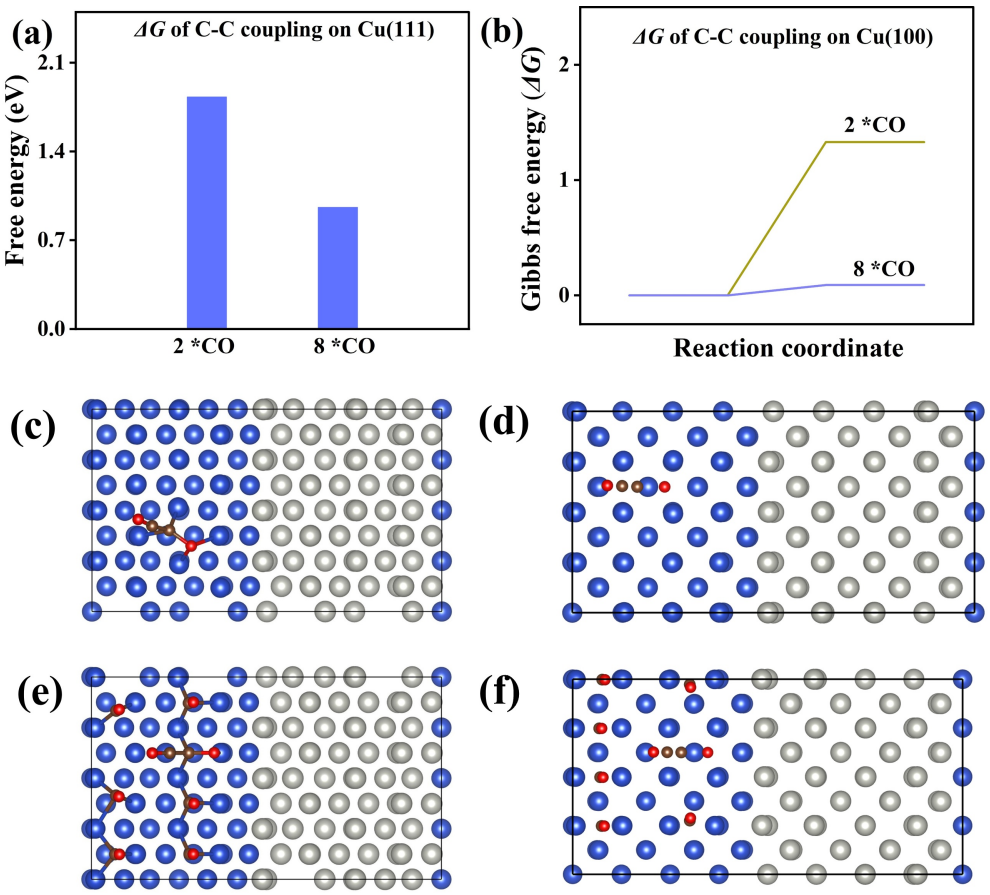

Figure 4.14: C-C coupling on Cu sites with different *CO coverage. The thermodynamic energy barrier of C-C coupling on Cu sites of (a) CuPd(111) and (b) CuPd(100) surfaces with different CO* coverage. (c, d) The configurations of C-C coupling on Cu site of CuPd(111) surface with different *CO coverage for DFT calculations. (e, f) The configurations of C-C coupling on Cu(100) sites with different *CO coverage for DFT calculations. The blue, grey, brown and red atoms represent Cu, Pd, C and O, respectively.

excitation. Overall, these results demonstrate that under 625 nm excitation, the formation and accumulation of *COOH intermediates on CuPd NPs surface is significantly enhanced compared to that on monometallic Cu or Pd surface. This enhancement stems from the synergistic effect of hot carrier injection at the CuPd interface and photothermal heating across the whole CuPd NPs surface, which together accelerate the CO_2 activation to *COOH. Furthermore, the plasmon-induced *COOH formation promotes the supply of more *CO intermediates, facilitating subsequent *CO diffusion and C-C coupling on the Cu site, thereby improving the selectivity for C_2H_4.

Next, we analyzed the *CO vibration bands (2100 $\sim$ 2000 cm^{-1}) on the CuPd, Cu and Pd catalyst under dark and illumination conditions, as shown in Figure 4.16. In dark and illumination conditions, the *CO stretching bands on Cu and Pd NPs appears near 2071 cm^{-1} and 2094 cm^{-1}, respectively (Figure 4.16a-4.16b), in line with previous reports.[164–168] These *CO stretching bands correspond to the linear adsorption of *CO on top of the Cu and Pd sites. On CuPd NPs in dark conditions, as shown in Figure 4.16c, the *CO stretching band appears near 2024 cm^{-1}, which deviates from the *CO stretching band on both Cu (2071 cm^{-1}) and Pd NPs (2094 cm^{-1}). The band near 2024 cm^{-1} could be attributed to the *CO being adsorbed on CuPd interface sites, similar to previous reports.[169] This red shift may be due to the hybridization between Cu 3d and Pd 4d orbitals, with charge redistribution weakening the C–O bond.

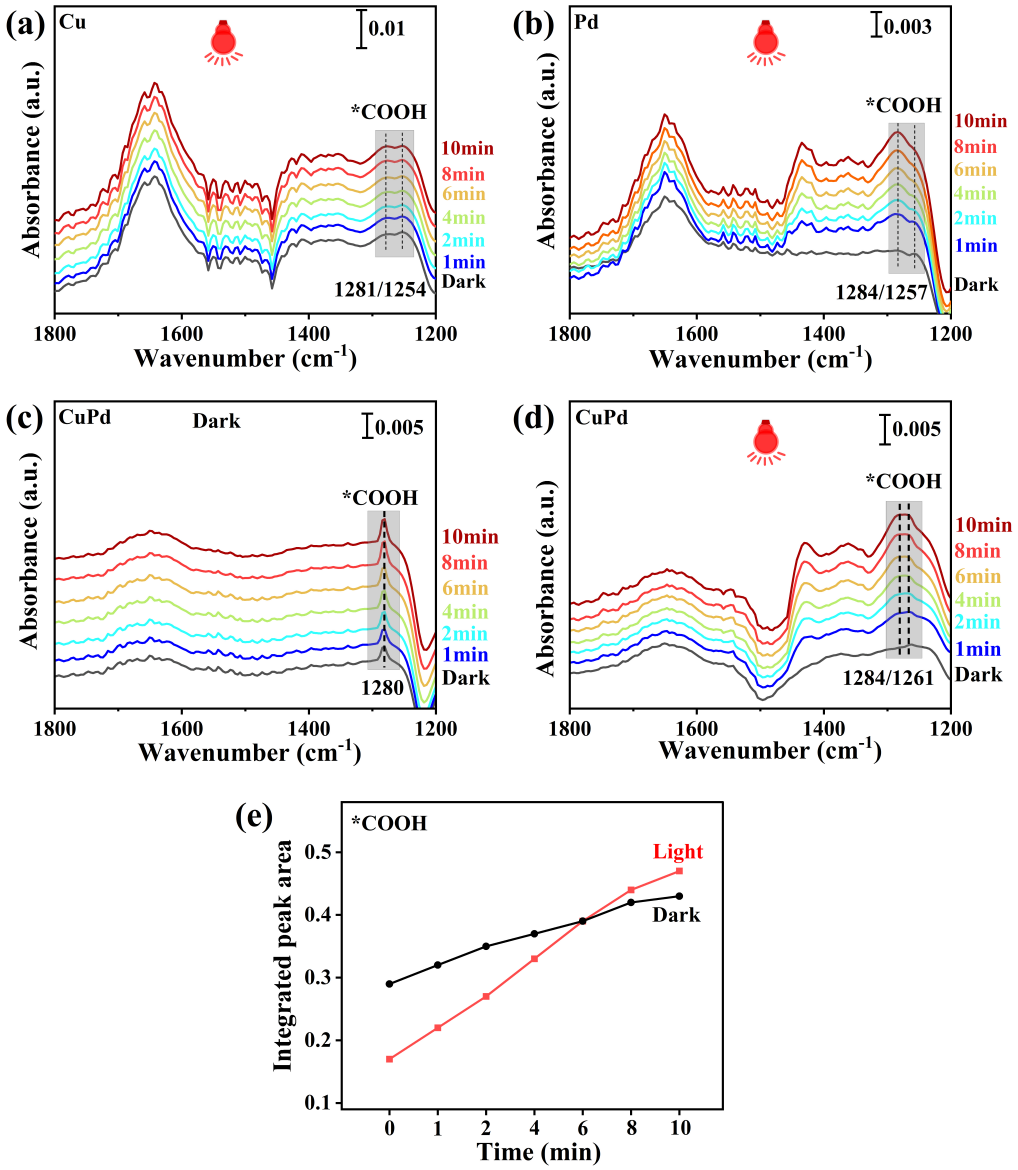

Figure 4.15: *COOH band of FTIR spectra. The in-situ FTIR spectra on (a) Cu NPs under 625 nm light irradiation for 10 minutes and (b) Pd NPs NPs under 625 nm light irradiation for 10 minutes, (c) CuPd NPs under dark and (d) CuPd NPs electrodes under 625 nm light irradiation for 10 minutes, which were continuously collected in CO_2RR-saturated 0.1 M $KHCO_3$ electrolyte at -1.3 V_{RHE} with a scan rate of 5 mV/s. (e) The integration of FTIR spectra of *COOH on CuPd NPs electrodes in CO_2-saturated 0.1 M $KHCO_3$ electrolyte at -1.3 V_{RHE} in 10 minutes under dark and 625 nm light irradiation, respectively.

Within around 2 minutes of light illumination, as shown in Figure 4.16d, the vibrational bands at 2017 cm^{-1}, attributed to *CO adsorbed on CuPd interfacial sites, gradually decreased, while a new band emerged at 2075 cm^{-1}. This band closely matches the linear *CO stretching band on the Cu surface, indicating the diffusion of *CO from the CuPd interface sites to the Cu surface.[170] Furthermore, the persistence of the 2075 cm^{-1} band during illumination indicates that the *CO formed under plasmon excitation is more stably bound to Cu sites, preventing desorption to CO gas. These spectroscopic observations, together with the electrochemical performance showing that CuPd NPs exhibit reduced gas CO generation but enhanced C_2H_4 formation under illumination, suggest that plasmon excitation promotes the CO_2 activation, *CO generation and diffusion from CuPd interface to Cu sites rather than desorption.

Mechanism of plasmon-enhanced CO_2RR. Considering all the experimental and theoretical results, we can paint the complete image of CO_2RR on CuPd NPs in dark condition,

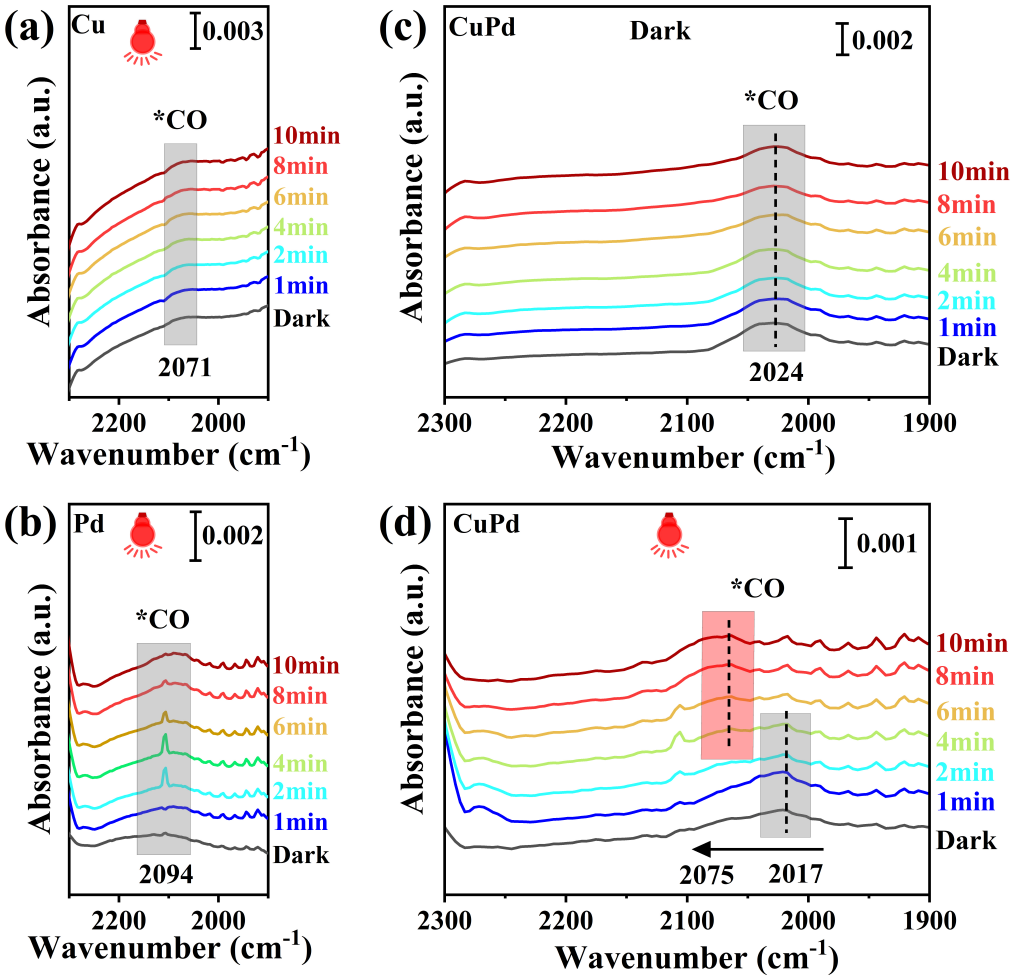

Figure 4.16: *CO band of FTIR spectra. The in-situ FTIR spectra on (a) Cu NPs under 625 nm light irradiation for 10 minutes and (b) Pd NPs NPs under 625 nm light irradiation for 10 minutes, (c) CuPd NPs under dark and (d) CuPd NPs under 625 nm light irradiation for 10 minutes, which were continuously collected in CO_2RR-saturated 0.1 M $KHCO_3$ electrolyte at -1.3 V_{RHE} with a scan rate of 5 mV/s.

external heating and light excitation, as shown in Figure 4.17. In dark, CO_2 is converted to *CO at the Pd and CuPd interface sites, and the generated *CO diffuses to the Cu sites where it undergoes C-C coupling to form C_2H_4. Under external heating, the CO solubility decreases with the increase in the electrolyte temperature, thereby yielding more CO gas but less C_2H_4. Under light excitation of CuPd NPs, the plasmon-generated hot electrons, which are mainly localized at the CuPd interface, accelerate the formation of *CO. Meanwhile, plasmon-induced heating accelerates CO_2RR and facilitates *CO formation on the whole CuPd NPs surface. Subsequently, the increased *CO generated on Pd and CuPd interfacial sites diffuses to Cu sites. The increased *CO coverage on Cu sites lowers the energy barrier of C-C coupling, ultimately promoting C_2H_4 generation. Simultaneously, the plasmon-induced heating also enhances H_2 production.

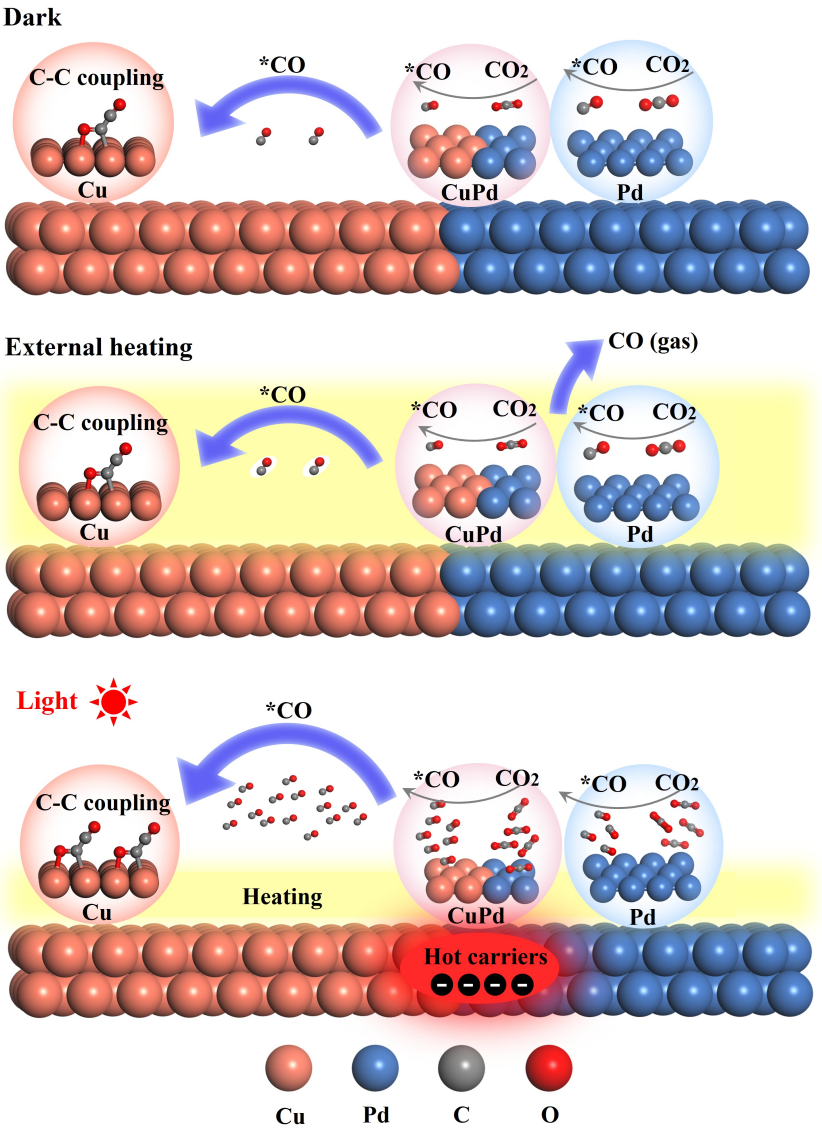

Figure 4.17: Schematic diagram. Schematic diagram of CO_2RR on the CuPd catalyst under dark, with external heating, and with illumination.

4.3 Summary

In summary, we synthesized CuPd NPs with distinct Cu, Pd, and CuPd interfacial sites and demonstrated that the synergy among the CuPd interface, plasmon-generated hot carriers and photothermal effects play a vital role in enhancing C_2H_4 generation under illumination. On CuPd NPs electrode under 625 nm LED excitation at -1.3 V_{RHE}, plasmon excitation led to a 11.4% decrease in CO generation concomitant to a 27.0% enhancement in C_2H_4 production, accompanied by a 26.6% increase in H_2 generation, com-pared to dark conditions. In contrast, Cu NPs under illumination exhibited significant enhancement in H_2 (51.4%) and CO production (9.8%), but only 8.6% enhancement in C_2H_4 production. Photocurrent response and COMSOL simulations confirmed that *CO formation on CuPd inter-face is greatly enhanced by plasmon-induced hot electrons and photothermal effect. Subsequently, DFT calculation reveal the increased *CO on CuPd interface weakens the adsorption of *CO, which promotes *CO diffusion to Cu sites. The significantly increased *CO on Cu sites further decreases the energy barrier of C-C coupling, ultimately promoting C_2H_4 generation. The *CO increase and diffusion are supported by in-situ FTIR spectroscopy. In addition, photothermal effect is considered as the primary contributor to the increased H_2 production

under illumination, as revealed by photocurrent response. These findings high-light the ability of plasmon-generated hot carriers and photothermal heating to tune the catalytic selectivity of CO_2RR. We also underscore the importance of catalyst design on leveraging plasmon excitation to control reaction pathways. This study offers new opportunities for the design of efficient, selective, and scalable systems for CO_2RR.

4.4 Method

Characterizations.

XRD data was collected by using an X'Pert PRO PANalytical instrument (Ni-filtered Cu Kα radiation source) from 30° to 80° with a slow scanning step 0.125° per min. X-ray photoelectron spectroscopy (XPS) was measured by Thermo Scientific Nexsa G2 surface analysis. The transmission electron microscopy (TEM) images were achieved on Tecnai G2 F20. The UV-vis-NIR absorption spectra were measured on UV/VIS/NR spectrometer Lambda 750 (PerkinElmer). CO_2 temperature-programmed desorption (TPD) measurements were conducted using a Xianquan TP-5080 apparatus.

Electrochemical measurements.

1. Preparation of work electrodes.

The inks for (plasmon-assisted) electrochemical activity measurement such as LSV curves and photocurrent response were prepared by mixing 1 mg catalyst in 600μL H2O and 400μL 2-propanol with 20 μL nafion. Then 30 minutes of ultrasound made the ink homogenous. 20μL ink was dropped onto carbon paper with an area of π × (0.25)2 cm2. The inks for (plasmon-assisted) CO2RR measurement were prepared by mixing 5 mg catalyst and 2mg carbon powder in 800μL 2-propanol with 20 μL nafion. Then 30 minutes of ultrasound made the ink homogenous. 400μL ink was sprayed onto 10 pieces of carbon paper (5mm × 5mm for every piece of carbon paper) by the airbrush.

2. CO_2RR (plasmon-assisted) electrocatalysis measurement.

The CO_2RR measurements were carried out in a quartz H-type cell as shown in Figure 4.18, with a potentiostat (Biologic, SP-300). For plasmon-assisted electrocatalysis measurement, the 625 nm LED (Mightex Systems) was first focused by a lens, then put front of the reactor with a distance of 10 cm. The power on the front side of the reactor was measured as 509 mW/cm2 by the power meter. The carbon paper loaded with catalysts was applied as the working electrode. A platinum plate and Ag/AgCl electrode were used as counter electrode and reference electrode, respectively. All the applied potentials (vs. Ag/AgCl) were converted to potentials (vs. RHE) by formula of $E_{RHE} = E_{Ag/AgCl} + 0.197\ V + 0.0592 * pH$. Before running the measurement, the electrolyte 0.1 M $KHCO_3$ was saturated with CO_2 by bubbling CO_2 gas (99.999%) for 20 minutes. The constant purged CO_2 was controlled with a rate of 30 sccm.

3. Detailed measurement parameter setting.

The LSV curves were obtained from 0 V_{RHE} to -1.6 V_{RHE} with interval of 10 mV. The plasmon-assisted CO_2RR experiments under every constant potential (-0.9 V_{RHE}, -1.0 V_{RHE}, -1.1 V_{RHE}, -1.2 V_{RHE}, -1.3 V_{RHE}) were carried out for 3600s under dark and 625 nm LED illumination, respectively. The photocurrent response measurements were carried out at -1.3 V_{RHE} upon 625 nm light chopped every 10 seconds in Ar-saturated and CO_2-saturated 0.1 M $KHCO_3$, which were recorded in interval of 0.01s.

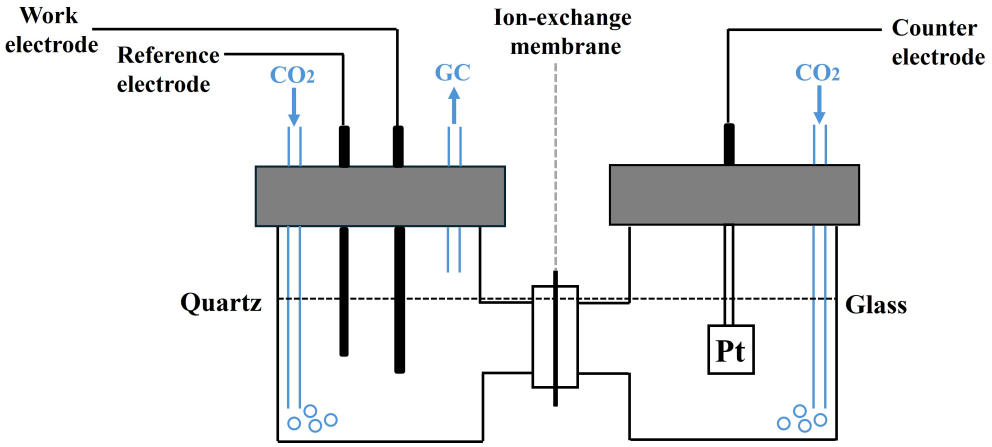

Figure 4.18: The H-cell reactor.

4. Products quantification.

The gas-phase products from cathodic were collected by gas chromatograph (SHIMADZU GC-2014C for external heating experiment, and PerkinElmer Clarus 590 for experiments in dark and illumination conditions). High-purity N2 (99.999%) was used as the carrier gas. The gas products from the cell were injected online every 30 minutes into the GC. The liquid-phase products were detected by proton nuclear magnetic resonance (1H NMR) of the electrolyte after every potential for 1 hour. To prepare the sample for 1H NMR measurement, 0.3 mL electrolyte after reaction, 0.1 mL Deuterium oxide and 0.1 mL Dimethyl sulfoxide (3.37898*10-4 mol/L) were mixed and injected into the NMR tube. The 1H NMR spectra were recorded on Avance III HD 500 MHz Bruker BioSpin spectrometers. The FE of gas and liquid products was obtained by the equation of Faraday efficiency.

In situ attenuated total reflection-infrared spectroscopy (ATR-IR).

ATR-IR was carried out on a Nicolet iS50 FT-IR spectrometer equipped with an MCT detector cooled with liquid nitrogen, as shown in Figure 4.19. First, the Si prism was polished with a slurry of 0.3 μm Al2O3 and sonicated in acetone and deionized water. After polishing, the Si prism was soaked in a piranha solution (3:1 volumetric ratio of 98% H2SO4 and H2O2) for 60 min to clean the prism of organic contaminants. Then the reflecting surface was immersed in a mixture of the Au plating solution at 60 °C for 10 min. 2 mg catalyst was mixed with 970 μL isopropanol and 30 μL Nafion solutions (5 wt%, Sigma-Aldrich) followed by sonication of 30 min to form a homogeneous solution. Then 100 μL of catalyst ink was cast onto the Au film modified Si prism reflecting surface. In situ ATR-IR spectra were recorded during stepping the working electrode potential.

COMSOL simulations.

Electromagnetic simulations were performed using the wave optics module in COMSOL Multiphysics software. The large ball is Pd particle (55 nm), and the small balls are Cu particles (10 nm, 15 nm and 20 nm, respectively). The plane wave was incident backward along the z-axis. The perfect matching layer (PML) was defined to contain the physical domain to absorb all scattered waves. The variables were defined as the wavelength of the excited wave and the radius of the copper particle. Firstly, the background field was calculated, and then the total field and power loss when nanoparticles were introduced were calculated. In the default library, the refractive indices of Pd and Cu were set to dispersion. The variables were defined as the wavelength of the excited wave and the radius of the Cu particle. All simulations used incidence (625 nm) as the excitation source.

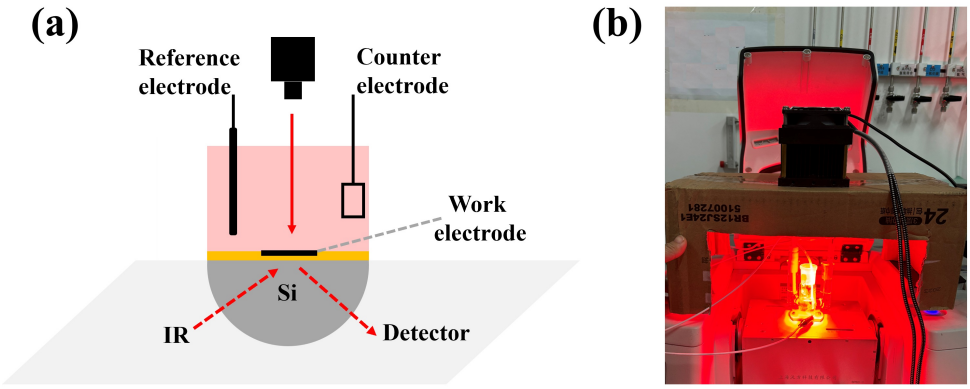

Figure 4.19: FTIR device. Schematic representation of attenuated total reflection surface-enhanced infrared absorption spectroscopy (ATR-SEIRAS).

DFT calculations.

XRD analysis in Figure 4.3 indicates that the Cu, CuPd, and Pd NPs are predominantly composed of (111) facets. HRTEM images further reveal the presence of CuPd(111) and CuPd(100) interfaces (Figure 4.1). The Cu(100) facets have been reported to facilitate the formation of C2 products, while Cu-based bimetallic catalysts with dominant (111) facets have also exhibited high efficiency in catalyzing C-C coupling toward C2 products.[171–173] Therefore, both crystal facets (111) and (100) are considered in this work.

The 4 × 2 supercell CuPd(111) and CuPd(100) periodic surface slab including four atomic layers were built. A vacuum slab with 15 Å was added to avoid the interaction influence of the periodic boundary conditions. Each model contains 128 atoms. The DFT calculations were performed by VASP with the projector augment wave (PAW) method.[174,175] The exchange and correlation potentials are present in the generalized gradient approximation with the Perdewe-Burkee-Ernzerhof (GGA-PBE). A 2 × 2 × 1 Monkhorst-Pack grid of k-point was used for the Brillouin zone integration. The cutoff energy, the convergence criteria for energy and force were set as 450 eV, 10^{-5} eV/atom and 0.02 eV/Å, respectively.

The adsorption energy was calculated by the following formula:

$$E_{ads} = E_{substrate+gas} - \left(E_{substrate} + E_{gas}\right) \tag{4.1}$$

Where $E_{substrate}$ and E_{gas} represent the energy of the isolated substrate and gas molecule, respectively. The $E_{substrate+gas}$ represents the total energy of gas molecule adsorbed on the substrate. The change in Gibbs free energy (ΔG) for each reaction step is given as follows:

$$\Delta G = \Delta E + \Delta ZPE - T\Delta S \tag{4.2}$$

Where ΔE represents the total energy difference between the product and the reactant. ΔZPE and $T\Delta S$ are the zero-point energy correction and the entropy change at 298.15 K, respectively.

5

Plasmonic Enhancement in an Earth-Abundant CuNi Catalyst for Alkaline Hydrogen Evolution Reaction

The content of this chapter is based on our manuscript to be submitted (Wang, Y.-H., Zhu, L., Mariani, E., Pensa, E., Henrotte, O., Xia, Y., Müller-Caspary, K., Zhang, T.-Y., Gao, M.-R., Cortés, E. Plasmonic Enhancement in an Earth-Abundant CuNi Catalyst for Alkaline Hydrogen Evolution Reaction.). As the foundation of the chapter, the current version of manuscript is used. Large language models are used to refine the grammars.

5.1 Research background

Hydrogen (H_2) is one of the most promising energy sources for the next generation by virtue of its zero emissions, renewable characteristics and high gravimetric energy density at 120 MJ/kg, nearly three times that of petroleum.[176,177] Electrochemical and photoelectrochemical water splitting offers an efficient and sustainable pathway towards green H_2 production owing to the abundance of water and the high purity of the produced H_2.[178,179] Owing to the less harsh conditions, the cathodic hydrogen evolution reaction (HER) in alkaline media holds many advantages in cost and stability over that in acid. Unfortunately, precious group metal, especially platinum (Pt)-based materials are still the benchmark catalysts for alkaline HER, owing to their nearly optimal adsorption energies for reaction intermediates, but their high cost significantly limits practical application.[180] Therefore, substantial efforts have been devoted to developing HER catalysts composed exclusively of non-precious elements, among which nickel (Ni)-based compounds have emerged as promising substitutes, benefiting from their moderate affinity towards key intermediates (e.g. *H and *OH).[181] To further optimize their electrocatalytic performance in alkaline HER, a number of strategies have been implemented to modulate the electronic property in Ni active sites, including Ni-based nanoalloys,[182–184] Ni nitrides,[185,186] Ni sulfides,[187] and heterogeneous Ni-based materials.[188–190] Remarkable progress has been made, with some of these catalysts achieving overpotentials below 100 mV at -10 mA cm^{-2}.[177,186,189–192] However, these researches have only been focused on electrocatalysis, neglecting synergistic contributions from other effects

such as photochemistry to electrocatalytic systems, which could further unlock the potential of non-precious metal catalysts in alkaline HER.

Among these contributors, localized surface plasmon resonance (LSPR) has been gaining extensive attention.[193] Plasmonic nanomaterials, notably copper (Cu), Silver (Ag), and Gold (Au) that exhibit LSPR in the optical regime can harness solar energy towards superior catalysis.[194] Under resonant illumination, the collective oscillation of conduction electrons amplifies local electric fields by several orders of magnitude,[195] facilitating the generation of non-equilibrium hot carriers through plasmon decay.[196–198] These hot carriers can either participate directly in surface reactions or relax via electron–phonon coupling, transferring energy to the metal lattice and generating heat.[199] Together, local electric field enhancement, hot carrier generation, and photothermal effect offer significant potential in electrochemistry to modify reaction pathways.[91,99,200–203] However, most existing plasmonic electrocatalysis studies in HER rely on expensive noble metals,[204–207] severely limiting their large-scale application. This underscores the need for earth-abundant, non-noble plasmonic systems[208] that can simultaneously harvest light and catalyze the HER efficiently in alkaline media.

Herein, we demonstrate a plasmonic Cu-Ni nanocatalyst composed entirely of earth-abundant elements for efficient alkaline HER, in which Cu serves as the LSPR light absorber and Ni provides the active sites. Our results showed that under 625 nm LSPR excitation, the CuNi catalyst achieves a very low overpotential 47 mV at the current density of -10 mA cm^{-2}, considerably lower than 106 mV for the dark counterpart and superior to Pt under the same reaction conditions (61 mV). The Tafel slope also dropped from 137 mV dec-1 to 109 mV dec-1 with illumination. Dark-field scattering spectrum and simulated resonant spectrum confirmed the plasmonic effect for our CuNi catalyst at around 625 nm, consistent with the electrocatalytic performance comparison among various illumination wavelengths. In-situ X-ray Photoelectron Spectroscopy (XPS) coupled with Raman and theoretical investigations revealed the contribution of plasmonic effects, which lower activation barriers through hot-electron generation and enhance mass transport via photothermal contributions, thus promoting alkaline HER at both low and high overpotentials. This study demonstrates that plasmonic excitation significantly promotes alkaline HER on a non noble Cu-Ni catalyst, opening up new opportunities to enhance the catalytic activity of non-precious metals for sustainable and affordable chemical production.

5.2 Results and discussion

Catalysts preparation and Plasmon-enhanced HER performance.

We prepared our CuNi catalysts by a pulse electrodeposition method, in which Cu and Ni deposition occurred during the on-time and the off-time allowed ions to diffuse back and re-equilibrate near the electrode surface, as shown in Figure 5.1, enabling a more uniform composition.[209,210] Especially, the Cu/Ni ratio, a critical factor in determining the photochemical performance, could be controlled by adjusting on-time current due to the different reduction potentials of Cu (+0.35 V) and Ni (-0.25 V). In our experiments, the pulse parameters were set as t_{on} = 0.2 s and t_{off} = 0.8 s. During each 0.2 s "on" period, a high cathodic current (j_{on}) drives the reduction of both Cu and Ni ions, and the concentration of ions on the electrode surface decreases. When it comes to 0.8 s "off" period, ions in the electrolyte diffuse to the electrode surface and restore a uniform concentration. This periodic process prevents severe ion depletion and allows the film to grow more uniform. By adjusting j_{on}, the ratio of Cu/Ni can be precisely controlled, due to the electrodeposition of Ni requiring a higher

overpotential than Cu. A higher j_{on} enriches Ni, while a lower j_{on} results in more Cu in the deposit. Meanwhile, too large j_{on} can lead to hydrogen bubble formation and rough surfaces. Thus, a moderate range of j_{on} ensures smooth and compact films with controllable composition. This pulse deposition strategy effectively combines fast nucleation with steady ions replenishment, enabling homogeneous CuNi nanostructures that combine Cu for plasmonic absorption and Ni for electrocatalytic activity.

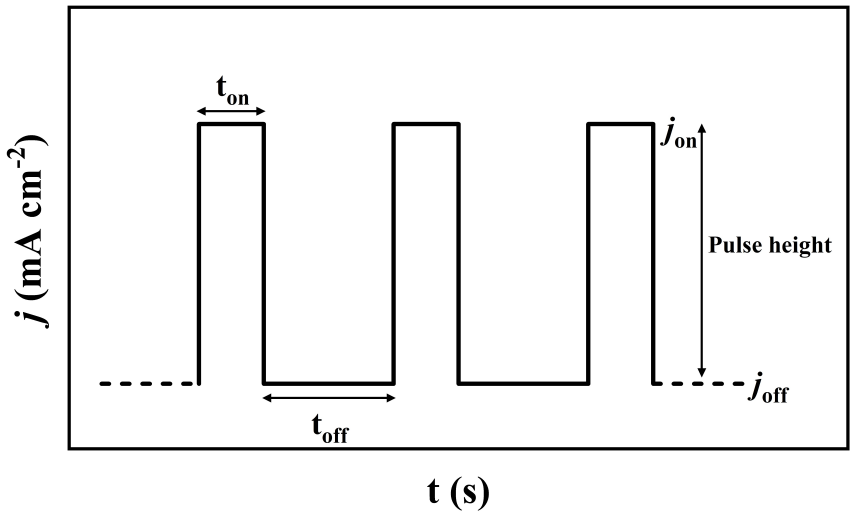

Figure 5.1: Schematic illustration of the pulse deposition procedure. The ton and toff here are 0.2 s and 0.8 s, respectively. The joff is 0 mA and the jon is cathodic.

We started from depositing a series of Cu-Ni catalysts with different deposition current j_d from 30 mA to 120 mA during the on-time on a carbon paper with an area of 0.25 cm^2 carbon paper for 5 min and tested their catalytic behaviors in alkaline HER. Three independent LSV curves (Figure 5.2a) reveal a clear dependence of HER activity on the deposition current. Under dark condition, increasing the deposition current from 30 to 90 mA gradually shifts the polarization curves toward more positive potentials, indicating enhanced catalytic activity, with the overpotential at -10 mA cm^{-2} from 308 mV to 168 mV (Figure 5.2b). The X-Ray diffraction (XRD) patterns show that Ni content was enriched as deposition current increasing from 30 mA to 90 mA, as shown in Figure 5.2d, indicating the role of Ni as active sites. However, further increasing the deposition current from 90 mA to 120 mA made little difference, indicating that the intrinsic activity plateaued at Ni-rich compositions. Under 625 nm LED illumination, all catalysts exhibited a marked improvement, with the sample deposited at 90 mA achieving the lowest overpotential of 71 mV (Figure 5.2b). Although the dark performances of the 90 mA and 120 mA samples were comparable, the CuNi sample deposited at 120 mA showed less improvement under illumination, attributable to partial Cu depletion, thereby confirming the key role of Cu in light absorption. The aforementioned trends were consistent with the Tafel plot, as shown in Figure 5.2c. Under illumination, CuNi samples with different deposition current exhibited a small Tafel slope, and the value decreased with increasing deposition current up to 90 mA, indicating that the HER kinetics were enhanced and the plasmon effect was the strongest at the optimal Cu/Ni ratio.

The surface morphology of the CuNi samples deposited under different current was further observed by SEM, as shown in Figure 5.3. At a low deposition current of 30 mA, the CuNi NPs were relatively sparse. Increasing the deposition current to 60 mA resulted in a denser distribution of CuNi NPs. At a current of 90 mA, the surface of CuNi NPs surface began to densely accumulate with regular shape. When increasing the deposition current further to 120 mA, it resulted in larger CuNi NPs.

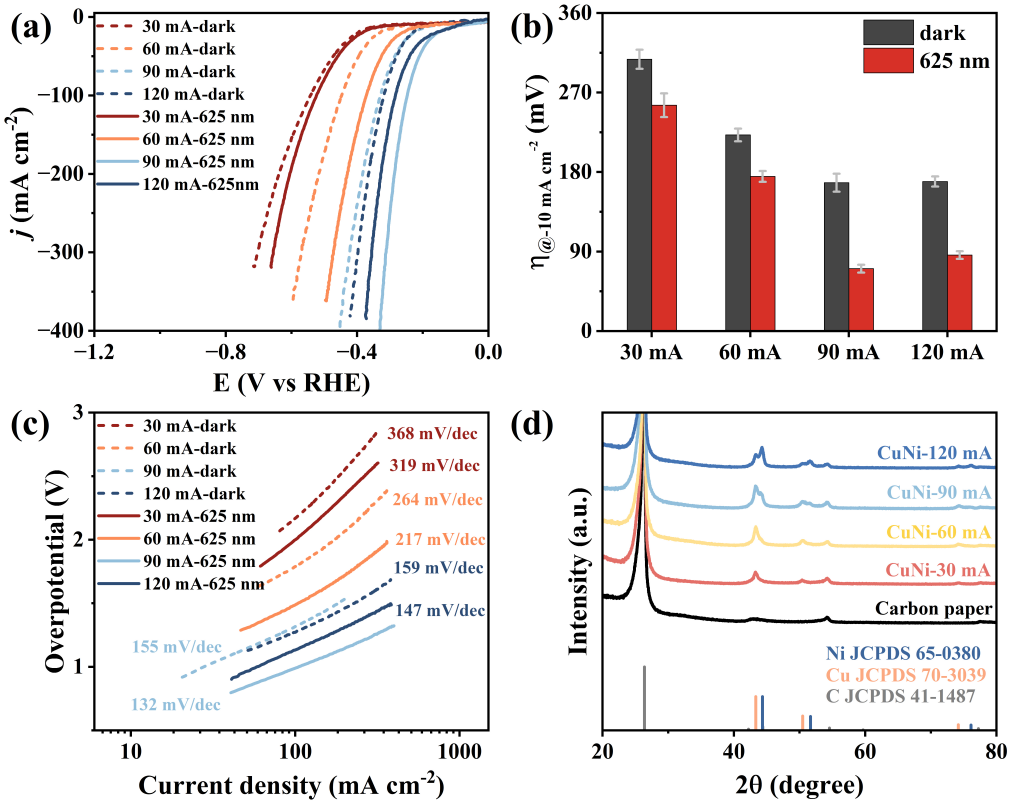

Figure 5.2: Performance of CuNi NPs with different deposition current. (a) HER polarization curves of the CuNi catalysts deposited for 5 min at 30, 60, 90 and 120 mA, measured both in the dark and under 625 nm illumination in Ar-saturated 1 M KOH. Sweep rate: 5 mV s-1. Comparison of (b) the overpotential (η) at -10 mA cm^{-2} and (c) the Tafel slope of the CuNi catalysts deposited for 5 min at 30, 60, 90 and 120 mA under dark and illumination conditions. (d) XRD patterns of CuNi catalysts deposited at 30 mA, 60 mA, 90 mA, and 120 mA, taking empty carbon paper as the reference.

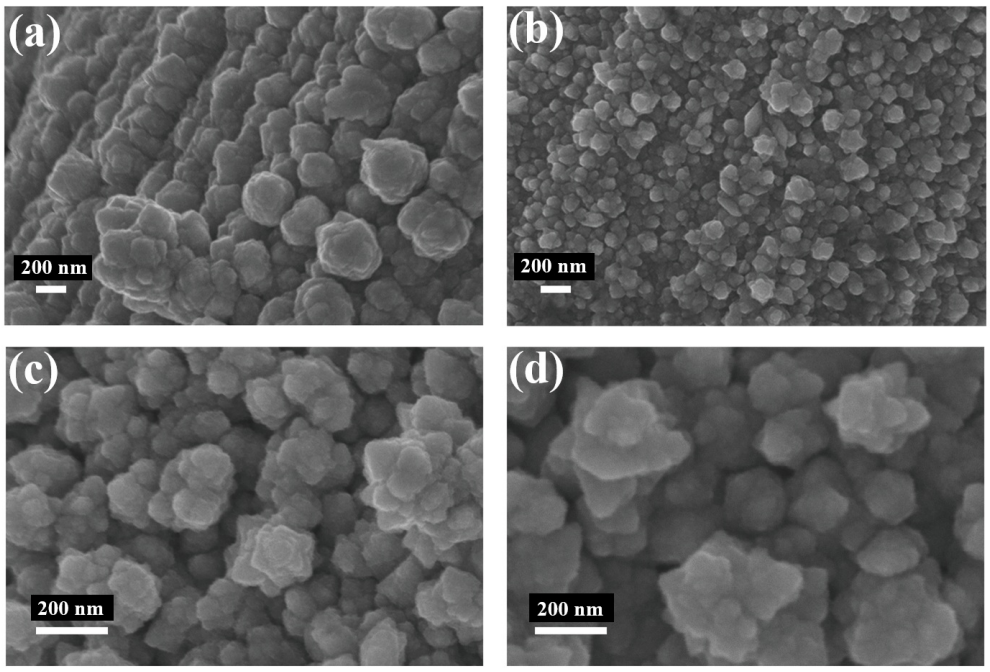

Figure 5.3: SEM images of CuNi NPs with different deposition current. SEM images of CuNi catalysts deposited at (a) 30 mA, (b) 60 mA, (c) 90 mA, and (d) 120 mA.

We subsequently optimized the performance of CuNi NPs with fixed deposition current 90 mA by extending the total deposition time to achieve higher catalyst loadings, as show in Figure 5.4a. When the deposition time was increased to 10 min, yielding a CuNi catalyst loading of 3.2 mg cm^{-2}. The CuNi catalyst with deposition time of 10 min exhibited remarkable catalytic activity requiring an overpotential of only 106 mV to reach -10 mA cm^{-2} in the dark, and this value was further significantly reduced to 47 mV under 625 nm illumination, as shown in Figure 5.4b. This was also in accordance with Tafel plot, revealing a promising slope of 137 mV dec-1 in the dark that improved to 109 mV dec-1 under 625 nm illumination, as shown in Figure 5.4c. Further increasing deposition time to 15 min produced minor changes owing to the saturation of active sites.

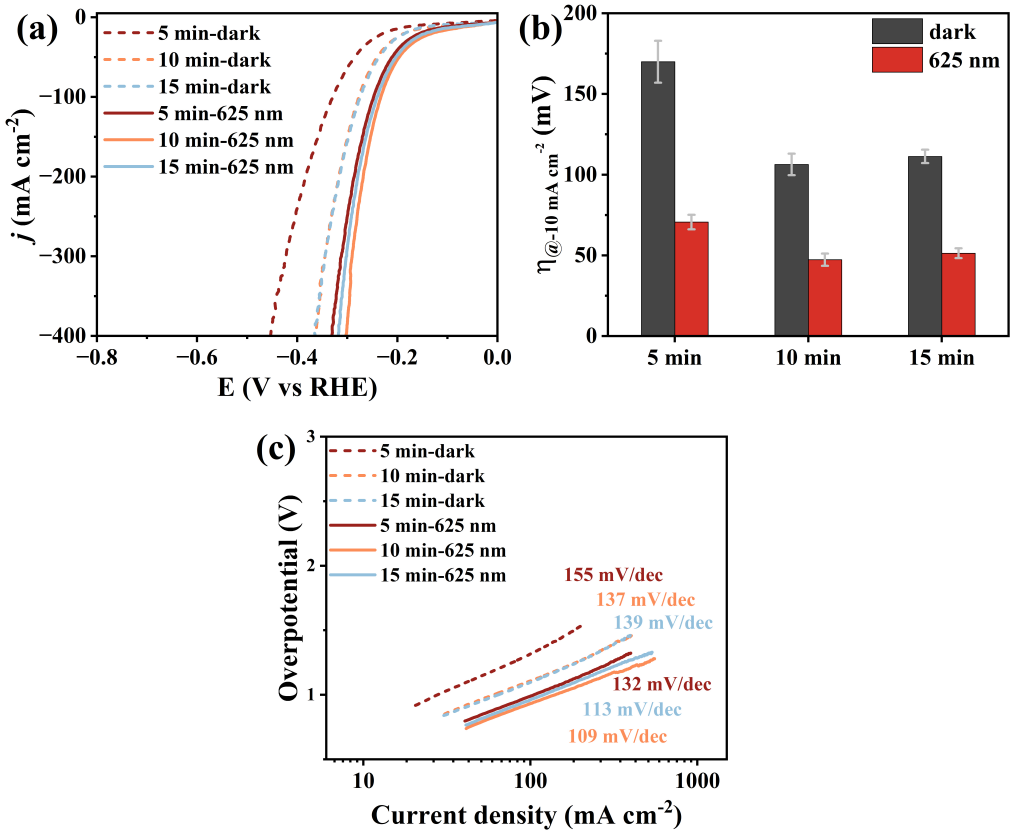

Figure 5.4: Performance of CuNi NPs with different deposition time. (a) HER polarization curves of the CuNi catalysts deposited at 90 mA for 5, 10 and 15 min, measured both in the dark and under 625 nm illumination in Ar-saturated 1 M KOH. Sweep rate: 5 mV s-1. Comparison of (b) the overpotential (η) at -10 mA cm^{-2} and (c) the Tafel slope of the CuNi catalysts deposited at 90 mA for 5, 10 and 15 min under dark and illumination conditions.

Consequently, we fixed the deposition parameters with depostion current of 90 mA and deposition time of 10 min in the following experiments. Depositing Cu and Ni separately with the same procedure and parameters serve as the control group. The Cu catalysts exhibited poor performance and high impedance under both dark and illumination conditions, as shown in Figure 5.5a-5.5c. The Ni catalysts exhibited much better performance than Cu catalyst under both dark and illumination conditions. However, Ni NPs exhibited no photo-response and Cu possessed inherently low catalytic activity. Remarkably, our CuNi catalyst under 625 nm illumination only required 47 mV, which outperformed commercial Pt that required 61 mV to reach -10 mA cm^{-2} (Figure 5.5b). Moreover, accelerated durability test (ADT) of CuNi catalyst under 625 nm illumination revealed only a slight activity decay after 10,000 cycles, whereas the overpotential slightly increased from 47 mV to 66 mV (Figure 5.5d), demonstrating excellent durability under light illumination. The SEM images of the CuNi

catalyst after 10,000 cycles of ADT test showed no obvious structural changes confirming the exceptional structural stability of the CuNi catalyst, as shown in Figure 5.6a-5.6b.

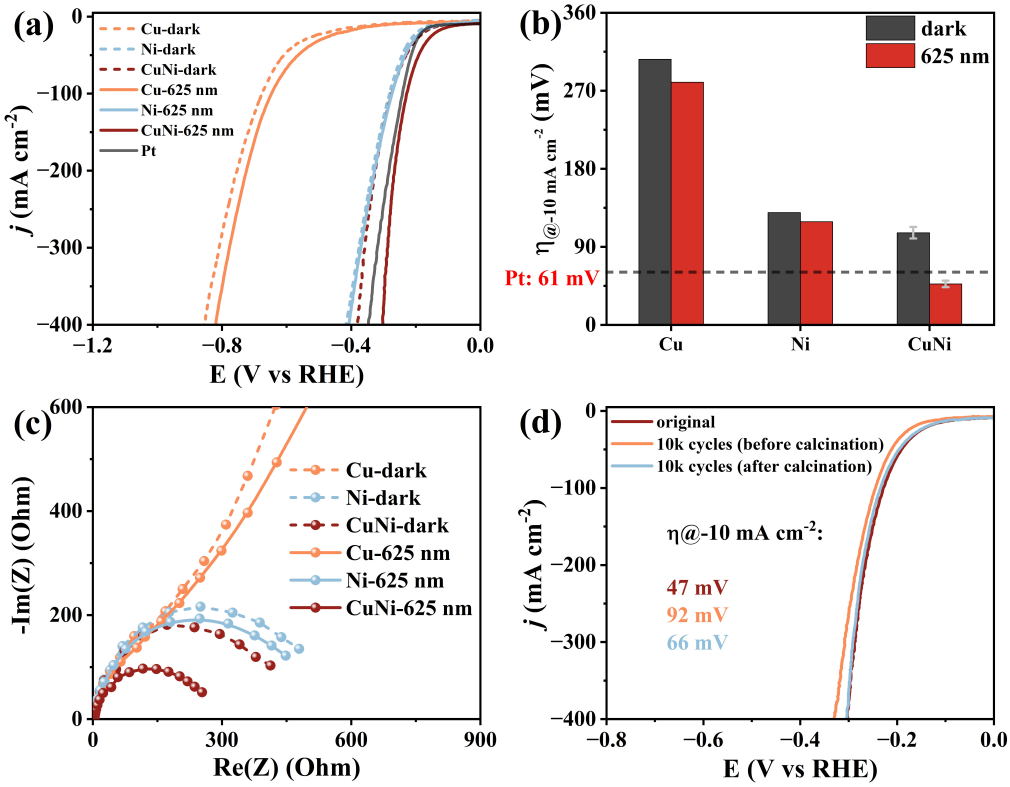

Figure 5.5: Performance of CuNi NPs deposited at 90 mA for 10 min. (a) HER polarization curves of CuNi, Cu and Ni deposited at 90 mA for 10 min with Pt as the reference, measured both in the dark and under 625 nm illumination in Ar-saturated 1 M KOH. Sweep rate: 5 mV s-1. (b) Comparison of the overpotential (η) at -10 mA cm^{-2} for the CuNi, Cu and Ni catalysts deposited at 90 mA for 10 min. (c) Electrochemical Impedance Spectroscopy (EIS) for CuNi, Cu, and Ni samples deposited at 90 mA for 10 min in Ar-saturated 1M KOH both under 625 nm illumination and in dark. (d) Accelerated durability tests (ADT) for CuNi deposited at 90 mA for 10 min in Ar-saturated 1M KOH under 625 nm illumination at a sweep rate of 200 mV s-1, recording the polarization curves after different aging cycles at 5 mV s-1.

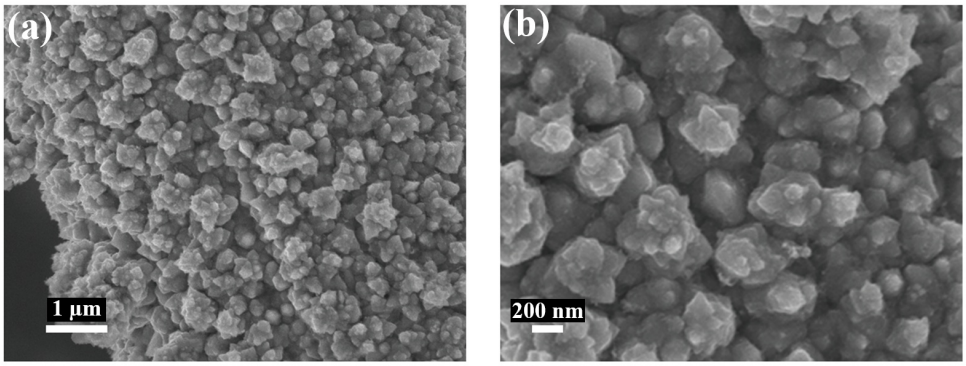

Figure 5.6: (a, b) SEM images of the CuNi catalyst deposited at 90 mA for min after 10,000 cycles ADT test.

We further benchmarked its performance against other plasmonic-enhanced catalysts for alkaline HER, as shown in Figure 5.7a, demonstrating its superiority across several dimensions.[204–207] Besides, it also surpassed a lot of the previous reported Pt group metal (PGM)-free electrocatalysts (Figure 5.7b).[183,186–192,211–214]

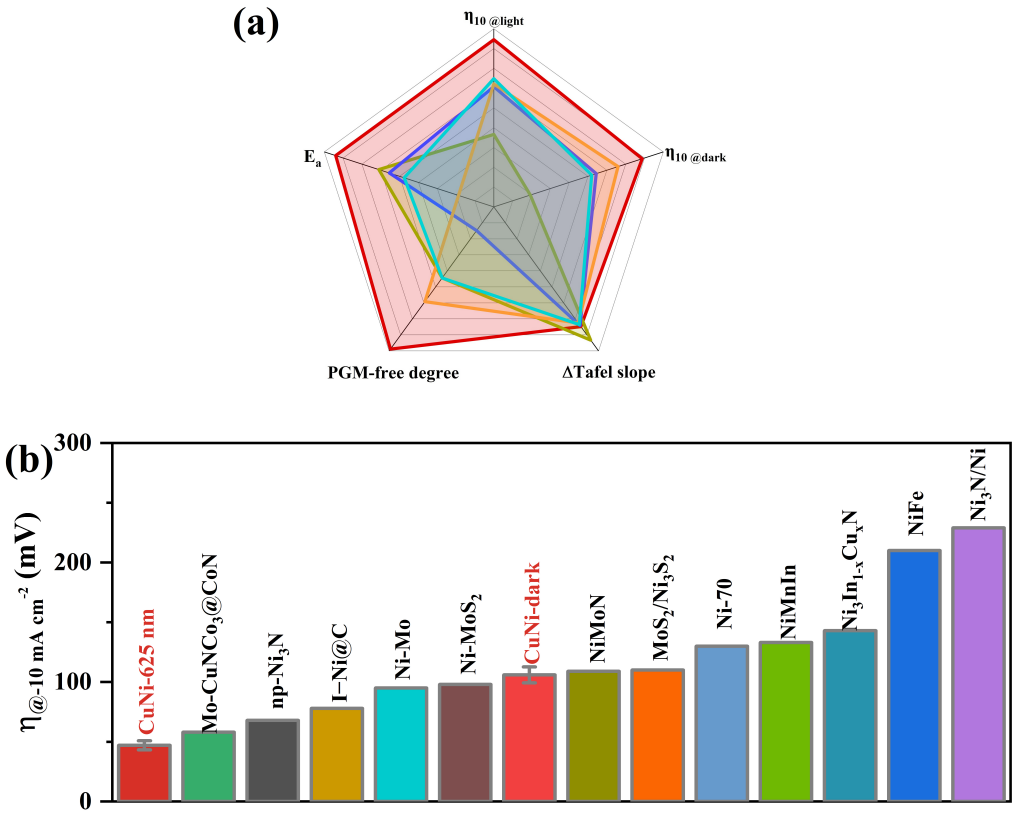

Figure 5.7: Performance comparison with PGM-free HER catalysts. (a) Radar chart comparing various aspects among several plasmon enhanced catalysts in alkaline HER. (b) Comparison of the η at -10 mA cm^{-2} among CuNi catalyst in dark, CuNi catalyst under 625 nm illumination and various PGM-free HER catalysts reported previously.

Catalysts characterization.

We then characterized the structure and chemical state of the CuNi catalyst by a set of analysis techniques. High-angle annular dark-field scanning transmission electron microscopy (HAADF-STEM) image in Figure 5.8a showed that the diameter of CuNi NPs was around 60 nm. The uniform contrast and well-defined boundaries of CuNi NPs, indicating good crystallinity and uniform growth during the electrodeposition process. The corresponding energy-dispersive X-ray spectrum (EDX) elemental mapping revealed the elemental distribution of Cu (orange) and Ni (blue). The signals of Cu and Ni are not uniformly distributed, but rather exhibit distinct compositional variations, with clear Cu-rich and Ni-rich areas. Specifically, EDX quantification revealed that the Cu-rich domains contained approximately 85.7% Cu, while the Ni-rich domains contained approximately 93.3% Ni. These observations suggest a partial phase segregation of the two metals at the nanoscale, likely due to their different reduction potentials during electrodeposition.

X-ray diffraction (XRD) patterns further confirm the structural characteristics of the CuNi catalyst, as shown in Figure 5.8b. The diffraction peaks of the CuNi sample closely match those of metallic Cu (JCPDS No. 70-3039) and Ni (JCPDS No. 65-0380). The main 2θ reflections for Cu are approximately 43.3°, 50.4°, and 74.1°, while the main 2θ reflections for Ni are approximately 44.5°, 51.8°, and 76.4°. Notably, the CuNi catalyst exhibited two distinct sets of peaks, corresponding to the Cu and Ni phases, respectively, with no intermediate alloy peak detected between them, indicating that Cu and Ni existed primarily as separate crystalline domains rather than forming a solid solution. As shown in Figure 5.8c, the energy-dispersive X-ray (EDX) spectrum collected over a wide area reveals characteristic emission peaks from Cu and Ni. Clear peaks of Ni and Cu are observed in the low-energy region and

high-energy region. No other peaks associated with impurities are detected, indicating the high purity of the deposited CuNi catalyst. Quantitative analysis based on multiple EDX spectra revealed an overall atomic ratio of Cu to Ni of approximately 1:1, consistent with the elemental distribution observed in STEM-EDX spectroscopy. These results confirm that the CuNi catalyst consists of coexisting Cu-rich and Ni-rich regions, rather than a single solid solution alloy.

Figure 5.8 (d,e) shows the high-resolution XPS spectra of Ni 2p and Cu 2p for the CuNi catalyst together with the monometallic Cu and Ni. In the Ni 2p region (Figure 5.8d), the spectra can be deconvoluted into the metallic doublet Ni^0 $2p_{3/2}$ and Ni^0 $2p_{1/2}$, minor Ni^{2+} components, and the characteristic shake-up satellites. For pure Ni, the main Ni^0 $2p_{3/2}$ peak is centered at $\tilde{8}52.83$ eV, whereas it red-shifted to $\tilde{8}52.56$ eV in CuNi. In the Cu 2p region (Figure 5.8e), both samples exhibited a dominant Cu^0 $2p_{3/2}$ peak and an accompanying Cu^0 $2p_{1/2}$ feature. Importantly, no obvious Cu^{2+} satellite was detected for CuNi, indicating the absence of significant Cu^{2+} species under the measurement conditions. Compared with pure Cu (Cu^0 $2p_{3/2}$ at $\tilde{9}32.17$ eV), the CuNi sample showed a slight blue shift of peak to $\tilde{9}32.40$ eV. The opposite energy shifts of Ni $2p_{3/2}$ (to lower binding energy) and Cu $2p_{3/2}$ (to higher binding energy), together with the suppressed Cu^{2+} satellites, consistently point to an interfacial electron redistribution from Cu to Ni in CuNi NPs, indicating Cu acted as an electron donor while Ni behaved as an electron acceptor. Such a direction charge transfer is physically reasonable given the larger work function of Ni relative to Cu, which lowers the surface potential on Ni domains and raises it on Cu domains. Overall, the XPS results confirm that Ni and Cu were predominantly metallic in CuNi, and there was electron transfer from Cu to Ni, which is beneficial for supplying electrons to the Ni active sites during alkaline HER.[215]

Mechanism of plasmon-enhanced HER.

To confirm the key role of LSPR in the photo-induced activity improvement, we investigated the mechanism of light response for CuNi. As shown in Figure 5.9a, dark-field optical images clearly distinguished the carbon fiber substrate (top) and the CuNi deposited region (bottom). The bare carbon fiber exhibited negligible scattering, while the CuNi-coated region exhibited bright yellow-orange scattering, confirming strong light-matter interaction and indicating the presence of LSPR modes in the visible region. The uniform brightness along the fiber indicates that the CuNi NPs are uniformly distributed and optically active across the entire surface. Figure 5.9b shows the corresponding dark-field scattering spectrum of the CuNi catalyst (solid line) and the simulated extinction spectrum (dashed line) obtained by finite-difference time-domain (FDTD) calculations. The dark-field scattering spectrum shows a prominent resonance centered at 645 nm, with minimal spectral shift between the experimental and simulated environments. This slight deviation is likely due to differences in nanoparticle morphology, surface roughness, and the local refractive index between the experimental and simulated environments. The experimental scattering spectrum are highly consistent with the FDTD simulation results. The strong plasmon response at 645 nm corresponds to the 625 nm illumination used in the plasmon-enhanced electrocatalytic tests, indicating that 625 nm light can effectively activate the LSPR in the CuNi catalyst, thereby enhancing charge transfer and catalytic performance.

To further elucidate the wavelength dependence of the plasmon-enhanced HER, the performance of CuNi catalysts under monochromatic illumination at different wavelengths (405, 525, 560, 625, and 730 nm) was systematically evaluated. As shown in Figure 5.9c, the polarization curves show a clear wavelength-dependent trend. Compared to dark conditions, illumination at all visible light enhanced the catalytic current densities, confirming the

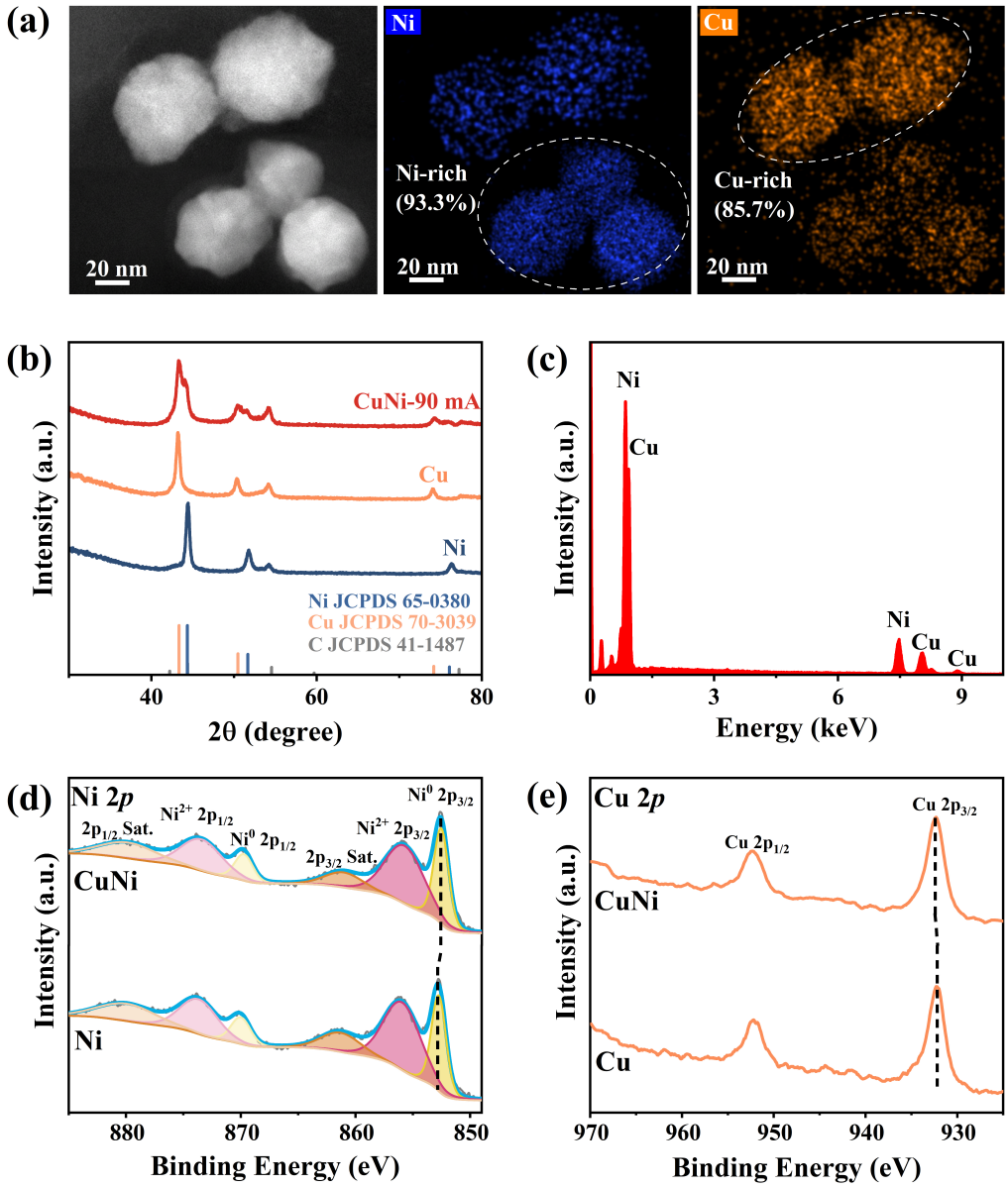

Figure 5.8: Structural characterization and surface analysis of CuNi catalyst. (a) HAADF-STEM image of the CuNi catalyst, and corresponding EDX elemental mapping of Ni and Cu. (b) XRD patterns of the CuNi, Cu and Ni catalysts deposited on carbon paper. (c) Scanning electron microscopy-energy-dispersive X-ray (SEM-EDX) spectrum over a broad area on the CuNi deposited carbon paper. (d) Ni 2p XPS spectra of CuNi and Ni. (e) Cu 2p XPS spectra of CuNi and Cu.

positive contribution of plasmon excitation to the HER process. Notably, as the illumination wavelength increased from 405 to 625 nm, the polarization curves gradually shifted toward more positive potentials, indicating enhanced catalytic activity and accelerated charge transfer kinetics. However, the enhancement weakened when the wavelength further increased to 730 nm, indicating a decrease in the efficiency of plasmon excitation in the near-infrared region. Figure 5.9d showed the changes of overpotential as wavelength increasing at a current density of 10 mA cm^{-2}. The overpotential decreased continuously from 110 mV in dark condition to a minimum of 43 mV under 625 nm illumination, then rised again at 730 nm LED. This strong correlation between optical resonance and catalytic activity directly demonstrates that the HER enhancement originated from LSPR excitation.

Plasmon-induced hot electrons are closely associated with local electric field enhancement on the surface of plasmonic nanomaterials, where a stronger near-field favors the generation

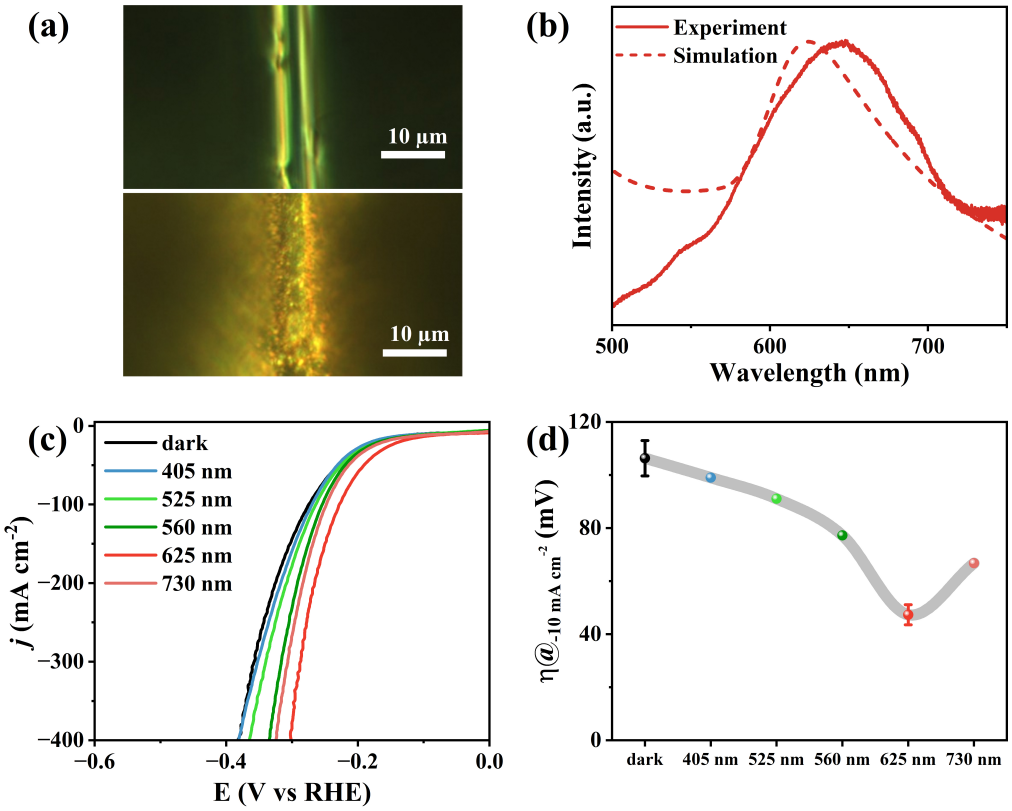

Figure 5.9: Wavelength dependence. (a) Dark-field images of a carbon fiber (up) and the CuNi catalyst on a carbon fiber (down). (b) Resonant spectra of the CuNi catalyst, where the solid line is the Dark-field scattering spectrum and the dashed line is the simulated extinction spectrum by FDTD. (c) HER polarization curves of the CuNi catalyst measured in the dark and under illumination from LEDs of various wavelengths in Ar-saturated 1 M KOH. Sweep rate: 5 mV s-1. (d) Comparison of the η at -10 mA cm^{-2} corresponding to the polarization curves in (c).

of hot electrons.[134,135] We then performed electromagnetic simulation using the FDTD method. Our HAADF analysis revealed that the CuNi NPs are composed of phase-separated Cu and Ni domains with negligible inter-doping, which coexist throughout the entire catalyst system. To investigate the photo-induced LSPR effect and the associated charge transfer from Cu to Ni, we simplified the system and modeled it as two adjacent nanoparticles (radius = 30 nm). We identified a pronounced local electromagnetic field at the Cu-Ni interface under 625 nm illumination, as shown in Figure 5.10a.

Furthermore, to directly probe the charge dynamics under illumination, we employed in situ Raman-XPS measurements. For our CuNi catalyst, increasing the laser power from 0 to 10 mW induced a positive shift in the Cu 2p3/2 signal from 932.40 eV to 932.89 eV (Figure 5.10b), accompanied by a simultaneous negative shift of the Ni 2p3/2 signal from 852.65 eV to 852.35 eV (Figure 5.10c). This opposing shift of the core levels provides compelling evidence for a directional, plasmon-mediated charge transfer, where hot electrons are generated on the Cu nanoantennas and subsequently injected into the Ni active sites.[216] The charge transfer could facilitate H_2O dissociation kinetics by providing electrons for the Volmer step:

$$M-H_2O + e^- \rightarrow OH^- + M-H$$

thereby accelerating alkaline HER. In contrast, pure Ni showed no peak shift under illumination, as shown in Figure 5.10d. In addition, we observed an increment in the Cu 2p3/2 peak intensity under the stepwise amplified illumination. This could be attributed to the altered surface charge environment and scattering pathways arising from plasmon-generated hot

electrons and the associated photothermal effect, which increase the escape probability of photoelectrons and thus enhance the XPS peak intensity.[217]

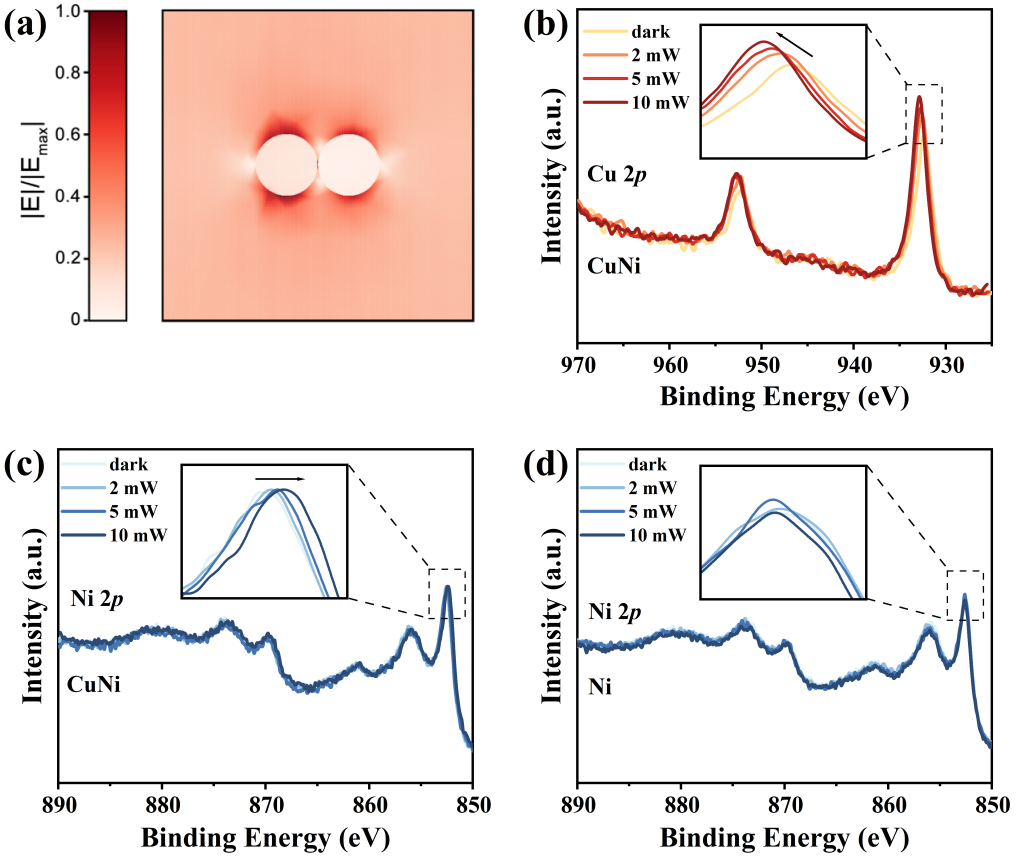

Figure 5.10: Local electric field and hot electrons. (a) Simulated two-dimensional electrostatic field distribution maps of the CuNi catalyst, with the left ball resembling Cu-rich and the right ball resembling Ni-rich part. Ball radius: 30 nm. (b) Cu 2p and Ni 2p (c) XPS of the CuNi catalyst measured under illumination ($\lambda \approx 532$ nm; 0–10 mW). Insets show the magnified view of the Cu $2p_{3/2}$ (b) and Ni $2p_{3/2}$ (c) main peaks. (d) XPS of pure Ni deposited on carbon paper measured under illumination ($\lambda \approx 532$ nm; 0–10 mW).

Next, we further elucidated the specific mechanism by which LSPR effect enhanced alkaline HER. Photocurrent response can help us to quantify the contributions of hot electrons and the photothermal effect, in which the rapid initial current jump (0.05 s) was due to hot electrons and the subsequent current increase (0.05 s to 10 s) owed to photothermal effect (Figure 5.11a).[218] It was clearly observed that hot electron effect predominated at lower cathodic overpotential, however, with increasing overpotential, the photocurrent enhancement became increasingly governed by photothermal contributions (Figure 5.11b). This transition reflects a shift in the driving forces for alkaline HER. It is widely recognized that Volmer step is the rate-determining step (RDS) for alkaline HER.[219] At low overpotentials, the supply of electrons is limited, and the injection of plasmon-generated hot electrons provides additional reactants for the Volmer step, thereby accelerating water dissociation kinetics. At high overpotentials, however, electrons are abundant and the active sites are saturated, leaving mass transport (including H_{ad} desorption, H_2 transport and OH^- diffusion) as the major bottleneck. In this regime, the local heating induced by photothermal effects plays a more dominant role by promoting diffusion of reactants and products and thus sustains high-rate HER.

To substantiate the enhanced electron spillover under illumination, we carried out potential of zero charge (PZC) measurements using the Gouy-Chapman capacitance minimum

method,[220] since the PZC is directly related to the work function that reflects the ease of electron emission from the surface.[221] The PZC of CuNi decreased substantially from 0.70 V to 0.30 V, indicating more facile electron availability for the reactants, whereas that of pure Ni remained nearly unchanged at 0.80 V (Figure 5.11c). This change could be partially ascribed to photothermal effects, as the PZC was reduced from 0.70 V to 0.64 V when the temperature was raised from 25 ℃ to 55 ℃ (Figure 5.11d). In addition, the reduced PZC implies a weakened interfacial electric field, which facilitates the reorientation of water molecules and enhances mass transport within the double layer[222]—a phenomenon also reported in the context of plasmonics by Kim et al.[223]—thereby accelerating alkaline HER. The plasmonic-driven water reorientation was also reported by Kim et al.[223]

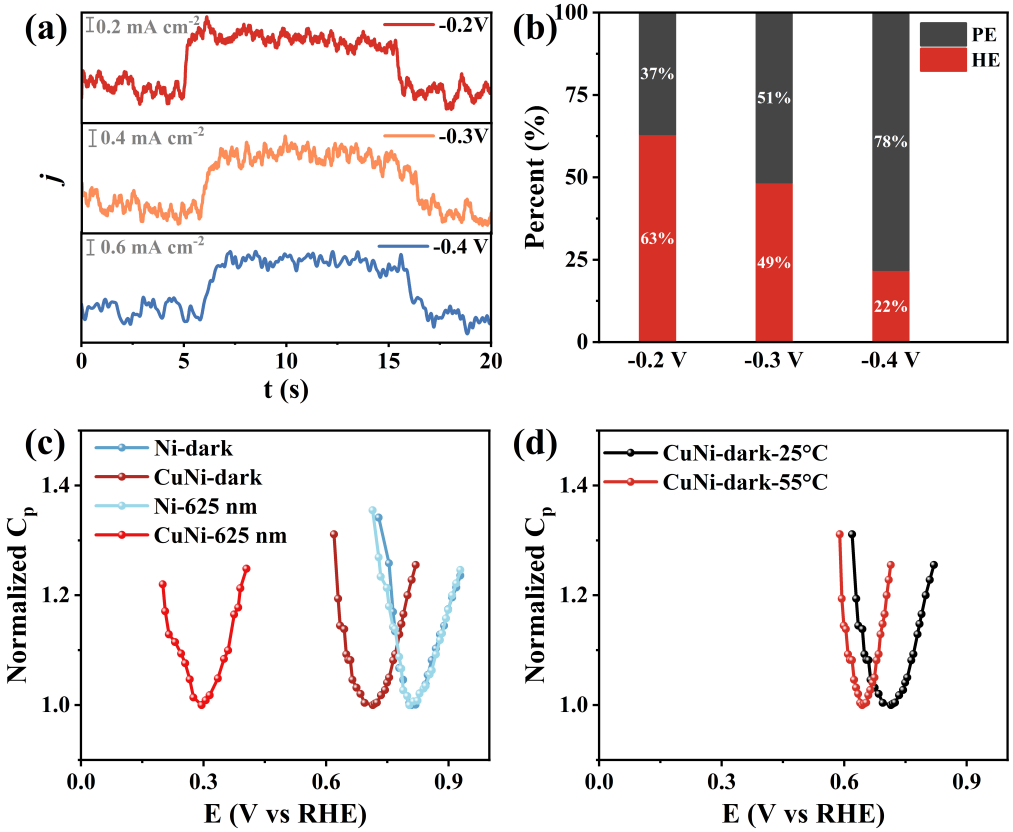

Figure 5.11: Photocurrent response and PZC. (a) Photocurrent response of the CuNi catalyst under chopped 625 nm illumination (10 s interval) at -0.2, -0.3 and -0.4 V_{RHE} in Ar-saturated 1 M KOH. (b) Contributions of the photothermal effect (PE) and hot-electrons effect (HE) at -0.2, -0.3 and -0.4 V_{RHE} derived from the photocurrent response in (a). (c) Potential of zero charge (PZC) measurements for CuNi and Ni obtained using the Gouy-Chapman capacitance minimum method. (d) PZC measurements for the CuNi catalyst at 25℃ and 55℃ in dark condition, obtained using the Gouy-Chapman capacitance minimum method.

Moreover, an analogy of photothermal effect was established by external heating, showing an obvious performance improvement with elevated temperature under both illumination and dark conditions, as shown in Figure 5.12a and 5.12c. Based on the temperature gradient experiment, we further examined the effect of light on the reaction activation energy (Ea) by the Arrhenius plots under 625 nm illumination (Figure 5.12b) and dark condition (Figure 5.12d). In Arrhenius plots, the current densities at different temperatures were extracted from the LSV curves at fixed overpotentials, and the natural logarithm of current density (ln j) was plotted against the reciprocal temperature (1/T) to determine the activation energy. According to the results deduced by Arrhenius plot, the Ea dropped from 36.9 ± 0.8 kJ mol-1 in dark to almost half of that for 18.8 ± 0.4 kJ mol-1 under 625 nm illumination (Figure 5.12e), which

suggested a reduced reaction energy barrier. This decrement was reported to originate from direct hot-electron injection into Ni active sties.[205] Furthermore, we validated this by DFT calculation of water dissociation process, demonstrating that adding two electrons to Ni sites lowered the energy barrier from 0.38 to 0.30 eV (Figure 5.12f), confirming the role of hot electrons in reducing the barrier.

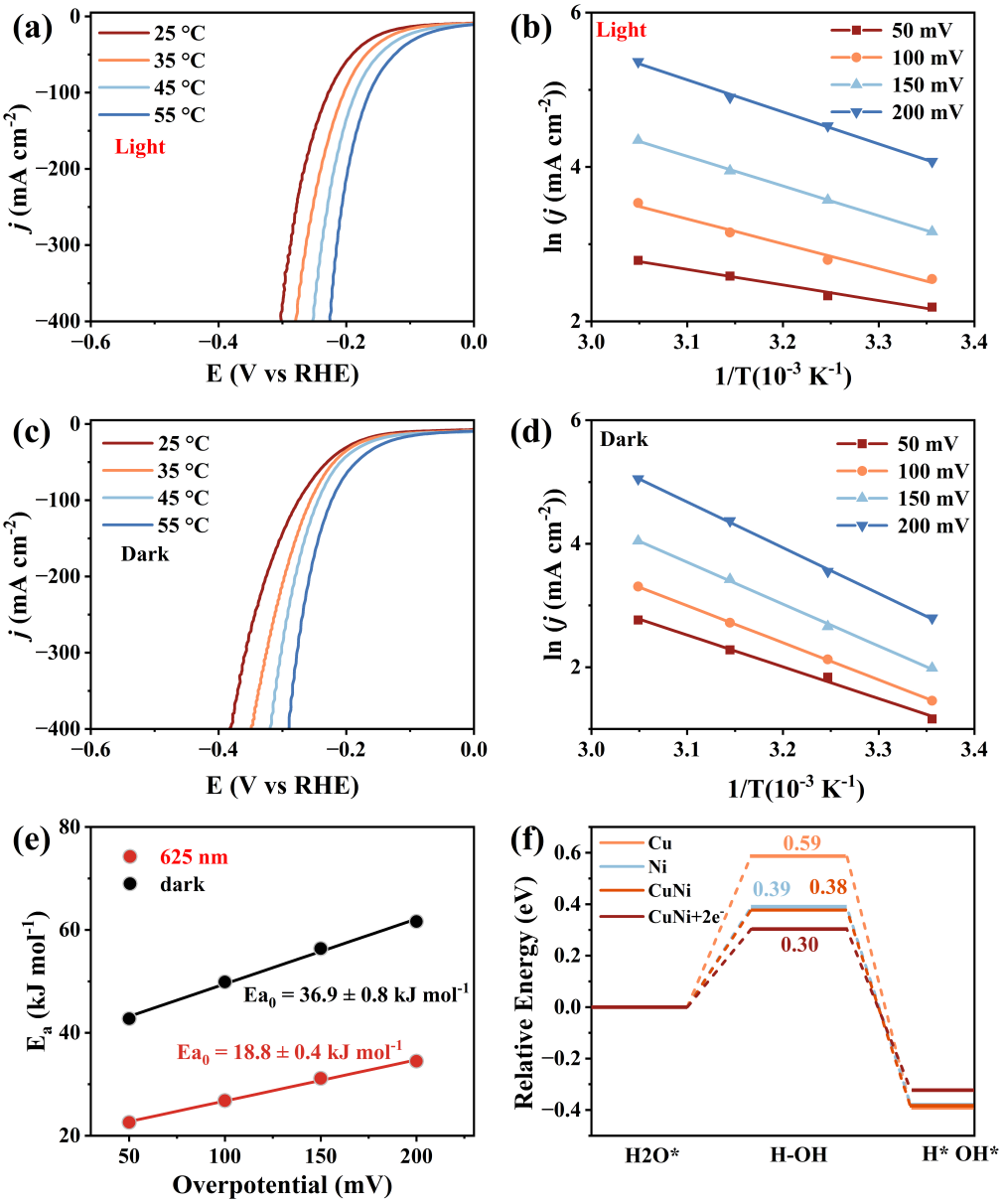

Figure 5.12: Arrhenius analysis and DFT calculation. (a) HER polarization curves of the CuNi catalyst at 25, 35, 45 and 55 ℃ under 625 nm illumination. (b) Arrhenius plots recorded at different overpotentials under 625 nm illumination. (c) HER polarization curves of the CuNi catalyst at 25, 35, 45 and 55 ℃ in dark condition. (d) Arrhenius plots recorded at different overpotentials under dark conditions. (e) Activation energy (Ea) with the 625 nm light on and off; the Ea at the zero overpotential was determined by trend extrapolation. (f) The calculated energy diagram of the HER at the equilibrium potential for various catalysts.

Based on these experimental findings, we propose the underlying mechanism responsible for the exceptional alkaline HER performance of CuNi under 625 nm illumination (Figure 5.13). Hot electrons generated via the LSPR effect actively participate in the Volmer step on Ni active sites, rapidly activating the reaction at relatively low overpotentials. The injected hot electrons can also be emitted more readily, mitigating the interfacial electric field to facilitate interfacial water reorientation. Meanwhile, photothermal heating at the catalyst-electrolyte interface

promotes mass transport—a contribution more critical at higher overpotentials—especially the diffusion of OH^-, H_2O and H_2, ensuring efficient reactant supply and product removal at higher overpotentials. Collectively, the LSPR effect on the CuNi cocatalyst boosts alkaline HER primarily by greatly promoting the Volmer step.

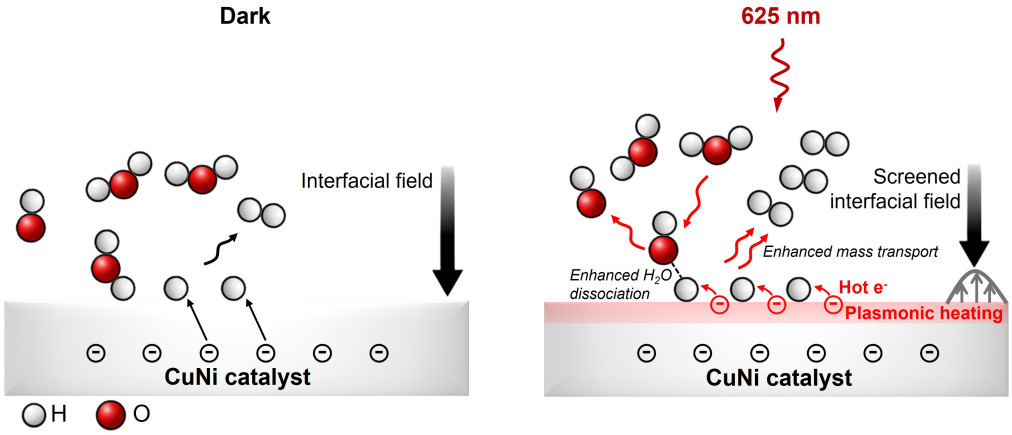

Figure 5.13: Schematic diagram. The schematic diagram of alkaline HER on the CuNi catalyst under dark and 625 nm illumination. White balls, H atoms; red balls, O atoms.

5.3 Summary

To conclude, we investigated plasmon-enhanced electrocatalysis for alkaline HER using earth-abundant CuNi catalysts. The CuNi catalyst exhibited an exceptionally low overpotential of 47 mV at a current density of 10 mA cm^{-2} under 625 nm illumination, about twofold lower than in the dark and even surpassing Pt. This enhancement originated from a pronounced LSPR resonance centered around 640 nm. Upon illumination, hot electrons are generated in Cu and transferred to Ni, taking part in the Volmer step and thereby lowering the activation energy. In addition, photothermal effect raises the interfacial temperature and facilitates mass transfer processes. Together, these effects accelerate alkaline HER over the entire potential range. We envision that our catalyst and mechanistic insights—leveraging plasmonic effects to enhance catalytic performance—will inspire the design of next-generation Pt group metal (PGM)-free catalysts for alkaline HER, potentially overcoming current performance limitations and offering a viable alternative to precious metal-based systems.

5.4 Method

Material synthesis. $NiSO_4{\cdot}6H_2O$ ($\geq$ 98.0%), $CuSO_4{\cdot}5H_2O$ ($\geq$ 98.0%), and $Na_3C_6H_5O_7$ ($\geq$ 99.0%) were purchased from Sigma-Aldrich. Potassium hydroxide (EMPLURA) was bought from Merck KGaA. Toray Carbon Paper (TGP-H-060) was used in our experiments. All chemicals were used as received without further purification.

Electrodeposition procedure: We first prepared the electrodeposition solution by dissolving 2.62 g $NiSO_4{\cdot}6H_2O$, 0.05 g $CuSO_4{\cdot}5H_2O$, and 2.94 g $Na_3C_6H_5O_7$ in 100 mL deionized water (DIW), followed by adjusting the pH of solution to 4.2 with 1 M H_2SO_4. Before deposition, the TGP-H-060 substrate was hydrophilized by oxygen plasma treatment for 10 min. Then, CuNi cocatalysts were deposited onto 0.25 cm^2 carbon paper via pulse deposition with 0.2 s on and 0.8 s off per cycle, using a three-electrode configuration. A Pt foil and an

Ag/AgCl electrode (saturated in 3.0 M KCl) were used as the counter and reference electrodes, respectively. For the deposition of pure Cu and pure Ni, $NiSO_4 \cdot 6H_2O$ and $CuSO_4 \cdot 5H_2O$ were respectively omitted while maintaining all other deposition parameters.

CuNi Catalyst loading on carbon paper was determined gravimetrically. Specifically, the carbon paper was weighed before and after electrodeposition of CuNi catalyst, which was performed at a constant current of -90 mA for 10 min. The difference in mass before and after deposition corresponded to the mass of the deposited CuNi catalyst. Three independent electrodeposition were performed to ensure reproducibility, and an average loading value was calculated from these measurements. Detailed data obtained for each run are provided in Table 5.1. On average, the CuNi catalyst loading was 3.2 mg cm^{-2}.

Table 5.1: Catalyst loading of CuNi samples obtained from three independent runs.

Run	Before (mg)	After (mg)	Catalyst (mg)	Loading (mg cm^{-2})
1	7.3	8.2	0.9	3.6
2	7.2	7.9	0.7	2.8
3	7.3	8.0	0.8	3.2

Material characterization. The as-prepared catalysts were characterized by multiple analytical techniques. The SEM images and corresponding EDX mappings were captured in GeminiSEM 450. The XRD was conducted on an X'Pert PRO PANalytical instrument (Ni-filtered Cu Kα radiation source) from 20° to 80° with a scanning step of 5° per min. In-situ XPS were recorded on a Thermo Scientific Nexsa G2 surface analysis spectrometer, equipped with a low-power monochromatic Al K X-ray source along with simultaneous illumination of a laser of wavelength 532 nm. During the XPS measurements (under the dark and illumination), the position of the sample and the X-ray focus spots were kept constant to avoid any discrepancies in measuring the data. Dark-field scattering spectra were recorded with a WiTec imaging microscopy setup.

Electrochemical measurements. All electrochemical measurements were performed in a standard three-electrode system with the VSP-300 Potentiostat (Bio-Logic, France). During the voltammetry measurement, the electrolytes were stirred magnetically at the rate of 500 rpm. Carbon rod was used as the counter electrode and all potentials were measured by an Hg/HgO reference electrode (saturated in 1.0 M KOH) and converted to the RHE reference scale using:

$$E_{(\text{vs. RHE})} = E_{(\text{vs. Hg/HgO})} + 0.098 + (0.0591 \times \text{pH})$$

All the measured potentials in this work were corrected with 100% iR compensation. Before HER measurements, the electrolyte (1 M KOH) was bubbled with Ar gas for at least 15 min. The EIS measurement was performed over a frequency ranging from 100 kHz to 100 mHz at open circuit voltage. Before stability test, the catalyst was calcinated in an atmosphere of Ar at 200 ° C for 1 h. For plasmon-assisted electrocatalysis measurements, LEDs (Mightex Systems) were focused using a lens and positioned 10 cm in front of the reactor to illuminate the catalyst surface. The power density at the reactor front was measured as 509 mW cm^{-2} using a power meter. Prior to recording the LSV, the catalyst was illuminated for at least 5 min to reach a steady state.

Determination of Activation Energy. The activation energy (E_a) of the catalytic reaction was determined using the Arrhenius relationship:

$$k = A \exp\left(-\frac{E_a}{RT}\right), \tag{5.1}$$

where k is the reaction rate constant, A is the pre-exponential factor, R is the gas constant, and T is the absolute temperature. For electrochemical reactions, the current density (j) is proportional to the reaction rate constant (k):

$$j \propto k. \tag{5.2}$$

Thus, the temperature dependence of j can be written as

$$j = j_0 \exp\left(-\frac{E_a}{RT}\right), \tag{5.3}$$

and taking the natural logarithm yields

$$\ln(j) = \ln(j_0) - \frac{E_a}{R}\frac{1}{T}. \tag{5.4}$$

Then the Arrhenius plots were constructed by plotting ln(j) versus 1/T at fixed overpotentials (e.g., 50, 100, 150, and 200 mV). The current densities at each temperature were extracted from the corresponding LSV curves. The activation energy (E_a) was obtained from the slope of the linear fit according to

$$E_a = -R \times \text{slope}. \tag{5.5}$$

The activation energy can reflect the reaction barrier, and a lower activation energy indicates enhanced catalytic activity.

Potential of zero charge (PZC). The PZC represents the electrode potential at which the net charge density on the electrode surface is zero, meaning that the number of adsorbed anions and cations in the double layer is in equilibrium. At this potential, the interfacial electric field is minimal, and no excess electrons or holes accumulate on the surface. Therefore, a lower PZC value corresponds to a smaller work function and a higher Fermi level relative to the electrolyte, indicating that electrons are more readily available for surface reactions. In electrocatalysis, PZC is a sensitive descriptor of the electronic structure of a catalyst, helping to understand how surface charge and energy band alignment affect charge transfer dynamics at the solid-liquid interface.

DFT calculations. All the DFT calculations were carried out via the Vienna *ab initio* simulation package (VASP)[224,225] program with projector augmented wave (PAW)[226,227] method. The Perdew–Burke–Ernzerhof (PBE) generalized gradient approximation (GGA) exchange-correlation functional was chosen.[228] In addition, a 520 eV plane-wave kinetic energy cutoff was used, and a $4 \times 4 \times 1$ Gamma k-point sampling was adopted for the structure relaxation. The convergence criterion for the electronic self-consistent iteration was set to be 10^{-5} eV. A residual force threshold of 0.02 eV $Å^{-1}$ was set for geometry optimizations. The calculations were conducted on a 3×3 Ni(111) and Cu(111) surface slab model. The CuNi model was built by layering Ni(111) and Cu(111), with Ni exposed as the active sites. A 15 Å vacuum layer was modeled to simulate the surfaces studied. And the energy barriers (E_b) of H_2O dissociation were calculated by:

$$E_b = E_{TS} - E_{IS}$$

where E_{TS} and E_{IS} were the energies of the corresponding transition state (TS) and initial state (IS), respectively.

FDTD simulations. Electromagnetic simulations were performed using the commercial software lumerical finite-difference time-domain (FDTD) solution. The model consisted of

a heterostructure represented by two spheres (radius = 30 nm). A total-field scattered-field (TFSF) plane wave source was employed to illuminate the structure from the +Z direction, with a wavelength range of 500-800 nm and linear polarization along the X axis. Perfectly matched layers (PML) were applied to all simulation boundaries. A conformal mesh refinement was used in the vicinity of the metal/dielectric interfaces, with a minimum mesh size of 0.5 nm. Frequency-domain field monitors were positioned around the structure to record the near-field distribution and absorbed power, while power monitors were placed outside the structure to calculate reflection, transmission, and absorption spectra. The simulation time was set to 100 fs with an auto shut off level of 10 dec^{-5} to ensure stable field decay.

6

Electroreduction CO_2 reaction on CuAg tandem catalyst

6.1 Research background

Electrocatalytic CO_2 reduction (CO_2RR) is considered a promising method for converting CO_2 into value-added chemicals and renewable fuels, potentially contributing to the global carbon neutrality.[229] However, CO_2RR involves multiple proton-electron transfer steps and competing H_2 evolution reaction (HER), making selectivity of specific product difficult to control.[133,134] Transition metals, such as copper (Cu)[135–139] and silver (Ag),[111,230] have been extensively studied due to their unique catalytic performance for CO_2RR.[229] Ag exhibits excellent selectivity for CO via a two-electron pathway but is unable to catalyze deeper hydrocarbon products for CO_2RR.[111] In contrast, Cu is capable of producing multi-electron products such as CH_4 and C_{2+} products, although selectivities often vary due to surface structure and competing HER.[135–138]

Combining Ag and Cu as tandem catalysts offers a strategy to leverage both advantages: the Ag sites efficiently generate the *CO intermediate, while the Cu sites catalyze subsequent *CO protonation or C-C coupling steps to form hydrocarbons.[141–143] Furthermore, both Ag and Cu exhibit plasmonic responses in the visible light region,[123,124,154] potentially enabling plasmon-enhanced CO_2RR via localized surface plasmon resonance (LSPR). Plasmon excitation can be amplified by local electromagnetic field enhancement,[125] promoting the generation of hot carriers and photothermal effects.[126] Under plasmon excitation, hot electrons and photothermal heating were reported to synergistically promote CO_2RR and the generation of hydrocarbon products in CuPd,[99] CuAg nanoparticles (NPs)[231], and Cu nanocubes systems.[232] These studies highlight the important roles of hot carriers and photothermal effects in CO_2 activation and enhancing selectivity of multi-carbon products of CO_2RR.

Based on these considerations, this chapter first investigated CO_2RR on Ag nanoneedle (NND) under dark and illumination conditions. Catalytic results indicated that the plasmon excitation of Ag NND decreased the selectivity of CO from CO_2RR but instead of favoring HER. Subsequently, Cu was introduced onto the Ag NND surface via electrodeposition and e-beam evaporation to construct tandem catalysts. Under dark conditions, the AgCu NND systems catalyzed CO_2RR to CH_4 with FE more than 35%. The Ag sites catalyzed the production of *CO, while the Cu sites promoted *CO protonation to CH_4. Moreover, the morphological changes of Cu e-beam evaporated with different thicknesses on the AgNND surface were

also observed. The dependence of Cu evaporation thickness on CO_2RR performance, as well as the plasmon-enhanced CO_2RR on AgCu NND catalysts, remain to be further explored. Ultimately, this work aims to develop plasmon-enhanced electrocatalysts that can effectively convert CO_2 into valuable hydrocarbon fuels.

6.2 Results and discussion

The Ag NND samples were provided by our collaborator and subsequently used for CO_2RR under dark and illumination conditions, as well as serving as substrates for further Cu coating via electrodeposition and e-beam evaporation.[111]

Ag NND for CO_2RR: Dark vs. Light

The fabrication process of Ag NND samples from our collaborator is illustrated in Figure 6.1, which is reproduced from their previous publication.[111] Briefly, Ag was deposited onto an Al_2O_3 template by thermal evaporation, followed by chemical etching of the template in NaOH solution to obtain the Ag nanoneedle (NND) array. For clarity, Figure 6.2 presents the photograph taken during our own experiments, showing the Al_2O_3 template, the back side of the Ag NND, and the front side of the Ag NND on PDMS. The backside of the Ag NND sample exhibited a smooth metallic surface with a silver-grey color, while the front side (where the nanoneedles were exposed) appeared darker and slightly matte.

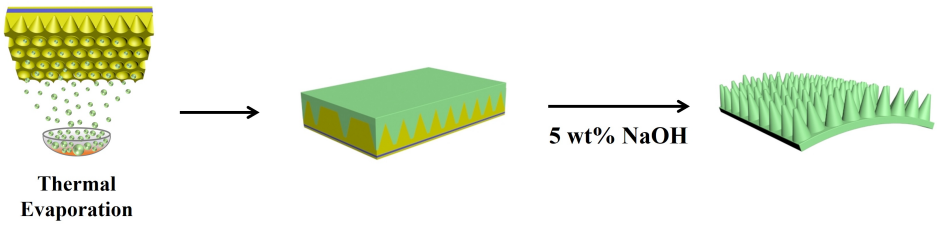

Figure 6.1: Fabrication of Ag NND. Yellow and green represent Al_2O_3 template and Ag NND, respectively. Reproduced with permission from Ref[111]

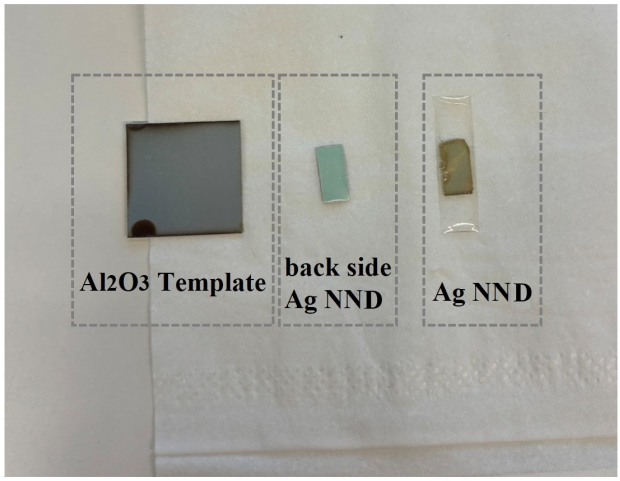

Figure 6.2: Photograph of the Ag samples. From left to right: Al_2O_3 template used for thermal evaporation, back side of Ag NND, and the front side of Ag NND on PDMS.

The surface morphology of the Ag NND sample was further characterized by scanning electron microscopy (SEM). As shown in Figure 6.3a, vertically aligned Ag NND is clearly

observed, with uniform distribution and high density. The Ag NND exhibit a well-defined conical shape, forming an ordered array over a large area. The back side of the Ag NND sample, as shown in Figure 6.3b, reveals ordered circular holes. Each circular hole corresponds to the top of an Al_2O_3 nanoneedle. The uniform size and periodic arrangement of these circular holes indicate that the Ag NND was formed by templated growth, followed by removal of the Al_2O_3 template.

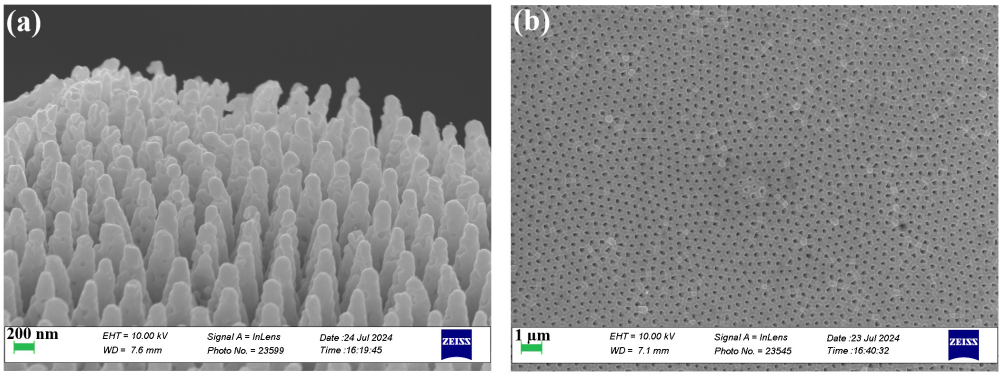

Figure 6.3: SEM images of (a) Ag NND and (b) the back side of the Ag sample.

The X-ray diffraction (XRD) pattern of the Ag NND sample (Figure 6.4a) is consistent with face-centered cubic (fcc) metallic Ag, showing characteristic reflections in the planes (111), (200), (220), and (311), with the diffraction peak (111) dominating. Such a strong (111) peak is a typical feature of evaporated Ag nanostructures. No distinct peaks corresponding to oxide species of Ag were observed, indicating high crystallinity and phase purity of the metallic Ag. Moreover, as shown in Figure 6.4b, the XPS spectrum shows that the Ag 3d spectrum exhibits two major peaks at 368.33 eV (Ag $3d_{5/2}$) and 374.33 eV (Ag $3d_{3/2}$), which are characteristic of metallic Ag. A weak shoulder attributed to the Ag^+ species can also be identified, which may be caused by mild surface oxidation when the Ag NND sample is exposed to air, indicating that the surface of the Ag NND is mainly composed of metallic Ag with only a small amount of oxidized species. The combined analysis of XRD pattern and XPS spectrum confirmed that the Ag NND sample has a crystalline fcc structure with a preferred (111) orientation, and its surface is predominantly metallic with only minor oxidation.

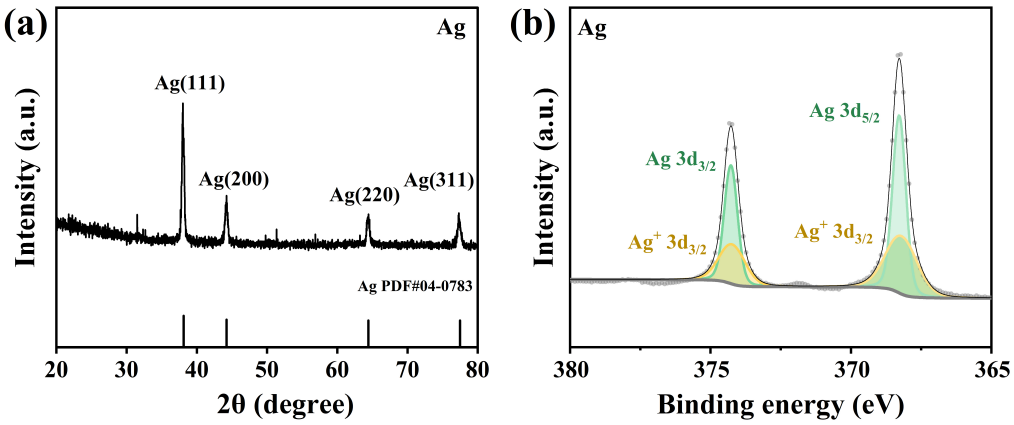

Figure 6.4: (a) XRD pattern and (b) Ag 3d XPS spectrum of the Ag NND.

The reflectance spectrum of the Ag NND electrode is shown in Figure 6.5a. A significant reflectance dip occurs near 455 nm, indicating strong light absorption near this wavelength. Therefore, Ag NND sample exhibits LSPR response in the visible light region. Based on this optical characteristic, a 405 nm LED was used to excite the LSPR effect of Ag NND for CO_2RR. As shown in Figure 6.5b, the current densities of the Ag NND electrode at all tested

potentials increased under 405 nm LED illumination compared to that in the dark condition, indicating plasmon-enhanced electrocatalytic activity. Plasmon excitation also influences product selectivity, as shown in Figure 6.5c-6.5d. Under dark conditions, CO is the primary product of CO_2RR, while H_2 is a minor competitor. Under 405 nm illumination, the Faradaic efficiency (FE) of CO decreases, while the FE of CO_2 increases at all tested potentials. This trend suggests that plasmon excitation of the Ag NND favors HER over CO_2RR, likely due to the faster surface charge transfer to H_2 evolution. Overall, these results indicate that the Ag NND electrode exhibits distinct plasmon-enhanced electrocatalytic performance, while light illumination favors HER rather than CO_2RR.

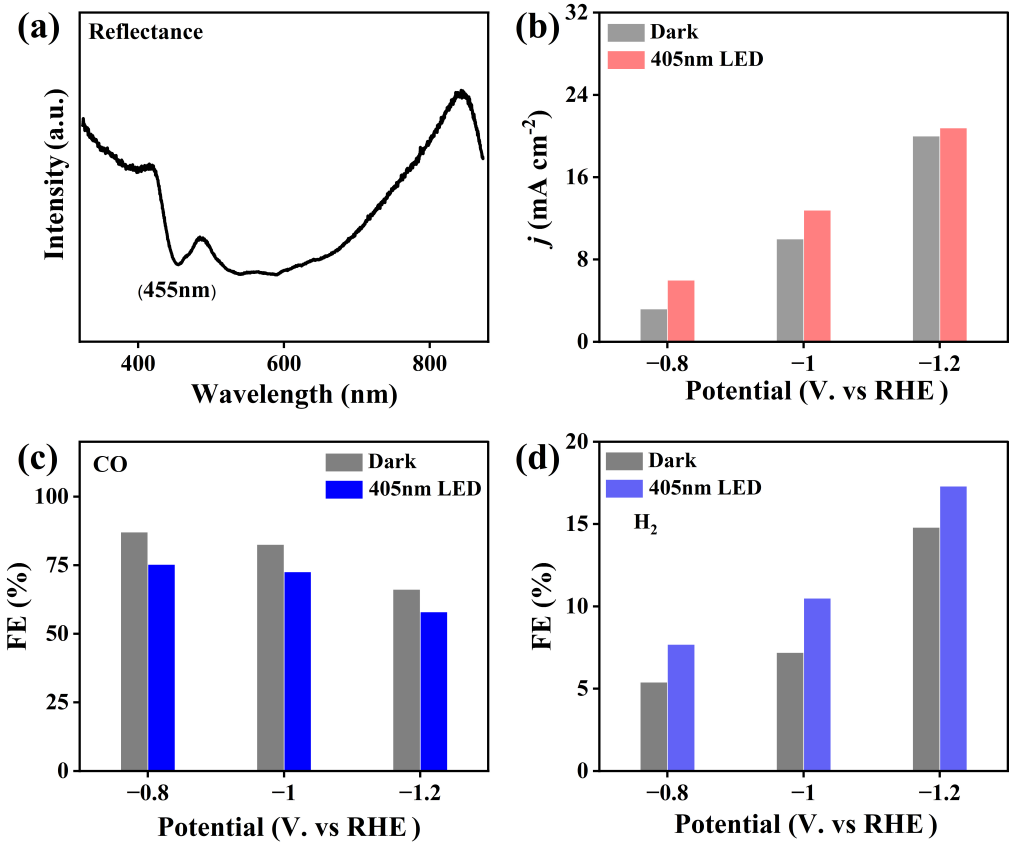

Figure 6.5: Photoelectrocatalytic performance of Ag nanoneedle. (a) Reflectance spectrum of Ag NND. (b) The current density, and Faradaic efficiencies of (c) CO and (d) H_2 on Ag NND electrode at different potentials, under dark and 405 nm LED illumination.

Overall, the Ag NND fabricated from the Al_2O_3 template exhibits a highly ordered nanoneedle morphology. Its LSPR effect enhances the overall current densities of CO_2RR under 405 nm LED illumination. However, light illumination shifts the product selectivity toward H_2 rather than CO generation, indicating that plasmon excitation preferentially promotes the HER. To further regulate the selectivity of CO_2RR toward hydrocarbon products such as CH_4 and C_{2+} species, Cu was subsequently introduced onto the Ag NND surface via electrodeposition and e-beam evaporation, considering both its plasmonic response in the visible region and its superior electrocatalytic activity for CH_4 and C_{2+} species products.

Cu on Ag NND via Electrodeposition

To further tailor the catalytic performance of Ag NND to CH_4 or C_{2+} for CO_2RR, Cu was introduced onto the Ag NND via electrodeposition. Based on the method of collaborators,[111] Cu-deposited Ag NND electrodes were prepared by electrodeposition in a 0.5 mM $CuSO_4{\cdot}5H_2O$ electrolyte at 0 V_{RHE} for 30 s (AgCu-30s) and 180 s (AgCu-180s), respectively. As shown in

Figure 6.6, after 30 s of electrodeposition, the AgCu-30s sample exhibited the typical brick-red color of Cu. The nail polish was used to control the CO_2RR area to 0.5 cm * 0.5 cm.

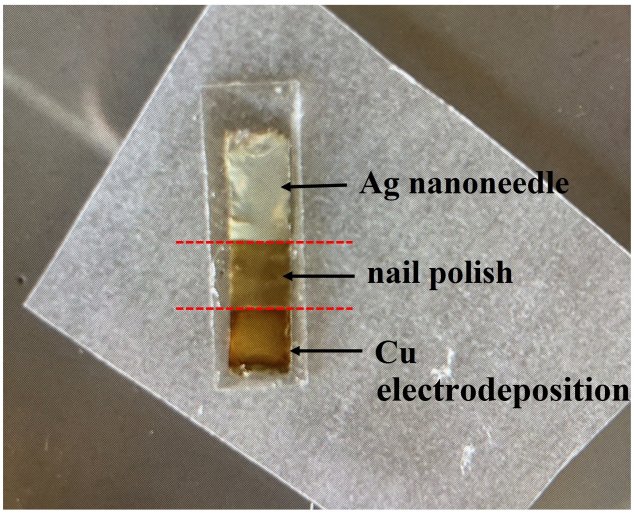

Figure 6.6: Photograph of Cu electrdeposited on Ag NND with 0 V_{RHE}, 30 s.

The surface morphology of AgCu-30s and AgCu-180s was characterized by SEM, as shown in Figure 6.7a-6.7b. The CuAg-30s and CuAg-180s samples exhibited rougher surfaces, compared to Ag NND. The SEM images and brick-red color of the samples, combined with the performance of the CuAg-30s and CuAg-180s electrodes for CH_4 generation from CO_2RR under dark conditions (Figure 6.7c-6.7d), demonstrate that Cu was successfully deposited on the Ag NND. Under dark conditions, the main products of AgCu-30s were CH_4 and H_2, with FE of 38.4% and 35.2%, respectively. Extending the deposition time to 180 s (AgCu-180s) resulted in a slight decrease in FE of CH_4 (36.6%) and a significant increase in FE of H_2 (54.4%).

Compared to AgCu-30s, the surface of AgCu-180s was covered with more Cu. Ag needle sites favor *CO formation, while Cu sites are more active for both *CO protonation and the HER. With higher Cu coverage, the proportion of exposed Ag needle sites decreased, making HER kinetically more favorable than CO_2RR. Furthermore, excess Cu may also alter the local electric field on the tip of the Ag needle, further promoting the HER.[111] Therefore, precisely controlling the Cu coverage on Ag NND is crucial for enhancing CO_2RR and suppressing the competing HER.

5nm Cu on Ag NDD via e-beam Evaporation

To achieve more uniform and precisely controlled Cu coverage, a 5 nm Cu layer was further deposited onto the Ag NND surface by e-beam evaporation. This approach allows a uniform Cu coating across the entire Ag NDD without significantly altering needle morphology. The obtained AgCu catalysts are expected to provide a balanced surface composition, thereby leveraging the high efficiency of Ag sites for *CO formation and the high efficiency of Cu sites for *CO protonation or coupling, thereby promoting the generation of CH_4 and C_{2+} products for CO_2RR.

Figure 6.8 illustrates a Cu-deposited Ag NND sample via e-beam evaporation and its corresponding optical appearance. As shown in Figure 6.8b, a thin layer of Cu with thickness of 5 nm was deposited on the Ag NND via e-beam evaporation, resulting in a slightly darker color. SEM images in Figure 6.9 reveal that the Ag tips are intact, with small metallic particles on the tips and the body.

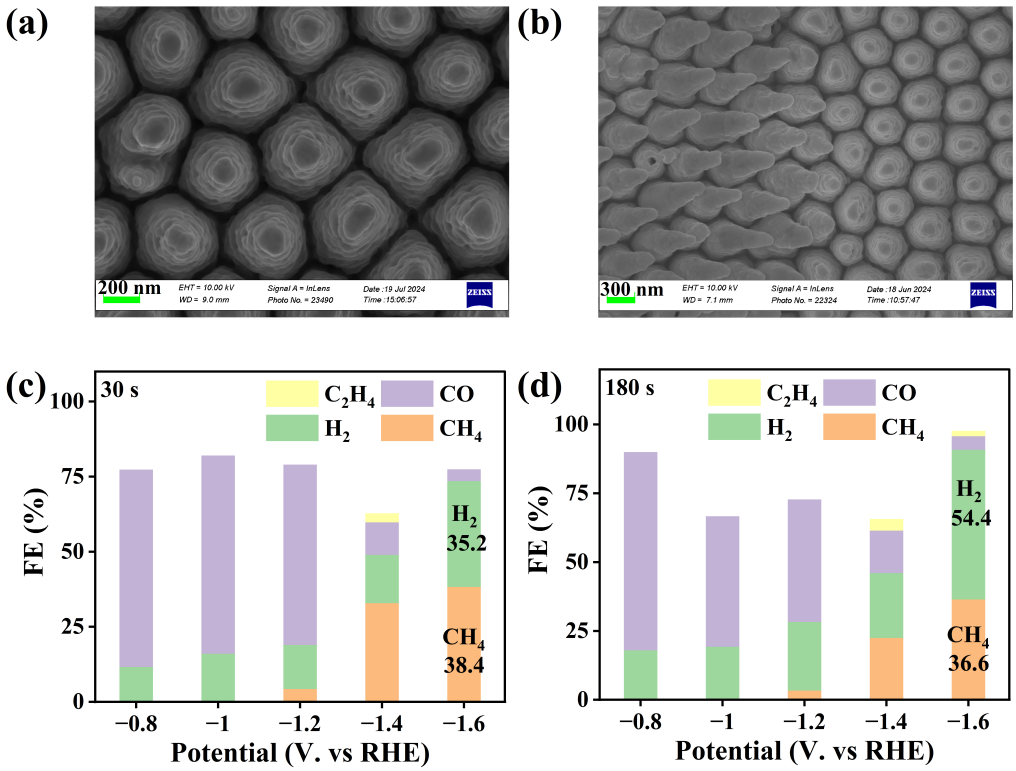

Figure 6.7: Ag NND with Cu electrodeposition. SEM images of (a) AgCu-30s (Cu electrdeposited on Ag NND with with 0 V_{RHE}, 30 s) and (b) AgCu-180s (Cu electrdeposited on Ag NND with with 0 V_{RHE}, 180 s). Faradaic efficiencies of gas products on (c) AgCu-30s and (d) AgCu-180s electrodes at different potentials under dark condition.

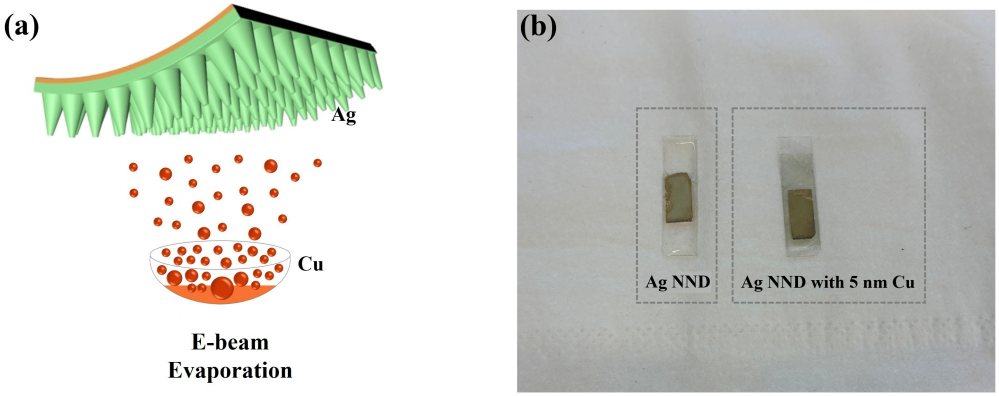

Figure 6.8: E-beam evaporation of 5 nm Cu on Ag NND. (a) Fabrication of Ag NND with Cu by e-beam evaporation. Reproduced with permission from Ref[111]. (b) Photograph of Ag NDD and AgCu-5nm (Ag NND after 5 nm Cu depostion by e-beam evaporation).

The surface chemical states of the AgCu-5nm sample were further analyzed by XPS spectra, as shown in Figure 6.10. In the Ag 3d spectrum (Figure 6.10a), two main peaks are observed at 368.51 eV (Ag $3d_{5/2}$) and 374.51 eV (Ag $3d_{3/2}$), which are characteristic of metallic Ag. Compared with the Ag NND sample (368.33 and 374.33 eV), there is a slight positive shift of 0.18 eV, which can be attributed to interfacial electronic interactions between Ag and Cu, or mild surface oxidation. The Ag 3d spectrum of AgCu-5nm shows Ag sites remain predominantly metallic with only a small amount of surface Ag^+ species. The Cu 2p spectrum (Figure 6.10b) displays two distinct peaks at 932.81 eV (Cu $2p_{3/2}$) and 952.61 eV (Cu $2p_{1/2}$), typical of metallic Cu. Only weak signals of Cu^+ and Cu^{2+} are detected, indicating that the Cu layer mainly existed in metallic state, with minimal oxidation state likely due to exposure to air. The XPS analysis verifies that the e-beam evaporated AgCu-5nm sample mainly consists

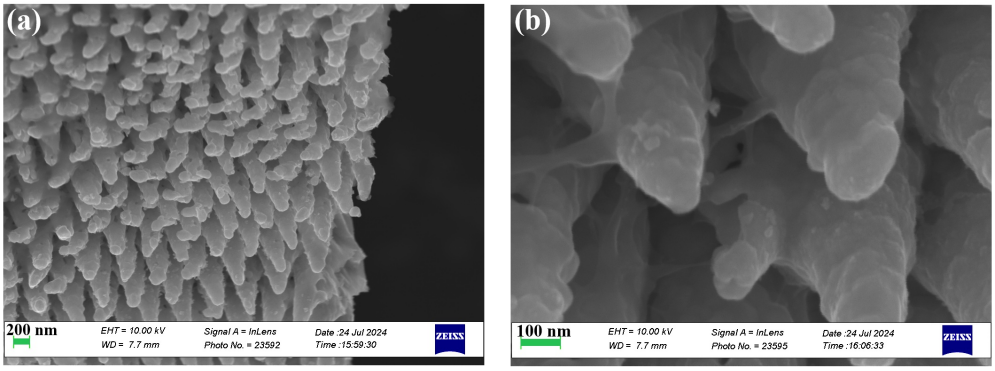

Figure 6.9: SEM images of AgCu-5nm.

of metallic Ag and Cu on its surface, suggesting suitable for serving as tandem catalyst for CO_2RR.

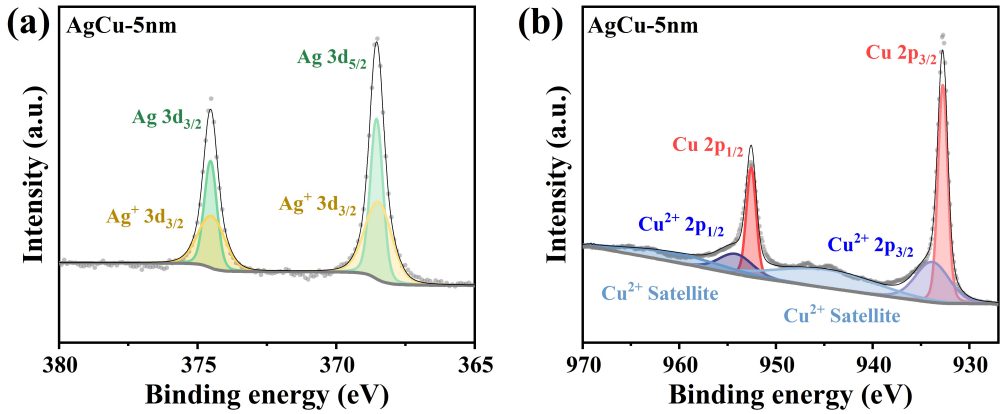

Figure 6.10: XPS spectra of AgCu-5 nm: (a) Ag 3d and (b) Cu 2p regions.

The electrocatalytic performance of the AgCu-5nm electrode for CO_2RR under dark conditions is shown in Figure 6.11a. In the potential range of -0.8 V_{RHE} to -1.2 V_{RHE}, CO gas was the main product, and CH_4 started to generate at -1.2 V_{RHE}. When the potential goes to -1.6 V_{RHE}, CH_4 and H_2 were the main products, with minor formation of CO and C_2H_4, where the FE of CH_4 reached the highest of 35.2% and the FE of H_2 reached 30.3%. As the potential further increases to -1.6 V_{RHE}, the FE of CH_4 decreased and H_2 increased. The production of CH_4 indicates that the Ag sites facilitated the generation of *CO, while the Cu sites around the Ag sites were catalytically active for the protonation of *CO. Therefore, the tandem configuration of AgCu-5nm effectively promoted multi-step CO_2RR toward CH_4. SEM image of AgCu-5nm electrode after the reaction in Figure 6.11b shows that the sample remained nanoneedle morphology. However, the metallic nanoparticles on the body of needle disappeared, suggesting that partial dissolution of Cu during the reaction, which is commonly observed.[233]

Cu layers with different Thicknesses on Ag NND via e-beam Evaporation

To further increase the number of active sites for *CO protonation or C–C coupling, Cu layers with thicknesses of 10 nm and 50 nm (denoted as AgCu-10nm and AgCu-50nm, respectively) were deposited on the Ag NND surface via e-beam evaporation. As shown in Figure ??a, when the deposition thickness of Cu increased from 5 nm to 10 nm, the color of the AgCu-10nm sample became a litter bit darker. When the thickness of Cu reached 50 nm, the AgCu-50nm sample exhibited a color of deep brick red. The change of color reflected the increased Cu coverage on the Ag NND surface.

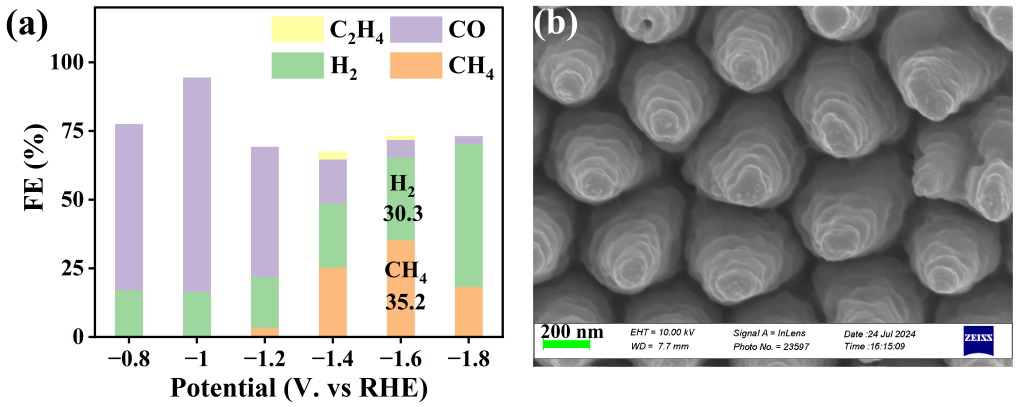

Figure 6.11: (a) Faradaic efficiencies of gas products on AgCu-5nm electrode at different potentials under dark condition. (b) SEM image of AgCu-5nm after reaction.

The XPS spectra analyzed the surface chemical states of the AgCu-10nm sample. As shown in Figure 6.12a, the Ag 3d spectrum showed two main peaks at 368.61 eV (Ag $3d_{5/2}$) and 374.61 eV (Ag $3d_{3/2}$), which are characteristic of metallic Ag. Compared with Ag NND sample (368.33 and 374.33 eV), the AgCu-10nm sample exhibited a positive shift of 0.28 eV, which is slightly larger than the 0.18 eV shift observed for AgCu-5nm. This indicates AgCu-10nm sample exhibited a stronger interfacial electronic interaction between Ag and the Cu overlayer than the AgCu-5nm sample. The Cu 2p spectrum displayed two main peaks at 932.71 eV (Cu $2p_{3/2}$) and 952.61 eV (Cu $2p_{1/2}$), typical of metallic Cu. Weak satellite features suggested that Cu^{2+} species are negligible, which were likely formed upon exposure to air. The XPS results indicated that the increased Cu thickness strengthened the interfacial electronic interactions of Ag and Cu, while the AgCu-10nm sample mainly maintained metallic state.

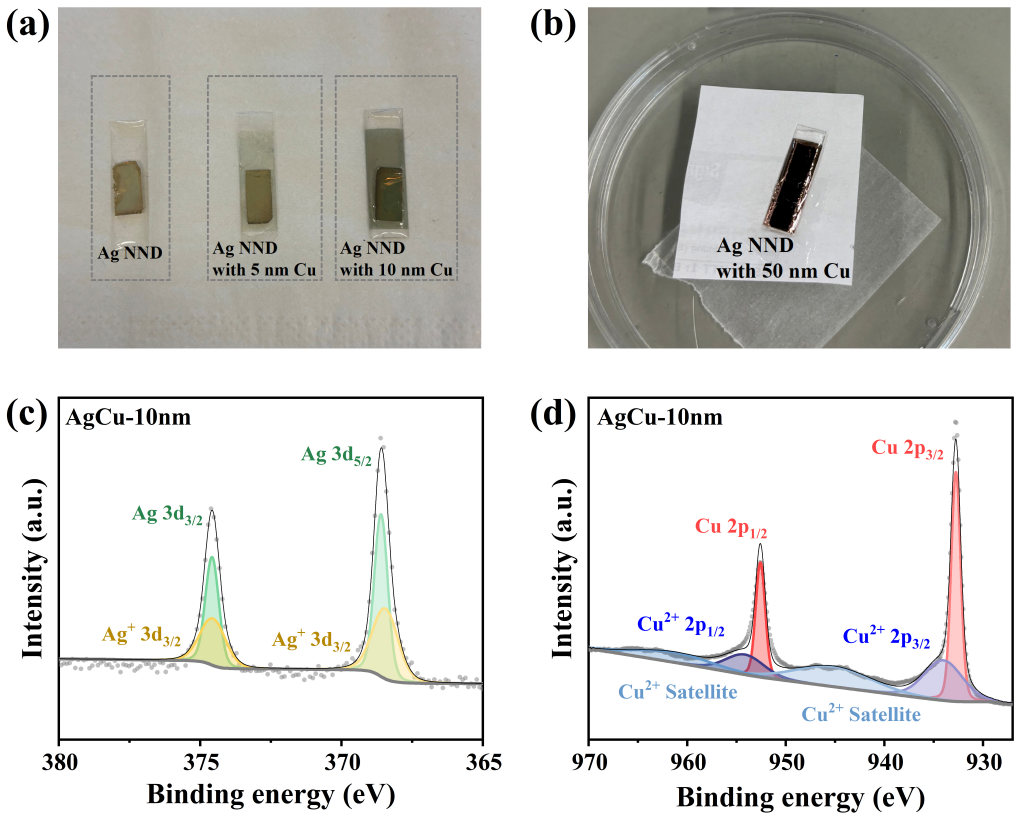

Figure 6.12: Cu Layers of different thicknesses on Ag NND. (a, b) Photograph of Ag NDD, AgCu-5nm, AgCu-10nm and AgCu-50nm (Ag NND after 5 nm, 10 nm and 50 nm Cu depostion by e-beam evaporation. XPS spectra of AgCu-10 nm: (c) Ag 3d and (d) Cu 2p regions.

The SEM images of the AgCu-10nm sample, as shown in Figure 6.13 show that the vertically aligned nanoneedle structure was well preserved after the e-beam evaporation of a 10 nm Cu layer on Ag NND substrate. Compared with the AgCu-5nm sample, the surface of AgCu-10nm sample became noticeably rougher, which seems to be covered with granular Cu clusters, confirming thicker layer of Cu and increased Cu sites on the needle surface. The enhanced roughness and granular morphology enlarged the electrochemically active surface area and provided more Cu sites for *CO protonation to CH_4 or C-C coupling to C_{2+} products during CO_2RR. The SEM images of the AgCu-50nm sample, as shown in Figure 6.14, even with a Cu thickness of 50 nm, the vertically aligned nanoneedle morphology was still preserved. Compared with the AgCu-10nm sample, the Cu coating of the AgCu-50nm sample was thicker and more continuous, like a dense and uniform Cu cluster layer, which shielded the sharp needle to some extent.

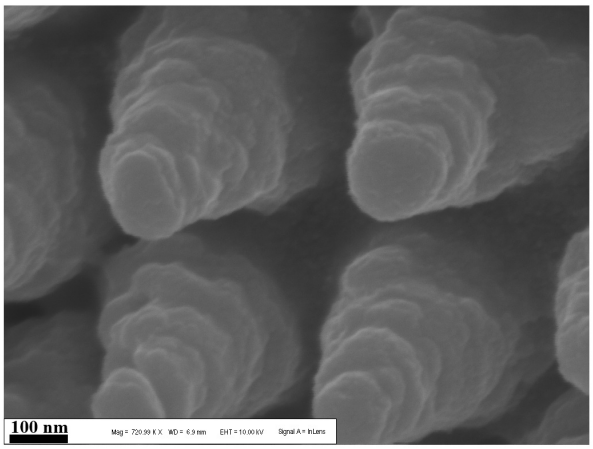

Figure 6.13: SEM images of AgCu-10nm.

Although high Cu coverage can provide more active sites for *CO protonation and C-C coupling, it also reduced the exposed area of Ag, which resulted in unable to take advantage of the Ag needle sites to promote CO_2 activation and *CO generation. Therefore, controlling the Cu thickness is crucial to balance the exposure of Ag and Cu active sites and maintain efficient tandem catalysis. When the Cu and Ag sites are maintained at a suitable ratio, allowing as much *CO as possible to be generated on the Ag site, and then *CO migrates to the adjacent Cu site for protonation or coupling, more hydrocarbons will be produced. To further validate the optimal Cu thickness for achieving high activity and selectivity toward specific CO_2RR products, more comprehensive electrocatalytic tests are required.

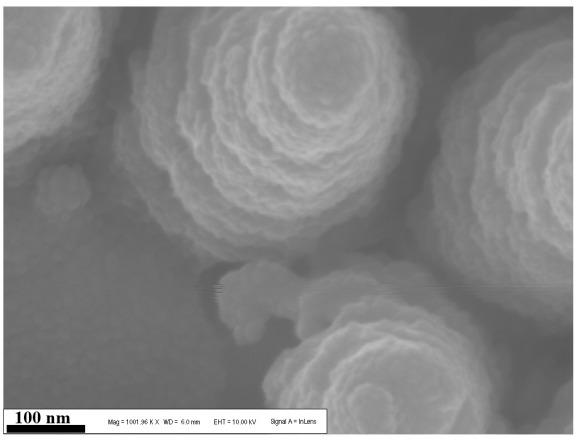

Figure 6.14: SEM images of AgCu-50nm.

Further Investigation for plasmon-enhanced CO_2RR on AgCu NND

To further establish the correlation between optimal Cu thickness, plasmon excitation, and selectivities of different products, future works will first determine the optimal Cu thickness for different hydrocarbon products of CO_2RR under dark conditions. After identifying the optimized parameters of Cu evaporation, the effective excitation wavelength of the AgCu NND catalysts will be determined by reflectance spectrum.

Based on the optimized Cu thickness and efficient excitation wavelength, plasmon-enhanced CO_2RR experiments will be performed to verify whether plasmon excitation of Cu can significantly enhance the protonation or coupling of *CO intermediates. The enhancement in the production yields of CH_4 and C_{2+} products under illumination will be quantitatively analyzed. Finally, the mechanism of hot carriers and photothermal heating in tuning product selectivity will be elucidated.

6.3 Summary and outlook

In summary, the AgCu NND tandem catalysts were developed in this work to regulate the products of CO_2RR towards hydrocarbons (CH_4 and C_{2+} products). Based on the bare Ag NND catalyst exhibiting high CO selectivity under dark conditions, Cu was introduced onto Ag NND substrate to serve as active sites for *CO protonation or coupling. With moderate Cu coverage (electrodeposition at 0 V_{RHE} for 30 s, and 5 nm thickness of Cu by e-beam evaporation), CH_4 was generated, which FE was more than 35%, confirming that Cu sites actively facilitated the protonation of *CO intermediates generated at Ag sites. Furthermore, increasing the Cu thickness to 10 nm and 50 nm by e-beam evaporation can further improve the surface roughness and the density of Cu sites of AgCu NND samples, maintaining the morphology of nanoneedle array as well as providing more opportunities for *CO protonation or coupling.

Nevertheless, the optimal Cu coverage must be carefully balanced by tuning the thickness of Cu to maintain the tandem catalytic synergy between Ag and Cu. Based on these findings, future studies will focus on optimizing the Cu layer thickness and selectively exciting the LSPR of Cu to further enhance multi-electron pathways. Plasmon-enhanced CO_2RR experiments will be conducted, while different kinds of theoratical and experimental methods will be used to reveal the contribution of plasmonic hot carriers and photothermal effects to the improved CH_4 and C_{2+} products.

Overall, this work highlighted the importance of balancing the different active sites of tandem catalysts and demonstrated a promising strategy for plasmon-enhanced electrocatalysts that effectively convert CO_2 into energy-rich hydrocarbon fuels.

6.4 Method

Characterizations.

XRD data was collected by using an X'Pert PRO PANalytical instrument (Ni-filtered Cu Kα radiation source) from 30° to 80° with a slow scanning step 0.125° per min. X-ray photoelectron spectroscopy (XPS) was measured by Thermo Scientific Nexsa G2 surface

analysis. The reflection spectrum were tested by a WiTec setup. The SEM images were from ZEISS Ultra Plus Raster Elektronen Mikroskop.

Electrochemical measurements.

1. CO_2RR (plasmon-assisted) electrocatalysis measurement.

The CO_2RR measurements were carried out in a quartz H-type cell with a potentiostat (Biologic, SP-300). For plasmon-assisted electrocatalysis measurement, the 405 nm LED (Mightex Systems) was first focused by a lens, then put front of the reactor with a distance of 10 cm. The Ag NND or AgCu NND on PDMS were applied as the working electrode. A platinum plate and Ag/AgCl electrode were used as counter electrode and reference electrode, respectively. All the applied potentials (vs. Ag/AgCl) were converted to potentials (vs. RHE) by formula of $E_{RHE} = E_{Ag/AgCl} + 0.197\ V + 0.0592 * pH$. Before running the measurement, the electrolyte 0.5 M $KHCO_3$ was saturated with CO_2 by bubbling CO_2 gas (99.999%) for 20 minutes. The constant purged CO_2 was controlled with a rate of 20 sccm.

2. Products quantification.

The gas-phase products from cathodic were collected by gas chromatograph (PerkinElmer Clarus 590. High-purity N2 (99.999%) was used as the carrier gas. The gas products from the cell were injected online every 30 minutes into the GC. The FE of gas and liquid products was obtained by the equation of Faraday efficiency.

7
Conclusion and Outlook

This thesis establishes a coherent framework for using plasmonic excitation to regulate electrocatalytic reactions over Cu-based bimetallic and tandem architectures. Across CuPd, CuNi, and CuAg platforms, the work demonstrates that localized surface plasmon resonance (LSPR) can accelerate rate-limiting steps and change product selectivity by providing hot carriers injection and photothermal heating.

For carbon dioxide electroreduction reaction (CO_2RR), CuPd tandem catalysts show that plasmonic excitation promotes *CO (an adsorbed carbon monoxide on the catalyst surface) formation on CuPd interface and facilitates its migration to Cu sites, where higher *CO coverage enables more efficient C-C coupling toward ethylene. This clarifies the functional division in CuPd system and demonstrates that optical activation can shift reaction pathways toward higher-value hydrocarbon formation.

For alkaline hydrogen evolution reaction (HER), the developed CuNi catalyst surpasses the performance of commercial Pt under illumination. Hot electrons generated in Cu domains are effectively injected into Ni active centers, improving both water dissociation and hydrogen evolution kinetics. Photothermal heating further enhances interfacial mass transport, enabling sustained catalytic performance without noble metals.

For CuAg nanoneedle system, Ag nanoneedle sites efficiently catalyze *CO intermediates formation while adjacent Cu domains drive *CO hydrogenation to methane. By tuning the Cu coverage to balance exposed Ag sites for *CO formation and exposed Cu sites for *CO high hydrogenation or coupling, high selectivity toward methane or multi-carbon products may be achieved. Moreover, CuAg nanoneedle system is potential to serve as a plasmonic platform to improve the selectivity of specific product of CO_2RR.

Plasmon-enhanced electrocatalysis offers several promising directions for further development. Optimization of catalyst structure to tune the LSPR energies, near field enhancement, and hot carriers distribution, will allow for more precise control of product selectivity. Meanwhile, emerging in situ and nanoscale characterization techniques are expected to provide deeper insights into hot carrier dynamics, interfacial photothermal heating, and light-induced structural evolution. Translating these findings into practical applications, such as flow cells and membrane electrode assemblies, will facilitate operation under industrially relevant current densities and illumination conditions. Furthermore, extending the strategies to complex systems, for example, higher-value multi-carbon oxygenate synthesis or integrated CO_2 fuel production chains, will further illustrate the universality and broad applicability of plasmon-enhanced approaches in energy conversion and chemical manufacturing.

In summary, this thesis advances both the understanding and practical use of plasmon-enhanced CO_2RR and HER by integrating rational catalyst nanoengineering, comprehensive operando mechanistic investigation, and theoretical modeling. These results demonstrate a generalizable approach for plasmon-enhanced electrocatalysis, which combines the light-absorbing antenna and electrocatalytic active centers at the nanoscale. The design ideas of the catalyst in this thesis, as well as the theoretical and experimental methods used to reveal the LSPR effect, provide a theoretical basis and structural design principles for the development of the next generation of highly active, highly selective and highly stable plasmonic electrocatalysts, and also lay an important foundation for clean energy conversion technology driven by the synergy of light and electricity.

A
Appendix

A.1 XRD rulers

Table A.1: Table A.X: XRD ruler of Pd in the FCC phase for Cu Kα radiation.

2-Theta (°)	d (Å)	I(f)	(h k l)	Θ (°)	$\frac{1}{2d}$	$\frac{2\pi}{d}$	n^2
40.114	2.2460	100.0	(1 1 1)	20.057	0.2226	2.7975	3
46.661	1.9450	42.0	(2 0 0)	23.330	0.2571	3.2304	4
68.083	1.3760	25.0	(2 2 0)	34.042	0.3634	4.5663	8
82.094	1.1730	24.0	(3 1 1)	41.047	0.4263	5.3565	11
86.596	1.1232	8.0	(2 2 2)	43.298	0.4452	5.5940	12
104.788	0.9723	3.0	(4 0 0)	52.394	0.5142	6.4622	16
119.345	0.8924	13.0	(3 3 1)	59.673	0.5603	7.0408	19
124.672	0.8697	11.0	(4 2 0)	62.336	0.5749	7.2245	20

Table A.2: Table A.X: XRD ruler of Ni in the FCC phase for Cu Kα radiation.

2-Theta (°)	d (Å)	I(f)	(h k l)	Θ (°)	$\frac{1}{2d}$	$\frac{2\pi}{d}$	n^2
44.347	2.0409	100.0	(1 1 1)	22.174	0.2450	3.0786	3
51.673	1.7675	41.5	(2 0 0)	25.836	0.2829	3.5548	4
76.095	1.2498	16.1	(2 2 0)	38.048	0.4001	5.0273	8
92.555	1.0658	14.4	(3 1 1)	46.278	0.4691	5.8951	11
98.021	1.0205	3.9	(2 2 2)	49.010	0.4900	6.1571	12
121.291	0.8838	1.7	(4 0 0)	60.646	0.5658	7.1097	16
143.540	0.8110	5.3	(3 3 1)	71.770	0.6165	7.7476	19

Table A.3: Table A.X: XRD ruler of Cu in the FCC phase for Cu Kα radiation.

2-Theta (°)	d (Å)	I(f)	(h k l)	Θ (°)	$\frac{1}{2d}$	$\frac{2\pi}{d}$	n^2
43.341	2.0860	100.0	(1 1 1)	21.670	0.2397	3.0121	3
50.478	1.8065	42.7	(2 0 0)	25.239	0.2768	3.4781	4
74.172	1.2774	17.1	(2 2 0)	37.086	0.3914	4.9188	8

Table A.4: Table A.X: XRD ruler of Graphite-2H for Cu Kα radiation.

2-Theta (°)	**d** (Å)	**I(f)**	**(h k l)**	**Θ (°)**	$\frac{\mathbf{1}}{\mathbf{2d}}$	$\frac{\mathbf{2\pi}}{\mathbf{d}}$	$\mathbf{n^2}$
26.381	3.3756	100.0	(0 0 2)	13.190	0.1481	1.8613	
42.221	2.1386	2.0	(1 0 0)	21.111	0.2338	2.9379	
44.391	2.0390	6.0	(1 0 1)	22.196	0.2452	3.0815	
50.452	1.8074	1.0	(1 0 2)	25.226	0.2766	3.4764	
54.542	1.6811	4.0	(0 0 4)	27.271	0.2974	3.7375	
59.692	1.5478	1.0	(1 0 3)	29.846	0.3230	4.0595	
77.243	1.2341	3.0	(1 1 0)	38.622	0.4052	5.0914	
83.183	1.1604	3.0	(1 1 2)	41.592	0.4309	5.4148	
86.823	1.1208	1.0	(0 0 6)	43.412	0.4461	5.6058	
93.594	1.0567	1.0	(2 0 1)	46.797	0.4732	5.9459	

Table A.5: Table A.X: XRD ruler of Ag in the FCC phase for Cu Kα radiation.

2-Theta (°)	**d** (Å)	**I(f)**	**(h k l)**	**Θ (°)**	$\frac{\mathbf{1}}{\mathbf{2d}}$	$\frac{\mathbf{2\pi}}{\mathbf{d}}$	$\mathbf{n^2}$
38.116	2.3590	100.0	(1 1 1)	19.058	0.2120	2.6635	3
44.277	2.0440	40.0	(2 0 0)	22.139	0.2446	3.0740	4
64.426	1.4450	25.0	(2 2 0)	32.213	0.3460	4.3482	8
77.472	1.2310	26.0	(3 1 1)	38.736	0.4062	5.1041	11
81.536	1.1796	12.0	(2 2 2)	40.768	0.4239	5.3265	12
97.888	1.0215	4.0	(4 0 0)	48.944	0.4895	6.1509	16
110.497	0.9375	15.0	(3 3 1)	55.248	0.5333	6.7021	19
114.924	0.9137	12.0	(4 2 0)	57.462	0.5472	6.8766	20
134.882	0.8341	13.0	(4 2 2)	67.441	0.5994	7.5329	24

References

[1] Stefan Alexander Maier. *Plasmonics: Fundamentals and Applications*. New York: Springer, 2007. ISBN: 978-0-387-37825-1 (cited on pages 5, 8, 9).

[2] Gustav Mie. "Beiträge zur Optik trüber Medien, speziell kolloidaler Metallösungen". In: *Annalen der Physik* 330.3 (1908), pp. 377–445 (cited on page 10).

[3] Jingyi Han et al. "Advances and challenges in the electrochemical reduction of carbon dioxide". In: *Chemical Science* 15 (2024), pp. 7870–7907 (cited on page 11).

[4] Jianjun Shi et al. "Recent progress and perspective of electrocatalysts for the hydrogen evolution reaction". In: *Catalysis Science & Technology* 15.7 (2025), pp. 2104–2131 (cited on page 11).

[5] Zhu Deng et al. "Global carbon emissions and decarbonization in 2024". In: *Nature Reviews Earth & Environment* 6 (2025), pp. 231–233 (cited on page 11).

[6] Tsimafei Kazlou, Aleh Cherp, and Jessica Jewell. "Feasible deployment of carbon capture and storage and the requirements of climate targets". In: *Nature Climate Change* 14.10 (2024), pp. 1047–1055 (cited on page 11).

[7] Hongtao Dang et al. "Research Status, Challenges, and Future Prospects of Carbon Dioxide Reduction Technology". In: *Accounts of Materials Research* 38.6 (2024), pp. 4836–4880 (cited on page 11).

[8] Remko J. Detz et al. "Electrochemical CO_2 conversion technologies: state-of-the-art and future perspectives". In: *Sustainable Energy & Fuels* 7.23 (2023), pp. 5445–5472 (cited on page 11).

[9] Yoshio Hori et al. "Production of Methane and Ethylene in Electrochemical Reduction of Carbon Dioxide at Copper Electrode in Aqueous Hydrogencarbonate Solution". In: *Chemistry Letters* 15.6 (1986), pp. 897–898 (cited on page 11).

[10] Aneelman Brar et al. "Challenges in Product Selectivity for Electrocatalytic Reduction of Amine-Captured CO_2: Implications for Reactive Carbon Capture". In: *ACS Omega* 10.21 (2025), pp. 21980–21984 (cited on page 11).

[11] Ping Shao et al. "Metal-organic frameworks for electrochemical reduction of carbon dioxide: The role of metal centers". In: *Journal of Energy Chemistry* 40 (2020), pp. 156–170 (cited on page 12).

[12] Qiang Wang et al. "Recent advances in copper-based catalysts for electrocatalytic CO_2 reduction toward multi-carbon products". In: *Nano Research Energy* 3.9 (2024), e9120020 (cited on page 12).

[13] Claudio Ampelli et al. "Electrode and cell design for CO_2 reduction: A viewpoint". In: *Catalysis Today* 421 (2023), p. 114217 (cited on page 12).

[14] Chao Zhan et al. "Key intermediates and Cu active sites for CO_2 electroreduction to ethylene and ethanol". In: *Nature Energy* 9 (2024), pp. 1485–1496 (cited on page 12).

[15] Jiabao Huang et al. "Recent Progress on Copper-Based Bimetallic Heterojunction Catalysts for CO_2 Electrocatalysis: Unlocking the Mystery of Product Selectivity". In: *Advanced Science* 11 (2024), p. 2309865 (cited on pages 12, 13).

[16] Chao Zhan et al. "Key intermediates and Cu active sites for CO_2 electroreduction to ethylene and ethanol". In: *Nature Energy* 9 (2024), pp. 1485–1496 (cited on page 12).

[17] Jingyi Han et al. "Advances and challenges in the electrochemical reduction of carbon dioxide". In: *Chemical Science* 15 (2024), pp. 7870–7907 (cited on page 13).

[18] Yuhou Pei, Heng Zhong, and Fangming Jin. "A brief review of electrocatalytic reduction of CO_2—Materials, reaction conditions, and devices". In: *Energy Science & Engineering* 9.8 (2021), pp. 956–981 (cited on page 13).

[19] Alexander Bagger et al. "Electrochemical CO_2 Reduction: A Classification Problem". In: *ChemPhysChem* 18.22 (2017), pp. 3266–3273 (cited on page 13).

[20] Grazia Leonzio, Anna Hankin, and Nilay Shah. "CO_2 electrochemical reduction: A state-of-the-art review with economic and environmental analyses". In: *Chemical Engineering Research and Design* 208 (2024), pp. 934–955 (cited on page 13).

[21] Stephanie Nitopi et al. "Progress and Perspectives of Electrochemical CO_2 Reduction on Copper in Aqueous Electrolyte". In: *Chemical Reviews* 119.12 (2019), pp. 7610–7672 (cited on page 13).

[22] Nivedita Sikdar. "Electrochemical CO_2 Reduction Reaction: Comprehensive Strategic Approaches to Catalyst Design for Selective Liquid Products Formation". In: *Chemistry – A European Journal* 30 (2024), e202402477 (cited on page 13).

[23] Yichen Sun et al. "Non-noble metal single atom-based catalysts for electrochemical reduction of CO_2: Synthesis approaches and performance evaluation". In: *DeCarbon* 2 (2023), p. 100018 (cited on page 13).

[24] Ke Ma, Shiyu Zhang, and Weixuan Nie. "Heterogeneous Electrocatalytic CO_2 Reduction by Supported Molecular Catalysts Well Dispersed on Electrode Surface". In: *ChemElectroChem* 12.13 (2025), e202500074 (cited on page 13).

[25] Biaobiao Zhang and Licheng Sun. "Artificial photosynthesis: opportunities and challenges of molecular catalysts". In: *Chemical Society Reviews* 48.7 (2019), pp. 2216–2264 (cited on page 13).

[26] Zhi-Wen Yang et al. "Molecular Engineering of Metal Complexes for Electrocatalytic Carbon Dioxide Reduction: From Adjustment of Intrinsic Activity to Molecular Immobilization". In: *Angewandte Chemie International Edition* 61.44 (2022), e202205301 (cited on page 14).

[27] Eleanor Stewart-Jones and Daniel A. Kurtz. "An atomistic picture is worth a thousand words: New details on supported molecular catalysts". In: *Matter* 5.8 (2022), pp. 2553–2555 (cited on page 14).

[28] Kee Chun Poon et al. "A review on recent advances in the electrochemical reduction of CO_2 to CO with nano-electrocatalysts". In: *RSC Advances* 12 (2022), pp. 22703–22721 (cited on page 14).

[29] Wei Chen et al. "Electrocatalytic CO_2 Reduction over Bimetallic Bi-Based Catalysts: A Review". In: *CCS Chemistry* 5 (2023), pp. 544–567 (cited on page 14).

[30] Xiaolong Zhang et al. "Electrocatalytic carbon dioxide reduction: from fundamental principles to catalyst design". In: *Materials Today Advances* 7 (2020), p. 100074 (cited on page 14).

[31] Luwei Peng et al. "Research Advances in Electrocatalysts, Electrolytes, Reactors and Membranes for the Electrocatalytic Carbon Dioxide Reduction Reaction". In: *Acta Physico-Chimica Sinica* 39.12 (2023), p. 230203 (cited on page 14).

[32] Hassina Tabassum et al. "Surface engineering of Cu catalysts for electrochemical reduction of CO_2 to value-added multi-carbon products". In: *Chem Catalysis* 2.7 (2022), pp. 1561–1593 (cited on page 14).

[33] Kevin Rossi and Raffaella Buonsanti. "Shaping Copper Nanocatalysts to Steer Selectivity in the Electrochemical CO_2 Reduction Reaction". In: *Accounts of Chemical Research* 55.5 (2022), pp. 513–524 (cited on page 14).

[34] Minki Jun et al. "Strategies to Modulate the Copper Oxidation State Toward Selective C_2+ Production in the Electrochemical CO_2 Reduction Reaction". In: *Advanced Materials* 36.21 (2024), e2313028 (cited on page 14).

[35] Yinchao Yao et al. "A surface strategy boosting the ethylene selectivity for CO_2 reduction and in situ mechanistic insights". In: *Nature Communications* 15 (2024), p. 1257 (cited on page 14).

[36] Junpeng Qu et al. "Electrochemical Carbon Dioxide Reduction to Ethylene: From Mechanistic Understanding to Catalyst Surface Engineering". In: *Nano-Micro Letters* 15 (2023), p. 178 (cited on page 14).

[37] Jin Cai et al. "Highly Selective Electrochemical Reduction of CO_2 into Methane on Nanotwinned Cu". In: *Journal of the American Chemical Society* 145 (2023), pp. 9136–9143 (cited on page 14).

[38] Jiabao Huang et al. "Recent Progress on Copper-Based Bimetallic Heterojunction Catalysts for CO_2 Electrocatalysis: Unlocking the Mystery of Product Selectivity". In: *Advanced Science* (2024) (cited on page 14).

[39] Qian Sun et al. “Atomically Dispersed Cu–Au Alloy for Efficient Electrocatalytic Reduction of Carbon Monoxide to Acetate”. In: *ACS Catalysis* 13.8 (2023), pp. 5689–5696 (cited on page 14).

[40] Hakhyeon Song et al. “Tunable Product Selectivity in Electrochemical CO_2 Reduction on Well-Mixed Ni–Cu Alloys”. In: *ACS Applied Materials & Interfaces* 13.46 (2021), pp. 55272–55280 (cited on page 14).

[41] Jinyan Huang et al. “Highly Selective Electroreduction of CO_2 to CH4 on Cu–Pd Alloy Catalyst: the Role of Palladium-Adsorbed Hydrogen Species and Blocking Effect”. In: *Advanced Science* 12.19 (2025), p. 2417247 (cited on page 14).

[42] Dimiao Luo et al. “Cu-based bimetallic catalysts for electrochemical CO_2 reduction: before and beyond the tandem effect”. In: *Nanoscale* 11.24 (2025), p. 2309865 (cited on page 15).

[43] Qingqing Qin et al. “Emerging Cu-Based Tandem Catalytic Systems for CO_2 Electroreduction to Multi-Carbon Products”. In: *Advanced Materials Interfaces* 11.13 (2024), p. 2301049 (cited on page 15).

[44] Qianwen Li, Jingjing Jiang, Xiangwen Liu, et al. “Catalyst design for the electrochemical reduction of carbon dioxide: from copper nanoparticles to copper single atoms”. In: *Microstructures* 5 (2025), p. 2025003 (cited on page 15).

[45] Ruo-Zheng Xiong et al. “Recent progress in Cu-based electrocatalysts for CO_2 reduction”. In: *Chemical Engineering Journal* 505 (2025), p. 159210 (cited on page 15).

[46] Li Li et al. “Measurement Systems and Parameters for CO_2 Photo/Electro-Conversion”. In: *CO_2 Conversion and Utilization: Principles and Fundamentals, Methodologies and Applications*. Ed. by Zhicheng Zhang. Wiley-VCH, 2023. Chap. 1 (cited on page 15).

[47] Paul A. Kempler and Adam C. Nielander. “Reliable reporting of Faradaic efficiencies for electrocatalysis research”. In: *Nature Communications* 14 (2023), p. 1158 (cited on page 15).

[48] Siddhartha Subramanian, Joost Middelkoop, and Thomas Burdyny. “Spatial reactant distribution in CO_2 electrolysis: balancing CO_2 utilization and faradaic efficiency”. In: *Sustainable Energy & Fuels* 5 (2021), pp. 6040–6048 (cited on page 15).

[49] Sumit Verma et al. “Insights into the Low Overpotential Electroreduction of CO_2 to CO on a Supported Gold Catalyst in an Alkaline Flow Electrolyzer”. In: *ACS Energy Letters* 3 (2018), pp. 193–198 (cited on page 15).

[50] Jim de Ruiter et al. “Probing the Dynamics of Low-Overpotential CO_2-to-CO Activation on Copper Electrodes with Time-Resolved Raman Spectroscopy”. In: *Journal of the American Chemical Society* 144.33 (2022), pp. 15047–15058 (cited on page 15).

[51] Yueyuan Gu et al. “A study on improving the current density performances of CO_2 electrolysers”. In: *Scientific Reports* 11 (2021), pp. 1–10 (cited on page 15).

[52] Onno van der Heijden et al. “Tafel Slope Plot as a Tool to Analyze Electrocatalytic Reactions”. In: *ACS Energy Letters* 9.4 (2024), pp. 1871–1879 (cited on page 16).

[53] Stefan Popović et al. “Stability and degradation mechanisms of copper-based catalysts for electrochemical CO_2 reduction”. In: *Angewandte Chemie International Edition* 59.36 (2020), pp. 14736–14757 (cited on page 16).

[54] Mingjie Cai et al. “Recent advances in metal-free electrocatalysts for the hydrogen evolution reaction”. In: *Journal of Materials Chemistry A* 12.2 (2024), pp. 592–612 (cited on page 16).

[55] Anders A. Feidenhans’l et al. “Precious Metal Free Hydrogen Evolution Catalyst Design and Application”. In: *Chemical Reviews* 124.9 (2024), pp. 5617–5667 (cited on page 16).

[56] Martí López et al. “Theoretical study of the mechanism of the hydrogen evolution reaction on the V_2C MXene: Thermodynamic and kinetic aspects”. In: *Journal of Catalysis* 421 (2023), pp. 252–263 (cited on page 16).

[57] Fuxi Bao et al. “Understanding the Hydrogen Evolution Reaction Kinetics of Electrodeposited Nickel-Molybdenum in Acidic, Near-Neutral, and Alkaline Conditions”. In: *ChemElectroChem* 7.24 (2020), pp. 4859–4869 (cited on page 16).

[58] Jana Mehrez et al. “Hydrogen evolution reaction mechanisms in thiosemicarbazone metal complexes: a combined theoretical and experimental investigation on the impact of proton source”. In: *Dalton Transactions* 54 (2025), pp. 8113–8122 (cited on page 17).

[59] Krishankant et al. “Unveiling a Cooperative Mechanism for the Alkaline Hydrogen Evolution Reaction: Role of Built-in Electric Field”. In: *Advanced Energy Materials* 15.8 (2025), p. 2405608 (cited on page 17).

[60] Maria B. Brands and Joost N. H. Reek. "Mechanistic Insights into Electrocatalytic Hydrogen Evolution by an Exceptionally Stable Cobalt Complex". In: *Inorganic Chemistry* 63.18 (2024), pp. 8484–8492 (cited on page 17).

[61] Paola Quaino et al. "Volcano plots in hydrogen electrocatalysis – uses and abuses". In: *Beilstein Journal of Nanotechnology* 5 (2014), pp. 846–854 (cited on page 17).

[62] Sergio Trasatti. "Work function, electronegativity, and electrochemical behaviour of metals: III. Electrolytic hydrogen evolution in acid solutions". In: *Journal of Electroanalytical Chemistry and Interfacial Electrochemistry* 39.1 (1972), pp. 163–184 (cited on page 17).

[63] Fuxi Bao et al. "Understanding the Hydrogen Evolution Reaction Kinetics of Electrodeposited Nickel-Molybdenum in Acidic, Near-Neutral, and Alkaline Conditions". In: *ChemElectroChem* 7.24 (2020), pp. 4859–4869 (cited on page 17).

[64] Frederik C. Østergaard, Alexander Bagger, and Jan Rossmeisl. "Predicting catalytic activity in hydrogen evolution reaction". In: *Current Opinion in Electrochemistry* 35 (2022), p. 101037 (cited on page 17).

[65] Changqing Li and Jong-Beom Baek. "Noble Metal (Pt, Ru, and Ir)-Based Electrocatalysts for Efficient Hydrogen Evolution Reaction". In: *ACS Omega* 5.1 (2020), pp. 31–40 (cited on page 18).

[66] Aiyi Dong et al. "Recent Advances in Non-Noble Metal Electrocatalysts for Hydrogen Evolution Reaction in Water Splitting". In: *Nanomaterials* 15.14 (2025), p. 1106 (cited on page 18).

[67] Song Xie et al. "Non-precious Electrocatalysts for the Hydrogen Evolution Reaction". In: *Innovations and Discoveries* 1.2 (2024), p. 11 (cited on page 18).

[68] Chao Wang et al. "A machine learning model with minimize feature parameters for multi-type hydrogen evolution catalyst prediction". In: *npj Computational Materials* 11.1 (2025), p. 111 (cited on page 18).

[69] Anders A. Feidenhans'l et al. "Precious Metal Free Hydrogen Evolution Catalyst Design and Application". In: *Chemical Reviews* 124.9 (2024), pp. 5617–5667 (cited on page 18).

[70] Chao Wei et al. "Recommended Practices and Benchmark Activity for Hydrogen and Oxygen Electrocatalysis in Water Splitting and Fuel Cells". In: *Advanced Materials* 31.31 (2019), e1806296 (cited on page 18).

[71] Yue Xin et al. "Copper-Based Plasmonic Catalysis: Recent Advances and Future Perspectives". In: *Advanced Materials* 33.32 (2021), p. 2008145 (cited on pages 19, 20).

[72] Jian Zhao et al. "Localized surface plasmon resonance for enhanced electrocatalysis". In: *Chemical Society Reviews* 50 (2021), pp. 12070–12097 (cited on pages 19, 20).

[73] Lucas Dias Germano, Leonardo Domenico De Angelis, and Susana Inés Córdoba de Torresi. "Plasmon-enhanced electrochemistry: A sustainable path for molecular sensing and energy production". In: *Current Opinion in Electrochemistry* 43 (2024), p. 101422 (cited on pages 19, 20, 23).

[74] Xiu Wang, Yu Mao, and Ziyun Wang. "Plasmonic-assisted Electrocatalysis for CO_2 Reduction Reaction". In: *ChemElectroChem* 11 (2024), e202300805 (cited on pages 19, 20, 24).

[75] Zhixuan Lu. "Plasmon-enhanced electrochemistry: Fundamentals and potential applications". In: *International Journal of Electrochemical Science* 20 (2025), p. 101100 (cited on pages 19–22).

[76] Fengxia Wu et al. "Metallic Heterostructures for Plasmon-Enhanced Electrocatalysis". In: *ChemPhysChem* 24 (2023), e202200881 (cited on pages 19, 20).

[77] Fengxia Wu et al. "Metallic Heterostructures for Plasmon-Enhanced Electrocatalysis". In: *ChemPhysChem* 24 (2023), e202200881 (cited on pages 19, 20).

[78] Andrew J. Bagnall, Sagar Ganguli, and Alina Sekretareva. "Hot or Not? Reassessing Mechanisms of Photocurrent Generation in Plasmon-Enhanced Electrocatalysis". In: *Angewandte Chemie International Edition* 63 (2024), e202314352 (cited on page 20).

[79] Rajesh Belgamwar et al. "Synthesis of synergistic catalysts: integrating defects, SMSI, and plasmonic effects for enhanced photocatalytic CO_2 reduction". In: *Chemical Science* 16 (2025), pp. 9766–9784 (cited on page 20).

[80] Florian Rathmann et al. "Unraveling Photothermal Effects in CO_2 Methanation over Ru/C Catalysts under Visible Light". In: *ACS Applied Energy Materials* 8.12 (2025), pp. 8365–8375 (cited on page 21).

[81] Andrew J. Bagnall, Sagar Ganguli, and Alina Sekretareva. "Hot or Not? Reassessing Mechanisms of Photocurrent Generation in Plasmon-Enhanced Electrocatalysis". In: *Angewandte Chemie International Edition* 62.52 (2023), e202314352 (cited on page 21).

[82] Viktoryia Shaustova et al. “Plasmon induced thermoelectric effect in graphene”. In: *Nature Communications* 9 (2018), p. 5190 (cited on page 21).

[83] Mengqi Sun et al. “Interband and Intraband Hot Carrier-Driven Photocatalysis on Plasmonic Bimetallic Nanoparticles: A Case Study of Au–Cu Alloy Nanoparticles”. In: *ACS Nanoscience Au* 4.5 (2024), pp. 360–373 (cited on page 21).

[84] Pardeep Kumar et al. “Photoexcited Plasmon-Driven Ultrafast Dynamics of the Adsorbate Probed by Femtosecond Time-Resolved Surface-Enhanced Time-Domain Raman Spectroscopy”. In: *The Journal of Physical Chemistry Letters* 14.10 (2023), pp. 2845–2853 (cited on page 21).

[85] Rishi Verma, Gunjan Sharma, and Vivek Polshettiwar. “The paradox of thermal vs. non-thermal effects in plasmonic photocatalysis”. In: *Nature Communications* 15 (2024), p. 7974 (cited on page 21).

[86] Sara El Hakim, Tony Chave, and Sergey I. Nikitenko. “Deciphering the reaction mechanisms of photothermal hydrogen production using H/D kinetic isotope effect”. In: *Catalysis Science & Technology* 12 (2022), pp. 5252–5259 (cited on page 21).

[87] Cecilia Romeo, Andrea Baldi, and Sven H. C. Askes. “Engineering light-driven thermal landscapes at the nanoscale”. In: *APL Materials* 13.8 (2025), p. 080601 (cited on page 21).

[88] Giulia Dall’Osto et al. “Peeking into the Femtosecond Hot-Carrier Dynamics Reveals Unexpected Mechanisms in Plasmonic Photocatalysis”. In: *Journal of the American Chemical Society* 146.5 (2024), pp. 2208–2218 (cited on page 21).

[89] María C. Nevárez Martínez et al. “Numerical Simulation of Light to Heat Conversion by Plasmonic Nanoheaters”. In: *Nano Letters* 25.1 (2025), pp. 230–235 (cited on page 21).

[90] Weiwei Lu et al. “Photoelectrocatalytic Reduction of CO_2 for Efficient Methanol Production: Au Nanoparticles as Electrocatalysts and Light Supports”. In: *Industrial & Engineering Chemistry Research* 59.10 (2020), pp. 4375–4383 (cited on page 22).

[91] Yicui Kang et al. “Effect of crystal facets in plasmonic catalysis”. In: *Nature Communications* 15.3923 (2024), pp. 1–13 (cited on pages 22, 29, 39, 52).

[92] Takuya Yamada et al. “High Specific Activity during Electrochemical CO_2 Reduction through Homogeneous Deposition of Gold Nanoparticles on Gas Diffusion Electrodes”. In: *ACS Applied Energy Materials* 8.2 (2025), pp. 1230–1237 (cited on page 22).

[93] Kim Robert Gustavsen, Erik Andrew Johannessen, and Kaiying Wang. “Carbon modified silver thin-film catalysts for electrochemical reduction of CO_2 to syngas with tunable H_2/CO ratio”. In: *Electrochemistry Communications* 155 (2023), p. 107582 (cited on page 22).

[94] Elizabeth R. Corson et al. “In Situ ATR–SEIRAS of Carbon Dioxide Reduction at a Plasmonic Silver Cathode”. In: *Journal of the American Chemical Society* 142.27 (2020), pp. 11750–11762 (cited on page 22).

[95] Rui Lin et al. “Light tuning CO/H_2 composition on Ag: Unraveling CO_2 mass transfer and electron–phonon coupling in plasmon-enhanced electrocatalysis”. In: *Nano Research* 18.1 (2025), p. 94907042 (cited on page 22).

[96] Jing Xue et al. “The plasmonic effect of Cu on tuning CO_2 reduction activity and selectivity”. In: *Physical Chemistry Chemical Physics* 26.4 (2024), pp. 1234–1242 (cited on page 22).

[97] Elisabeth Robens et al. “Bimetallic Copper–Silver Catalysts for the Electrochemical Reduction of CO_2 to Ethanol”. In: *ACS Applied Energy Materials* 6.14 (2023), pp. 7600–7609 (cited on pages 22, 24).

[98] Esteban Landaeta, Nir I. Kadosh, and Zachary D. Schultz. “Mechanistic Study of Plasmon-Assisted *In Situ* Photoelectrochemical CO_2 Reduction to Acetate with a Ag/Cu_2O Nanodendrite Electrode”. In: *ACS Catalysis* 13.3 (2023), pp. 1947–1957 (cited on page 22).

[99] Li Zhu et al. “Plasmon-Enhanced C_2H_4 Generation in the CO_2 Electroreduction Reaction on a CuPd Tandem Catalyst”. In: *Journal of the American Chemical Society* 147.36 (2025), pp. 33003–33009 (cited on pages 22, 29, 52, 69).

[100] Yan Wei et al. “Site-selective modification of AgPt on multibranched Au nanostars for plasmon-enhanced hydrogen evolution and methanol oxidation reaction in visible to near-infrared region”. In: *Journal of Power Sources* 425 (2019), pp. 17–26 (cited on page 23).

[101] Maria Paula de Souza Rodrigues et al. “Gold–Rhodium Nanoflowers for the Plasmon-Enhanced Hydrogen Evolution Reaction under Visible Light”. In: *ACS Catalysis* 11.21 (2021), pp. 13832–13841 (cited on page 23).

[102] Xia Guo et al. “Plasmon-enhanced electrocatalytic hydrogen/oxygen evolution by Pt/Fe–Au nanorods”. In: *Journal of Materials Chemistry A* 6.17 (2018), pp. 7770–7778 (cited on page 23).

[103] Menglei Zhu et al. “Strategic modulation of energy transfer in Au–TiO_2–Pt nanodumbbells: plasmon-enhanced hydrogen evolution reaction”. In: *Nanoscale* 12.44 (2020), pp. 22705–22714 (cited on page 23).

[104] Juan Jose Quintana Gonzalez et al. “Defects engineering of Au@MoS_2 nanostructures for conventional and plasmon-enhanced hydrogen evolution reaction”. In: *International Journal of Hydrogen Energy* 51.Part C (2024), pp. 371–382 (cited on page 23).

[105] Huang JingWei Li et al. “Plasmon-induced local electric field improved hydrogen evolution reaction on Ag/Mo_2C nanosheets”. In: *Nano Research* 18.1 (2025), p. 94907043 (cited on page 23).

[106] Wenmin Zhang et al. “Plasmon of Au nanorods activates metal–organic frameworks for both the hydrogen evolution reaction and oxygen evolution reaction”. In: *Nanoscale* 12.33 (2020), pp. 17456–17463 (cited on page 23).

[107] Sourav Rej et al. “Determining Plasmonic Hot Electrons and Photothermal Effects during H_2 Evolution with TiN–Pt Nanohybrids”. In: *ACS Catalysis* 10.9 (2020), pp. 5261–5270 (cited on page 23).

[108] Li Zhu et al. “Tuning the intermediate reaction barriers by a CuPd catalyst to improve the selectivity of CO_2 electroreduction to C_2 products”. In: *Chinese Journal of Catalysis* 42.9 (2021), pp. 1500–1508 (cited on pages 24, 25, 30, 33).

[109] Liuxiang Huo et al. “Applications of Nickel-Based Electrocatalysts for Hydrogen Evolution Reaction”. In: *Advanced Energy and Sustainability Research* 3.4 (2022), p. 2100189 (cited on page 24).

[110] Shuang Ma et al. “Electroreduction of Carbon Dioxide to Hydrocarbons Using Bimetallic Cu-Pd Catalysts with Different Mixing Patterns”. In: *Journal of the American Chemical Society* 139.1 (2017), pp. 47–50 (cited on page 25).

[111] Qin Chen et al. “Ordered Ag Nanoneedle Arrays with Enhanced Electrocatalytic CO_2 Reduction via Structure-Induced Inhibition of Hydrogen Evolution”. In: *Nano Letters* 22.15 (2022), pp. 6276–6284 (cited on pages 26, 69, 70, 72–74).

[112] Mariana P. S. Rodrigues et al. “Gold-Rhodium Nanoflowers for the Plasmon-Enhanced CO_2 Electroreduction Reaction upon Visible Light”. In: *ACS Catalysis* 13.1 (2023), pp. 267–279 (cited on page 29).

[113] Yifan Zhang et al. “Plasmonic Ag-decorated Cu_2O nanowires for boosting photoelectrochemical CO_2 reduction to multi-carbon products”. In: *Chemical Communications* 58.67 (2022), pp. 9421–9424 (cited on page 29).

[114] Mariana P. S. Rodrigues et al. “Gold-Rhodium Nanoflowers for the Plasmon-Enhanced Hydrogen Evolution Reaction under Visible Light”. In: *ACS Catalysis* 11.21 (2021), pp. 13543–13555 (cited on page 29).

[115] Xiaohui Wu et al. “Bimetallic Au@Rh core-shell nanostars with plasmon-enhanced catalytic performance in hydrogen evolution reaction”. In: *CrystEngComm* 25.9 (2023), pp. 1365–1373 (cited on page 29).

[116] Chao Xu et al. “Plasmon-enhanced electrocatalytic hydrogen evolution based on tannic acid-platinum film functionalized gold nanoparticles”. In: *New Journal of Chemistry* 46.40 (2022), pp. 19263–19270 (cited on page 29).

[117] Hao Zhang et al. “In-Situ-Grown Cu Dendrites Plasmonically Enhance Electrocatalytic Hydrogen Evolution on Facet-Engineered Cu_2O”. In: *Advanced Materials* 35.42 (2023), e2305742 (cited on page 29).

[118] Hyemin Jung et al. “Directing Energy Flow in Core-Shell Nanostructures for Efficient Plasmon-Enhanced Electrocatalysis”. In: *Nano Letters* 23.5 (2023), pp. 1774–1780 (cited on page 29).

[119] Takuya Kameyama et al. “Promoting Oxygen Reduction Reaction by Excitation of Localized Surface Plasmon of Shape- and Facet-Controlled Octahedral Au@Pt Core-Shell Nanocrystals”. In: *ChemElectroChem* 10.17 (2023), e202300182 (cited on page 29).

[120] Wei Jiang et al. “Sensitive detection of extracellular hydrogen peroxide using plasmon-enhanced electrochemical activity on Pd-tipped Au nanobipyramids”. In: *Analyst* 148.16 (2023), pp. 3791–3797 (cited on page 29).

[121] Sangho Lee et al. “Multi-Layered PtAu Nanoframes and Their Light-Enhanced Electrocatalytic Activity via Plasmonic Hot Spots”. In: *Small* 19.17 (2023), e2206377 (cited on page 29).

[122] Hao Chen et al. “Amorphous CoFeB nanosheets with plasmon-regulated dynamic active sites for electrocatalytic water oxidation”. In: *Applied Catalysis B: Environmental* 323 (2023), p. 122187 (cited on page 29).

[123] Matthew J. Kale, Tatevik Avanesian, and Paul Christopher. “Direct Photocatalysis by Plasmonic Nanostructures”. In: *ACS Catalysis* 4.1 (2014), pp. 116–128 (cited on pages 29, 69).

[124] Eiji Kazuma and Youngku Kim. “Mechanistic Studies of Plasmon Chemistry on Metal Catalysts”. In: *Angewandte Chemie International Edition* 58.15 (2019), pp. 4800–4808 (cited on pages 29, 69).

[125] Zachary Fusco and Francis J. Beck. “Advances in fundamentals and application of plasmon-assisted CO_2 photoreduction”. In: *Nanophotonics* 13.4 (2024), pp. 387–417 (cited on pages 29, 69).

[126] Hao Zhang, Muhammad Ijaz, and Richard J. Blaikie. “Recent review of surface plasmons and plasmonic hot electron effects in metallic nanostructures”. In: *Frontiers of Physics* 18.6 (2023), p. 63602 (cited on pages 29, 69).

[127] Udayan Das, Ranjan Biswas, and Naba Mazumder. “Elucidating thermal effects in plasmonic metal nanostructures: a tutorial review”. In: *The European Physical Journal Plus* 137.11 (2022), p. 1248 (cited on page 29).

[128] Stefan Ezendam et al. “Hybrid Plasmonic Nanomaterials for Hydrogen Generation and Carbon Dioxide Reduction”. In: *ACS Energy Letters* 7.2 (2022), pp. 778–815 (cited on page 29).

[129] Andrei Stefancu et al. “Interface-Dependent Selectivity in Plasmon-Driven Chemical Reactions”. In: *ACS Nano* 17.3 (2023), pp. 3119–3127 (cited on page 29).

[130] Feng Wu et al. “Metallic Heterostructures for Plasmon-Enhanced Electrocatalysis”. In: *ChemPhysChem* 24.15 (2023), e202200881 (cited on page 29).

[131] Emiliano Cortes et al. “Experimental characterization techniques for plasmon-assisted chemistry”. In: *Nature Reviews Chemistry* 6.4 (2022), pp. 259–274 (cited on page 30).

[132] Jun Zhao et al. “Localized surface plasmon resonance for enhanced electrocatalysis”. In: *Chemical Society Reviews* 50.21 (2021), pp. 12070–12097 (cited on page 30).

[133] Yu Lei et al. “Recent advances on electrocatalytic CO_2 reduction to resources: Target products, reaction pathways and typical catalysts”. In: *Chemical Engineering Journal* 453 (2023), p. 139663 (cited on pages 30, 35, 69).

[134] Xinyu Wang, Yifan Mao, and Zhen Wang. “Plasmonic-assisted Electrocatalysis for CO_2 Reduction Reaction”. In: *ChemElectroChem* 11.8 (2024), e202300805 (cited on pages 30, 35, 38, 60, 69).

[135] Hao Li et al. “Electric-field promoted C-C coupling over Cu nanoneedles for CO_2 electroreduction to C_2 products”. In: *Chinese Journal of Catalysis* 43.2 (2022), pp. 519–525 (cited on pages 30, 60, 69).

[136] Bo Liu et al. “Intermediate enrichment effect of porous Cu catalyst for CO_2 electroreduction to C_2 fuels”. In: *Electrochimica Acta* 388 (2021), p. 138635 (cited on pages 30, 69).

[137] Qiang Liu et al. “Highly Tensile Strained Cu(100) Surfaces by Epitaxial Grown Hexagonal Boron Nitride for CO_2 Electroreduction to C_2+ Products”. In: *Nano Letters* 24 (2024), p. 13741 (cited on pages 30, 69).

[138] Bo Yang et al. “Accelerating CO_2 Electroreduction to Multicarbon Products via Synergistic Electric-Thermal Field on Copper Nanoneedles”. In: *Journal of the American Chemical Society* 144.7 (2022), pp. 3039–3049 (cited on pages 30, 69).

[139] Yang Zhou et al. “Vertical Cu Nanoneedle Arrays Enhance the Local Electric Field Promoting C_2 Hydrocarbons in the CO_2 Electroreduction”. In: *Nano Letters* 22.5 (2022), pp. 1963–1970 (cited on pages 30, 69).

[140] Yao Xin et al. “Copper-Based Plasmonic Catalysis: Recent Advances and Future Perspectives”. In: *Advanced Materials* 33.32 (2021), e2008145 (cited on page 30).

[141] Jing Huang et al. “Structural Sensitivities in Bimetallic Catalysts for Electrochemical CO_2 Reduction Revealed by Ag-Cu Nanodimers”. In: *Journal of the American Chemical Society* 141.6 (2019), pp. 2490–2499 (cited on pages 30, 69).

[142] Yadong Ma et al. “Confined Growth of Silver-Copper Janus Nanostructures with 100 Facets for Highly Selective Tandem Electrocatalytic Carbon Dioxide Reduction”. In: *Advanced Materials* 34.19 (2022), e2110607 (cited on pages 30, 69).

[143] Shuai Zhang et al. “Electrochemical Reduction of CO_2 Toward C_2 Valuables on Cu@Ag Core-Shell Tandem Catalyst with Tunable Shell Thickness”. In: *Small* 17.37 (2021), e2102293 (cited on pages 30, 69).

[144] Yi Chen et al. “Ethylene Selectivity in Electrocatalytic CO_2 Reduction on Cu Nanomaterials: A Crystal Phase-Dependent Study”. In: *Journal of the American Chemical Society* 142.29 (2020), pp. 12760–12766 (cited on page 30).

[145] Haoran Jia et al. “Symmetry-Broken Au-Cu Heterostructures and their Tandem Catalysis Process in Electrochemical CO_2 Reduction”. In: *Advanced Functional Materials* 31.27 (2021), p. 2101255 (cited on page 30).

[146] Yi Zheng et al. “Seeded Growth of Gold-Copper Janus Nanostructures as a Tandem Catalyst for Efficient Electroreduction of CO_2 to C_2+ Products”. In: *Small* 18.19 (2022), e2201695 (cited on page 30).

[147] Yang Li, Zhiwei Tian, and Liang Chen. “Theoretical Understanding of the Interface Effect in Promoting Electrochemical CO_2 Reduction on Cu-Pd Alloys”. In: *The Journal of Physical Chemistry C* 125.39 (2021), pp. 21381–21389 (cited on page 30).

[148] Zhipeng Lyu et al. “Kinetically Controlled Synthesis of Pd-Cu Janus Nanocrystals with Enriched Surface Structures and Enhanced Catalytic Activities toward CO_2 Reduction”. In: *Journal of the American Chemical Society* 143.1 (2021), pp. 149–162 (cited on page 30).

[149] Shengliang Ma et al. “Electroreduction of Carbon Dioxide to Hydrocarbons Using Bimetallic Cu-Pd Catalysts with Different Mixing Patterns”. In: *Journal of the American Chemical Society* 139.1 (2017), pp. 47–50 (cited on page 30).

[150] Feng Li et al. “Ultrafine Cu-Pd bimetallic clusters enhance asymmetric electron distribution to boost C-C coupling in photothermal CO_2-to-ethanol conversion”. In: *Applied Catalysis B: Environmental* 355 (2024), p. 124187 (cited on pages 30, 40).

[151] Jonas Wohlwend et al. “CO_2 Conversion in Cu-Pd Based Disordered Network Metamaterials with Ultrasmall Mode Volumes”. In: *Nano Letters* 25.10 (2025), pp. 3740–3746 (cited on pages 30, 40).

[152] Xinyu Wang et al. “Cu-based bimetallic catalysts for CO_2 reduction reaction”. In: *Advanced Sensing and Energy Materials* 1.3 (2022), p. 100023 (cited on page 30).

[153] Lei Zhu et al. “Tuning the intermediate reaction barriers by a CuPd catalyst to improve the selectivity of CO_2 electroreduction to C_2 products”. In: *Chinese Journal of Catalysis* 42.9 (2021), pp. 1500–1508 (cited on page 30).

[154] Yi Wei et al. “Uncovering Photoelectronic and Photothermal Effects in Plasmon-Mediated Electrocatalytic CO_2 Reduction”. In: *Angewandte Chemie International Edition* 63.13 (2024), e202317740 (cited on pages 37, 39, 40, 69).

[155] Emiliano Cortes et al. “Plasmonic hot electron transport drives nano-localized chemistry”. In: *Nature Communications* 8 (2017), p. 14880 (cited on page 38).

[156] Lina Kabalan et al. “A computational study of the properties of low- and high-index Pd, Cu and Zn surfaces”. In: *Physical Chemistry Chemical Physics* 23.27 (2021), pp. 14649–14661 (cited on page 39).

[157] Jacopo Gargiulo et al. “From Optical to Chemical Hot Spots in Plasmonics”. In: *Accounts of Chemical Research* 52.9 (2019), pp. 2525–2535 (cited on page 40).

[158] Jacopo Gargiulo et al. “Impact of bimetallic interface design on heat generation in plasmonic Au/Pd nanostructures studied by single-particle thermometry”. In: *Nature Communications* 14.1 (2023), p. 3813 (cited on page 40).

[159] Robert E. Vos et al. “How Temperature Affects the Selectivity of the Electrochemical CO_2 Reduction on Copper”. In: *ACS Catalysis* 13.12 (2023), pp. 8080–8091 (cited on page 40).

[160] Meng Liu et al. “Potential Alignment in Tandem Catalysts Enhances CO_2-to-C_2H_4 Conversion Efficiencies”. In: *Journal of the American Chemical Society* 146.1 (2024), pp. 468–475 (cited on page 41).

[161] Yuki Katayama et al. “An In Situ Surface-Enhanced Infrared Absorption Spectroscopy Study of Electrochemical CO_2 Reduction: Selectivity Dependence on Surface C-Bound and O-Bound Reaction Intermediates”. In: *Journal of Physical Chemistry C* 123.10 (2019), pp. 5951–5963 (cited on page 42).

[162] Da Gao et al. “Switchable CO_2 electroreduction via engineering active phases of Pd nanoparticles”. In: *Nano Research* 10.6 (2017), pp. 2181–2191 (cited on page 42).

[163] Eric R. Corson et al. “In Situ ATR-SEIRAS of Carbon Dioxide Reduction at a Plasmonic Silver Cathode”. In: *Journal of the American Chemical Society* 142 (2020), p. 11750 (cited on page 42).

[164] Xiaoming Wei et al. “Highly Selective Reduction of CO_2 to C_2+ Hydrocarbons at Copper/Polyaniline Interfaces”. In: *ACS Catalysis* 10.7 (2020), pp. 4103–4111 (cited on page 43).

[165] Shuang Zhu et al. “Direct Observation on Reaction Intermediates and the Role of Bicarbonate Anions in CO_2 Electrochemical Reduction Reaction on Cu Surfaces”. In: *Journal of the American Chemical Society* 139.44 (2017), pp. 15664–15667 (cited on page 43).

[166] Xinyu Zi et al. “Breaking K^+ Concentration Limit on Cu Nanoneedles for Acidic Electrocatalytic CO_2 Reduction to Multi-Carbon Products”. In: *Angewandte Chemie International Edition* 62.42 (2023), e202309351 (cited on page 43).

[167] Xin Chang et al. “Understanding the complementarities of surface-enhanced infrared and Raman spectroscopies in CO adsorption and electrochemical reduction”. In: *Nature Communications* 13.1 (2022), p. 2656 (cited on page 43).

[168] C. David Zeinalipour-Yazdi et al. “CO adsorption over Pd nanoparticles: A general framework for IR simulations on nanoparticles”. In: *Surface Science* 646 (2016), pp. 210–220 (cited on page 43).

[169] Shuang Liu et al. “Tuning crystal-phase of bimetallic single-nanoparticle for catalytic hydrogenation”. In: *Nature Communications* 13.1 (2022), p. 4559 (cited on page 43).

[170] Chathura M. Gunathunge et al. “Spectroscopic Observation of Reversible Surface Reconstruction of Copper Electrodes under CO_2 Reduction”. In: *Journal of Physical Chemistry C* 121.22 (2017), pp. 12337–12344 (cited on page 44).

[171] Sofia B. Varandili et al. “Elucidating the structure-dependent selectivity of CuZn towards methane and ethanol in CO_2 electroreduction using tailored Cu/ZnO precatalysts”. In: *Chemical Science* 12.43 (2021), pp. 14484–14493 (cited on page 49).

[172] Yi Zheng et al. “Seeded Growth of Gold-Copper Janus Nanostructures as a Tandem Catalyst for Efficient Electroreduction of CO_2 to C_2+ Products”. In: *Small* 18.19 (2022), e2201695 (cited on page 49).

[173] Zhipeng Lyu et al. “Kinetically Controlled Synthesis of Pd-Cu Janus Nanocrystals with Enriched Surface Structures and Enhanced Catalytic Activities toward CO_2 Reduction”. In: *Journal of the American Chemical Society* 143.1 (2021), pp. 149–162 (cited on page 49).

[174] Georg Kresse and Jürgen Furthmüller. “From ultrasoft pseudopotentials to the projector augmented-wave method”. In: *Physical Review B* 59.3 (1998), pp. 1758–1775 (cited on page 49).

[175] Georg Kresse and Jürgen Furthmüller. “Efficient iterative schemes for ab initio total-energy calculations using a plane-wave basis set”. In: *Physical Review B* 54.16 (1996), pp. 11169–11186 (cited on page 49).

[176] Pablo J. Megía et al. “Hydrogen Production Technologies: From Fossil Fuels toward Renewable Sources. A Mini Review.” In: *Energy Fuels* 35 (2021), pp. 16403–16415 (cited on page 51).

[177] Wolfgang Lubitz and Warren Tumas. “Hydrogen: An Overview”. In: *Chemical Reviews* 107.10 (2007), pp. 3900–3903 (cited on page 51).

[178] Emanuele Taibi, Tomke Güldenberg, Morgan Bazilian, et al. *Hydrogen from Renewable Power: Technology Outlook for the Energy Transition*. 2018 (cited on page 51).

[179] Chao Jiang et al. “Photoelectrochemical devices for solar water splitting – materials and challenges”. In: *Chemical Society Reviews* 46.15 (2017), pp. 4645–4660 (cited on page 51).

[180] Nature Catalysis Editorial. “Price pressures on metals”. In: *Nature Catalysis* 2.9 (2019), p. 735 (cited on page 51).

[181] Zhi-Yong Yu, Jiao Li, Zheng Chen, et al. “Clean and Affordable Hydrogen Fuel from Alkaline Water Splitting: Past, Recent Progress, and Future Prospects”. In: *Advanced Materials* 33.50 (2021), p. 2007100 (cited on page 51).

[182] Yu-Yi Chen, Yu Zhang, Zheng Wang, et al. “Self-Templated Fabrication of $MoNi_4/MoO_{3-x}$ Nanorod Arrays with Dual Active Components for Highly Efficient Hydrogen Evolution”. In: *Advanced Materials* 29.33 (2017), p. 1703311 (cited on page 51).

[183] Jimin Kim, Junghoon Lee, Minwoo Choi, et al. “Efficient Alkaline Hydrogen Evolution Reaction Using Superaerophobic Ni Nanoarrays with Accelerated H_2 Bubble Release”. In: *Advanced Materials* 35.48 (2023), p. 2305844 (cited on pages 51, 56).

[184] Chao Wei, Yao Li, Xin Zhang, et al. “Surface Composition Dependent Ligand Effect in Tuning the Activity of Nickel–Copper Bimetallic Electrocatalysts toward Hydrogen Evolution in Alkaline”. In: *Journal of the American Chemical Society* 142.17 (2020), pp. 7765–7775 (cited on page 51).

[185] Jin-Tao Ren et al. “Interface engineering of in-situ formed nickel hydr(oxy)oxides on nickel nitrides to boost alkaline hydrogen electrocatalysis”. In: *Applied Catalysis B: Environmental* 309 (2022), p. 121279 (cited on page 51).

[186] Tianyi Wang, Lu Cao, Min Li, et al. “Weakening hydrogen adsorption on nickel via interstitial nitrogen doping promotes bifunctional hydrogen electrocatalysis in alkaline solution”. In: *Energy & Environmental Science* 12.11 (2019), pp. 3522–3529 (cited on pages 51, 56).

[187] Jian Zhang, Ting Wang, Pei Liu, et al. “Interface Engineering of MoS_2/Ni_3S_2 Heterostructures for Highly Enhanced Electrochemical Overall-Water-Splitting Activity”. In: *Angewandte Chemie International Edition* 55.23 (2016), pp. 6702–6707 (cited on pages 51, 56).

[188] Jingyi Luo et al. “Water photolysis at 12.3% efficiency via perovskite photovoltaics and Earth-abundant catalysts”. In: *Science* 345.6204 (2014), pp. 1593–1596 (cited on pages 51, 56).

[189] Jian Zhang, Pei Liu, Jiaguo Zhang, et al. “Engineering water dissociation sites in MoS2 nanosheets for accelerated electrocatalytic hydrogen production”. In: *Energy & Environmental Science* 9.8 (2016), pp. 2789–2793 (cited on pages 51, 56).

[190] Cheng Liu, Hao Li, Xin Wang, et al. “Manipulating d-Band Center of Nickel by Single-Iodine-Atom Strategy for Boosted Alkaline Hydrogen Evolution Reaction”. In: *Journal of the American Chemical Society* 146.59 (2024), pp. 26844–26854 (cited on pages 51, 56).

[191] Jiayi Qu, Yang Xu, Yajun Sun, et al. “Efficient Hydrogen Evolution on Antiperovskite CuNCo3 Nanowires by Mo Incorporation and its Trifunctionality for Zn Air Batteries and Overall Water Splitting”. In: *Small* 20.48 (2024), p. 2304541 (cited on pages 51, 56).

[192] Julie A. Bau, Stephan N. Steinmann, et al. “Role of Oxidized Mo Species on the Active Surface of Ni–Mo Electrocatalysts for Hydrogen Evolution under Alkaline Conditions”. In: *ACS Catalysis* 10.21 (2020), pp. 12858–12866 (cited on pages 51, 56).

[193] Jinhao Zhao et al. “Localized surface plasmon resonance for enhanced electrocatalysis”. In: *Chemical Society Reviews* 50.21 (2021), pp. 12070–12097 (cited on page 52).

[194] Mangesh J. Kale, Tigran Avanesian, and Phillip Christopher. “Direct Photocatalysis by Plasmonic Nanostructures”. In: *ACS Catalysis* 4.1 (2014), pp. 116–128 (cited on page 52).

[195] Rui Zhang, Yang Zhang, Zheng Dong, et al. “How To Identify Plasmons from the Optical Response of Nanostructures”. In: *ACS Nano* 11.7 (2017), pp. 7321–7335 (cited on page 52).

[196] Ravishankar Sundararaman et al. “Theoretical predictions for hot-carrier generation from surface plasmon decay”. In: *Nature Communications* 5 (2014), p. 5788 (cited on page 52).

[197] Lin Zhou, Qiang Huang, and Younan Xia. “Plasmon-Induced Hot Electrons in Nanostructured Materials: Generation, Collection, and Application to Photochemistry”. In: *Chemical Reviews* 124.14 (2024), pp. 8597–8619 (cited on page 52).

[198] Andrei Stefancu et al. “Electronic excitations at the plasmon–molecule interface”. In: *Nature Physics* 20.7 (2024), pp. 1065–1077 (cited on page 52).

[199] Xuejun Cui, Yong Zhu, Wei Zhang, et al. “Photothermal Nanomaterials: A Powerful Light-to-Heat Converter”. In: *Chemical Reviews* 123.11 (2023), pp. 6891–6952 (cited on page 52).

[200] Shuang Li, Peng Zhang, Qiang Wang, et al. “Recent Advances in Plasmonic Nanostructures for Enhanced Photocatalysis and Electrocatalysis”. In: *Advanced Materials* 33.5 (2021), p. 2000086 (cited on page 52).

[201] Hao Zhang, Jiaqi Diao, Yuxiang Liu, et al. “In-Situ-Grown Cu Dendrites Plasmonically Enhance Electrocatalytic Hydrogen Evolution on Facet-Engineered Cu_2O”. In: *Advanced Materials* 35.42 (2023), p. 2305742 (cited on page 52).

[202] Cheng Cai, Shiqiang Zhang, Qiang Li, et al. “Atomically Local Electric Field Induced Interface Water Reorientation for Alkaline Hydrogen Evolution Reaction”. In: *Angewandte Chemie International Edition* 62.25 (2023), e202300873 (cited on page 52).

[203] Yidong Wei, Zhen Mao, Tian-Wei Jiang, et al. “Uncovering Photoelectronic and Photothermal Effects in Plasmon-Mediated Electrocatalytic CO_2 Reduction”. In: *Angewandte Chemie* 136.13 (2024), e202317740 (cited on page 52).

[204] Yao Shi, Xun Wang, Yixin Wang, et al. “Hot Electron of Au Nanorods Activates the Electrocatalysis of Hydrogen Evolution on MoS2 Nanosheets”. In: *Journal of the American Chemical Society* 137.23 (2015), pp. 7365–7370 (cited on pages 52, 56).

[205] Shi-Sheng Wang, Ming Chen, Xin Xu, et al. “Boosting Electrocatalytic Hydrogen Evolution over Metal–Organic Frameworks by Plasmon-Induced Hot-Electron Injection”. In: *Angewandte Chemie International Edition* 58.31 (2019), pp. 10713–10717 (cited on pages 52, 56, 63).

[206] Marco P. S. Rodrigues, Aline H. B. Dourado, Lucas O. Cutolo, et al. “Gold–Rhodium Nanoflowers for the Plasmon-Enhanced Hydrogen Evolution Reaction under Visible Light”. In: *ACS Catalysis* 11.21 (2021), pp. 13543–13555 (cited on pages 52, 56).

[207] Hao Li, Yue Zhou, Qiyou Wang, et al. “Plasmon-induced local electric field improved hydrogen evolution reaction on Ag/Mo_2C nanosheets”. In: *Nano Research* 18 (2025) (cited on pages 52, 56).

[208] Yulong Yuan, Ze Li, Zhen Zhang, et al. “Earth-abundant photocatalyst for H_2 generation from NH_3 with light-emitting diode illumination”. In: *Science* 378.6623 (2022), pp. 889–893 (cited on page 52).

[209] Holger Natter, Martin Schmelzer, and Rolf Hempelmann. “Nanocrystalline nickel and nickel-copper alloys: Synthesis, characterization, and thermal stability”. In: *Journal of Materials Research* 13.5 (1998), pp. 1186–1197 (cited on page 52).

[210] I. Baskaran, T. S. N. Sankara Narayanan, and A. Stephen. “Pulsed electrodeposition of nanocrystalline Cu–Ni alloy films and evaluation of their characteristic properties”. In: *Materials Letters* 60.16 (2006), pp. 1990–1995 (cited on page 52).

[211] Hong Su, Qiang Wang, Wei Zhang, et al. “Insights into Antiperovskite $Ni_3In_{1-x}Cu_xN$ Multi-Crystalline Nanoplates and Bulk Cubic Particles as Efficient Electrocatalysts on Hydrogen Evolution Reaction”. In: *Small* 18.34 (2022), p. 2105906 (cited on page 56).

[212] Yao Zhang, Jian Li, Fei Wang, et al. “3D Porous Hierarchical Nickel–Molybdenum Nitrides Synthesized by RF Plasma as Highly Active and Stable Hydrogen-Evolution-Reaction Electrocatalysts”. In: *Advanced Energy Materials* 6.13 (2016), p. 1600221 (cited on page 56).

[213] Jian Chen, Peng Liu, Shun Wang, et al. “Enhanced electrocatalysis of NiMnIn Heusler alloy films for hydrogen evolution reaction by magnetic field”. In: *Journal of Alloys and Compounds* 877 (2021), p. 160271 (cited on page 56).

[214] D. Balaji, K. Venkatesh, A. Kumar, et al. “Carbon supported Ni_3N/Ni heterostructure for hydrogen evolution reaction in both acid and alkaline media”. In: *International Journal of Hydrogen Energy* 46.57 (2021), pp. 30739–30749 (cited on page 56).

[215] Sergio Trasatti. “Electronegativity, work function, and heat of adsorption of hydrogen on metals”. In: *Journal of the Chemical Society, Faraday Transactions 1* 68 (1972), pp. 229–236 (cited on page 58).

[216] Shanshan Liu, Yang Li, Xia Yu, et al. “Quantifying the distinct role of plasmon enhancement mechanisms in prototypical antenna-reactor photocatalysts”. In: *Nature Communications* 16 (2025), p. 2245 (cited on page 60).

[217] Sibel Ayas, Arlind Cupallari, and Aykut Dana. “Probing hot-electron effects in wide area plasmonic surfaces using X-ray photoelectron spectroscopy”. In: *Applied Physics Letters* 105.23 (2014), p. 231603 (cited on page 61).

[218] Adam J. Bagnall, Srivatsan Ganguli, and Anna Sekretareva. “Hot or Not? Reassessing Mechanisms of Photocurrent Generation in Plasmon-Enhanced Electrocatalysis”. In: *Angewandte Chemie International Edition* 63.49 (2024), e202314352 (cited on page 61).

[219] Yao Zheng et al. “The Hydrogen Evolution Reaction in Alkaline Solution: From Theory, Single Crystal Models, to Practical Electrocatalysts”. In: *Angewandte Chemie International Edition* 57.26 (2018), pp. 7568–7579 (cited on page 61).

[220] Tong Wu, Chang-Guo Zhan, et al. “Surface-treated carbon electrodes with modified potential of zero charge for capacitive deionization”. In: *Water Research* 93 (2016), pp. 30–37 (cited on page 62).

[221] Sergio Trasatti. “Work function, electronegativity, and electrochemical behaviour of metals: III. Electrolytic hydrogen evolution in acid solutions”. In: *Journal of Electroanalytical Chemistry* 39.1 (1972), pp. 163–184 (cited on page 62).

[222] Israel Ledezma-Yanez, William David Z. Wallace, Shaojian Chen, et al. “Interfacial water reorganization as a pH-dependent descriptor of the hydrogen evolution rate on platinum electrodes”. In: *Nature Energy* 2 (2017), p. 17031 (cited on page 62).

[223] Nor A. R. Che Mohamad, Muhamad Amir, et al. “Plasmon-Driven Reorientation of Interfacial Water for Wastewater Electrolysis with Light-Emitting Diode Illumination”. In: *Advanced Science* 12.18 (2025), e07147 (cited on page 62).

[224] Georg Kresse and Jürgen Hafner. "Ab initio molecular dynamics for liquid metals". In: *Physical Review B* 47.1 (1993), pp. 558–561 (cited on page 66).

[225] Georg Kresse and Jürgen Furthmüller. "Efficient iterative schemes for ab initio total-energy calculations using a plane-wave basis set". In: *Physical Review B* 54.16 (1996), pp. 11169–11186 (cited on page 66).

[226] Georg Kresse and Daniel Joubert. "From ultrasoft pseudopotentials to the projector augmented-wave method". In: *Physical Review B* 59.3 (1999), pp. 1758–1775 (cited on page 66).

[227] Peter E. Blöchl. "Projector augmented-wave method". In: *Physical Review B* 50.24 (1994), pp. 17953–17979 (cited on page 66).

[228] John P. Perdew, Kieron Burke, and Matthias Ernzerhof. "Generalized Gradient Approximation Made Simple". In: *Physical Review Letters* 77.18 (1996), pp. 3865–3868 (cited on page 66).

[229] Minghang Jiang et al. "Review on strategies for improving the added value and expanding the scope of CO_2 electroreduction products". In: *Chemical Society Reviews* 53 (2024), pp. 5149–5189 (cited on page 69).

[230] Peiqi Guo et al. "Perspectives on Cu–Ag Bimetallic Catalysts for Electrochemical CO_2 Reduction Reaction: A Mini-Review". In: *Energy & Fuels* 38.7 (2024), pp. 5659–5675 (cited on page 69).

[231] Tatiana Morin Caamano et al. "Plasmon-enhanced CO_2 electroreduction on copper, silver, and copper–silver nano-catalysts". In: *Electrochimica Acta* 488 (2024), p. 144182 (cited on page 69).

[232] Linlin Chen et al. "Enhancing C_2 Selectivity in Electrocatalytic CO_2 Reduction Via Synergy of Plasmonic Hot Electrons and Photothermal Effect". In: *Angewandte Chemie International Edition* e202515432 (2025) (cited on page 69).

[233] Seung-Hoon Lee et al. "Formate-Induced Dissolution and Reprecipitation of a Copper Electrocatalyst during Electrochemical CO_2 Reduction Reaction". In: *The Journal of Physical Chemistry C* 129.40 (2025), pp. 18011–18024 (cited on page 75).

Acknowledgments

Producing and publishing scientific work is always accompanied by a lot of stress and doubt. However, no pain, no gain. I learnt a lot from this process, not only the scientific skills, but also the attitude towards setbacks.

First and foremost, I would like to express my deepest gratitude to **Prof. Emiliano Cortés**, who hosted me during my PhD and whose input from the grand project ideas to the minute detail of crafting beautiful figures greatly improved the success of my PhD projects. I deeply grateful for his calm and trusting manner. Moreover, thank him for toping up my salary based on my scholarship for two years. Also thank to **Dr. Andrei Stefancu**, who helped my CuPd projects a lot, spending time and energy to analyze the data and revise my paper.

Furthermore, Special thank to **Prof. Dr. Min Liu** in Central South University, who was my supervisor when I was a Master student. He encouraged me to study abroad, as well as strong support. His support for me did not end with my master's degree. He hosted me in his group for exchange, and gave me useful suggestions. I am very grateful for his encouragement and support. Hope he can achieve his goal.

Moreover, I would like to thank my PhD defense committee.

Thank **Yicui Kang** and **Chenghao Fan**, we knew each other four years ago, we talked about projects, we shared the daily life, and we went to Brazil together. I will never forget our helicopter ride over Rio and our cooking in an apartment at the foot of Monte Cristo. Thank **Yehua**, we spent less than one year with each other, but he gave me very big help about my projects. More than that, we almost talked every week days and we often ate lunch together in the kitchen of the institut. Thank **Tao Jiang**, who is very helpful and nice, often work late and close GC for me, providing help in my daily life.

Thank **Dmytriy Gryb**, we shared great time at lunch. We talked many topics and shared daily life with each other. With his help, my spoken English improved a lot. He is always patient and nice. Hope we can see each other in China in 2026 and we can keep contact in the future. Thank to **Dr. Christoph Gruber, Dr. Simone Ezendam, Dr. Oliver Henrotte**, **Franz Gröbmeyer**, they are always helpful and friendly. Thank **Eduardo Mariani** and **Victor Fernandez Gonzales**, we knew each other this year, but we get along well with each other. Thank to our technician and secretary **Reinhold Rath, Namvar Jahanmehr, Denise Wedemeyer,** and **Martina Edenhofer** to support us technically and administratively.

Thank **Diya Xie, Jiaqi Chen, Xueqing Miao, Dr. Haiyang Hu, Dr. Chenhao Li, Dr. Wenzheng Lu, Dr. Rui Lin, Chi Zhang, Dr. Hong Zheng, XiaoXia Chen**, we spent

many great time in the kitchen of institut and restaruants. The time with them is my spiritual wealth.

Thank **Dr. Kang Liu, Dr. Hang Zhang, Prof. Dr. Junwei Fu, Dr. Qiyou Wang, Dr. Jingwei Li Huang, Qin Chen, Ziwen Mei, Xiaojian Wang, Xi Zi** helped me with my projects.

Thank to my **parents** and my relatives, their supports are very important to me. Special thank to **Chao Yang**, we met at the beginning of Phd study on September, 2021 and we have been with each other almost four years. We have many good memories during these four years for cooking, eating dinner, travel, watching movies and playing games. Hope we will get better and better.

I am so luck to meet such nice people. Finally, I want to say to myself. I am sure this is a very nice and special journey for my whole life, I must miss these four years in the future, miss Munich, English Garden, Marienplatz, Nanoinstitut, the kitchen, my home at Lindwurmstrasse street, many places I have visited in Europe and Brazil. This is the best life for my previous 29-year life. Time always goes fast. Hope I will be more optimistic and brave in the future, whatever the future holds.